JNeurosci Accepted Manuscript

JNeurosci
THE JOURNAL OF NEUROSCIENCE

Research Report: Regular Manuscript

Network architecture of gap junctional coupling among parallel processing channels in the mammalian retina

https://doi.org/10.1523/JNEUROSCI.1810-19.2020

Cite as: J. Neurosci 2020; 10.1523/JNEUROSCI.1810-19.2020

Received: 28 July 2019
Revised: 27 March 2020
Accepted: 12 April 2020

This Early Release article has been peer-reviewed and accepted, but has not been through the composition and copyediting processes. The final version may differ slightly in style or formatting and will contain links to any extended data.

Alerts: Sign up at www.jneurosci.org/alerts to receive customized email alerts when the fully formatted version of this article is published.

Copyright © 2020 Sigulinsky et al.

JNeurosci Accepted Manuscript

TITLE

Network architecture of gap junctional coupling among parallel processing channels in the mammalian retina.

ABBREVIATED TITLE

Gap junctional coupling in the mammalian retina

AUTHORS

Crystal L. Sigulinsky[1]*, James R. Anderson[1], Ethan Kerzner[2], Christopher N. Rapp[1], Rebecca L. Pfeiffer[1], Taryn M. Rodman[1], Daniel P. Emrich[1], Kevin D. Rapp[1], Noah T. Nelson[1], J. Scott Lauritzen[1], Miriah Meyer[2], Robert E. Marc[1], Bryan W. Jones[1]*

AFFILIATIONS

[1]Department of Ophthalmology, John A. Moran Vision Institute, University of Utah School of Medicine, Salt Lake City, UT 84132.

[2]Scientific Computing and Imaging Institute, University of Utah School of Computing, Salt Lake City, UT 84132.

***CORRESPONDING AUTHORS (2)**

Crystal L. Sigulinsky, Ph.D.
John A. Moran Eye Center
65 Mario Capecchi Dr
University of Utah
Salt Lake City, UT 84132
801-585-6502 voice
crystal.sigulinsky@hsc.utah.edu

Bryan W. Jones
John A. Moran Eye Center
65 Mario Capecchi Dr
University of Utah
Salt Lake City, UT 84132
801-585-5954 voice
bryan.jones@m.cc.utah.edu

JNeurosci Accepted Manuscript

Number of Text Pages: 77

Number of Figures: 14

Number of Tables: 3

Number of Multimedia: 0

Number of Words for Abstract: 250

Number of Words for Introduction: 648

Number of Words for Discussion: 1499

CONFLICT OF INTEREST

REM is a principal of Signature Immunologics, Inc., manufacturer of some antibodies used in this manuscript.

ACKNOWLEDGEMENTS

This work was supported by the National Institutes of Health: R01 EY02576 (REM), R01 EY015128 (BWJ), R01 EY028927 (BWJ), P30 EY014800 (Core), and T32 EY024234 (CLS); the Calvin and JeNeal Hatch Presidential Endowed Chair (REM); and an Unrestricted Grant from Research to Prevent Blindness, New York, NY to the Department of Ophthalmology & Visual Sciences, University of Utah. Funding for the JEOL JEM-1400 was generously provided by the late Martha Ann Healy, a friend of the Moran Eye Center. We thank Hope Morrison, John Hoang, Alex Sessions, Nicholas McCarthy, Jeebika Dahal, Jessica Garcia, and Andrea Bordt for cell tracing.

JNeurosci Accepted Manuscript

ABSTRACT

Gap junctions are ubiquitous throughout the nervous system, mediating critical signal transmission and integration, as well as emergent network properties. In mammalian retina, gap junctions within the Aii amacrine cell-ON cone bipolar cell (CBC) network are essential for night vision, modulation of day vision, and contribute to visual impairment in retinal degenerations, yet neither the extended network topology nor its conservation is well established. Here, we map the network contribution of gap junctions using a high resolution connectomics dataset of an adult female rabbit retina. Gap junctions are prominent synaptic components of ON CBC classes, constituting 5-25% of all axonal synaptic contacts. Many of these mediate canonical transfer of rod signals from Aii cells to ON CBCs for night vision, and we find that the uneven distribution of Aii signals to ON CBCs is conserved in rabbit, including one class entirely lacking direct Aii coupling. However, the majority of gap junctions formed by ON CBCs unexpectedly occur between ON CBCs, rather than with Aii cells. Such coupling is extensive, creating an interconnected network with numerous lateral paths both within, and particularly across, these parallel processing streams. Coupling patterns are precise with ON CBCs accepting and rejecting unique combinations of partnerships according to robust rulesets. Coupling specificity extends to both size and spatial topologies, thereby rivaling the synaptic specificity of chemical synapses. These ON CBC coupling motifs dramatically extend the coupled Aii-ON CBC network, with implications for signal flow in both scotopic and photopic retinal networks during visual processing and disease.

SIGNIFICANCE STATEMENT

Electrical synapses mediated by gap junctions are fundamental components of neural networks. In retina, coupling within the Aii-ON CBC network shapes visual processing in both the scotopic and photopic networks. In retinal degenerations, these same gap junctions mediate oscillatory activity that contributes to visual impairment. Here, we use high resolution connectomics strategies to identify gap

JNeurosci Accepted Manuscript

junctions and cellular partnerships. We describe novel, pervasive motifs both within and across classes of ON CBCs that dramatically extend the Aii-ON CBC network. These motifs are highly specific with implications for both signal processing within the retina and therapeutic interventions for blinding conditions. These findings highlight the underappreciated contribution of coupling motifs in retinal circuitry and the necessity of their detection in connectomics studies.

INTRODUCTION

Gap junctions are intercellular channels electrically and metabolically coupling cells through direct exchange of ions and small molecules. Ubiquitous throughout invertebrate and vertebrate central nervous systems, gap junctions provide the anatomical substrate for electrical synapses. Like their chemical synapse counterparts, gap junctions exhibit developmentally regulated tissue- and cell-specific expression (Lin et al., 2005; Kihara et al., 2006), divergent conductance and selectivity (Veenstra et al., 1995), and extensive plasticity through gating modulation (O'Brien, 2019).

Historically believed to simply facilitate rapid bidirectional signal propagation, electrical synapses are increasingly acknowledged as key network components with diverse roles in the transmission and integration of signals (Nagy et al., 2018). Gap junctions are well-known for mediating synchronization of oscillatory activity among neuronal ensembles, the fundamental mechanism underlying emergence of the central pattern generator in the embryonic zebrafish spinal cord (Saint-Amant and Drapeau, 2001), and implicated in cognition, including attention, learning and memory (Hormuzdi et al., 2001; Buhl et al., 2003; Long et al., 2004; Frisch et al., 2005; Coulon and Landisman, 2017). Additional emergent network properties afforded by synchrony (Marder, 1998) include: coincidence detection (Das et al., 2017), enhanced signal saliency (DeVries et al., 2002), pathway sensitization (Yang et al., 1990; Rash et al., 2013), low-pass filtering triggering desynchronization (Vervaeke et al., 2010), and shunting of

JNeurosci Accepted Manuscript

presynaptic signals for regulatory feedback (Kawano et al., 2011). Despite repeated findings of critical roles for gap junctions in the formation and function of neural networks, the expressing cells, participating circuits, and function remain largely unknown, and oft ignored.

Gap junctions in mammalian retina are best known for their role in scotopic night vision as obligate components of the primary pathway. In dim light, signals produced by light-sensing rod photoreceptors are collected by rod bipolar cells and transferred through chemical synapses to Aii amacrine cells (AC). Aii cells distribute these scotopic signals into the ON/OFF pathways of photopic day vision established by the opposing functional responses of ON and OFF cone bipolar cell (CBC) superclasses to light. Using sign-inverting chemical synapses onto OFF CBCs and sign-conserving electrical synapses with ON CBCs, Aii cells thereby maintain opposing light responses (Kolb and Famiglietti, 1974; Marc et al., 2014). CBCs transmit these scotopic signals (or photopic signals from cone photoreceptors) to ganglion cells (GC) for projection to the brain. Absence of the connexin proteins supporting Aii-ON CBC gap junctions strongly impairs scotopic signaling (Guldenagel et al., 2001; Deans et al., 2002; Maxeiner et al., 2005). The 5-7 classes of mammalian ON CBCs are believed to serve parallel processing channels and appear to receive differential input from Aii cells (McGuire et al., 1984; Cohen and Sterling, 1990; Veruki and Hartveit, 2002a; Tsukamoto and Omi, 2017). Gap junctions or coupling have also been reported between CBCs (Kolb, 1979; Marc et al., 1988; Cohen and Sterling, 1990; Umino et al., 1994; Luo et al., 1999; Mills, 1999; Dacey et al., 2000; Jacoby and Marshak, 2000; Arai et al., 2010; Kantor et al., 2017; Tsukamoto and Omi, 2017). Unfortunately, partner identification largely remains unresolved and species-specific divergence is suggested. Understanding ON CBC coupling motifs is critical as they contribute to shaping visual processing in both the scotopic and photopic networks (Guldenagel et al., 2001; Deans et al., 2002; Maxeiner et al., 2005; Demb and Singer, 2012; Farrow et al., 2013; Kuo et al., 2016; Seilheimer et al.,

JNeurosci Accepted Manuscript

124 2020). Moreover, these gap junctions subserve aberrant hyperactivity contributing to visual impairment
125 in retinal degenerative disease (Trenholm et al., 2012; Ivanova et al., 2016).
126
127 Here, we used serial section transmission electron microscopy (ssTEM)-based ultrastructural
128 connectomics to map the ground truth for gap junction contribution to retinal circuits. We report class-
129 specific coupling patterns for all seven rabbit ON CBC classes that are richer and more extensive than
130 previously appreciated. These motifs reveal extensive coupling both within and across parallel
131 processing streams of the rabbit retina, with implications for photopic and scotopic visual networks and
132 their disruption in disease.
133
134 **METHODS**
135 **Connectomics volume RC1**
136 ***Volume construction***
137 Retinal Connectome 1 (RC1) is an ultrastructural dataset acquired at 2.18 nm/pixel resolution from the
138 retina of a light-adapted 13-month-old female Dutch Belted rabbit (Oregon Rabbitry, OR). Dataset is
139 freely available at connectomes.utah.edu. RC1 spans the inner nuclear layer (INL) through ganglion cell
140 layer (GCL) of a 0.25 mm diameter field of mid-peripheral retina. Methods concerning tissue acquisition
141 and processing, volume assembly, visualization and annotation have been extensively detailed
142 (Anderson et al., 2009; Anderson et al., 2011b; Anderson et al., 2011a; Lauritzen et al., 2013; Marc et al.,
143 2013; Marc et al., 2014; Lauritzen et al., 2019). In short, the RC1 dataset was constructed from 371 serial
144 transmission electron microscopy (TEM) sections (70-90 nm thick), captured via Automated
145 Transmission Electron Microscopy (ATEM) at 5000X, combined with 11 optical sections intercalated
146 through the IPL, 6 capstone optical sections in the INL and another 12 capstone optical sections in the
147 GCL. These optical sections were probed for small molecule signals for computational molecular

JNeurosci Accepted Manuscript

148 phenotyping (CMP) (Marc et al., 1995). Sections were aligned into a single volume using the NCR
149 ToolSet, which has since been replaced by Nornir (RRID: SCR_016458). All protocols were in accord with
150 Institutional Animal Care and Use protocols of the University of Utah, the ARVO Statement for the Use
151 of Animals in Ophthalmic and Visual Research, and the Policies on the Use of Animals and Humans in
152 Neuroscience Research of the Society for Neuroscience.

153

154 ***Dataset viewing and annotation***

155 Dataset visualization and annotation was performed using the Viking Viewer for Connectomics
156 (RRID:SCR_005986; referred to hereafter as "Viking"), available via free license for educational use
157 through the University of Utah. Viking allows concurrent volume annotation by multiple users across
158 html-compliant protocols. Our manual annotation process involves users converting the raw 3-
159 dimensional (3D) image data into a set of 2D shape geometries stored in a central Microsoft SQL Server
160 Spatial Database. Each cell is tracked through the cross-sectional images of the 3D volume while
161 recording the boundaries of the cell membrane and cellular features (e.g. ribbon presynapse,
162 postsynaptic density, etc.) into the database. An "annotation" is single disconnected 2D outline of a cell
163 or cellular feature on a single section image and any user-defined data. Each cellular feature, or
164 "structure" is described by a set of annotations inter-connected across sections that collectively describe
165 its 3D morphology. For legacy reasons, RC1 cell boundaries were encoded using a 2D disc sized to the
166 largest diameter that can be completely contained within the continuous shape of the cell's membrane
167 on a given section. Membrane-associated structures, such as gap junctions and postsynaptic densities,
168 were encoded as poly-lines in the database and visualized as curves in the Viking user interface. Viking
169 organizes structures hierarchically and relationally. All cellular features are internal features of a cell and
170 organized in a parent-child hierarchy. Relational connections are encoded as links between structures.

JNeurosci Accepted Manuscript

For example, a ribbon presynapse in a bipolar cell would be a “child” of that bipolar cell “parent”. In turn, the ribbon pre-synapse could be linked to a post-synaptic density of the opposed cell to record the relationship between the structures. Importantly, a gap junction instance requires two gap junction annotations, each a child of their respective parent cells, with a bidirectional link. As some candidate gap junctions present with oblique orientations, confidence values were assigned to each annotation to reflect their confirmed versus candidate status and results of reimaging. Reimaging to obtain optimized section tilt for structure validation was performed at 40,000X magnification (0.27 nm/pixel resolution) with goniometric tilt.

Dataset analysis

All cells and structures are automatically assigned unique identifiers in the Microsoft SQL Server Spatial Database during annotation and numerically indexed to their location, shapes, and connectivity within RC1. This enables direct queries of the SQL database (SQL queries) to extract descriptions of cellular composition and network interactions, as well as evaluation in a host of custom, open-source software tools for visualization or analysis (for references, links and RRIDs, see the “Software Accessibility” section. Cell morphology was visualized on a per cell basis in ball and stick plots through morphology export functions in Viking to the network graph visualization application Tulip. The morphology of individual cells and spatial organization of large groups of cells was visualized in the 3D rendering environments VikingPlot and VikingView or through import into Blender. Morphometric features were retrieved or computed using Microsoft SQL queries. Use of a spatial database allows easy access to the established computational geometry analysis methods referred to throughout the paper. Synaptology and connectivity were explored or analyzed using Microsoft SQL queries, Cell Sketches, Graffinity,

JNeurosci Accepted Manuscript

and/or through network export for Tulip using the custom Python-based TulipPaths plug-in developed to query the connectivity graphs.

Cell identification

The small molecule signals from immunolabeled capstone and intercalated sections through the cell somas in the INL of the RC1 dataset for glutamate, glycine, and 4-aminobutyrate (GABA), enabled classification of every soma in the INL as belonging to an OFF CBC, ON CBC, rod bipolar cell, narrow-field glycinergic amacrine cell (GAC), wide-field GABAergic amacrine cell, or Müller cells (Anderson et al., 2009; Anderson et al., 2011b). The characteristic signature of high glutamate, medium glycine, and no GABA initially identified the subset of ON CBC candidates. ON CBC identity was confirmed by the presence of ribbon- and absence of conventional-type presynapses. Classification of these cells proceeded as described in the Results based upon axonal arbor features, including field area and the depth and breadth of stratification within the IPL, tiling, and synaptology. This process was performed iteratively until every candidate ON CBC with arbors fully contained within the volume was classified.

Synaptology and coupling profiles

Tabulations of synapses and other child structures, as well as details regarding the partner cell and child structure, were obtained from Microsoft SQL queries or Cell Sketches. Cell Sketches software was developed to support the visual analysis of neuron statistics and spatial properties. It pulls data from RC1's public interface (http://websvc1.connectomes.utah.edu/RC1/OData/) and is implemented in JavaScript using AngularJS (http://www.angularjs.org) and D3.js (http://www.d3js.org). Cell Sketches counts synapse statistics through iterative database queries.

JNeurosci Accepted Manuscript

215

216 **Cell morphometrics and distribution**

217 ***Aii and ON CBC stratification***

218 To control for the inherent volume curvature and local variability in the position of the inner plexiform
219 layer (IPL), the section corresponding to the top and bottom of the IPL was determined based on the
220 emergence or disappearance of neuronal processes at the XY somal position for 22 RC1 Aii cells directly
221 from volume visualization in Viking. For Aii cells impacted by the block refacing event in strata 4/5 of the
222 IPL, the bottom of the IPL was estimated using the average IPL thickness calculated from non-impacted
223 Aii cells (*n* = 8/22 Aii cells, 225 ± 4 sections). Using vertical views of 3D reconstructions in VikingView of
224 Aii cell morphology and synaptology, the ON/OFF boundary position was assessed at the XY somal
225 position as the bottom of the lobular dendrites and top of gap junction compartmentalization (Marc et
226 al., 2014). The consistency of the calculated ON/OFF boundary position within the IPL suggests that our
227 normalization method accounted well for volume curvature and local variation is limited (*n* = 22 Aii cells;
228 45% ± 3% IPL). Stratification of ON CBC arbors was evaluated from histograms of annotation frequency
229 by RC1 section, using a 5-section bin size. To control for volume curvature, the top and bottom of a cell's
230 axonal arbor was determined as the start or end section, respectively, of the bin situated at the
231 inflection points of the histogram curve. As the block refacing event also impacted determination of the
232 bottom of the IPL for ON CBC axonal stratification measures, the position of these sections within the
233 IPL was calculated as the average section difference from the top or bottom of the IPL determined for
234 the nearest Aii cell(s).

235

236 ***Branch path complexity***

JNeurosci Accepted Manuscript

Using the 3D reconstructions rendered in VikingView or VikingPlot, binary trees were manually drawn to capture the branching topology, ignoring branch lengths. Tree elements (Uylings and van Pelt, 2002) were marked and the number of branch terminals derived. Branch path complexity was determined using the parameterization and calculation reported by Elliott and colleagues (2015).

Mosaic analysis

Class mosaics were evaluated for regularity using the conformity ratio (mean / standard deviation (SD) of the nearest neighbor distances), as this measure is least impacted by boundary effects (Cook, 1996). Nearest neighbor distances were obtained using a Microsoft SQL query that calculates the distance between the geometric centroids of annotations on a given section in the RC1 database. Due to slight differences in somal depths across the volume, sections were chosen to optimize soma position and remove annotation ambiguity (Section 0001 - CBb5, CBb6; Section 0020 – CBb4, CBb4w; Section 0030 – CBb3, CBb3n).

Intersection analysis

The area of spatial overlap between cell arbors was calculated using a Microsoft SQL query (Anderson et al., 2019). First, the 2D convex hulls of all cells in two specified classes were determined. The intersection of the convex hulls for all pairwise combinations between the two classes was identified and the overlap fraction determined. The area of spatial overlap was then computed by multiplying the fraction by the area of the cell's convex hull. Using the R software environment, the data was fitted to a linear model with a y-intercept of zero and adjusted R^2 values obtained. An ANCOVA was then run using package "car" and the *post-hoc* Scheffe test run using package "agricolae".

JNeurosci Accepted Manuscript

Size distribution of gap junctions

The areas of the individual gap junction plaques formed by the 37 ON CBCs examined in this study were estimated by summing the products of the annotation lengths on each section multiplied by section thickness. Polyline annotations for gap junctions were centered on the inner leaflet of the parent cell's plasma membrane and extended the length of the zippered gap junction. In oblique and *en face* views, annotations were centered in the middle of the density and extended the length of the darkest continuous portion. Area values were obtained through a Microsoft SQL query of the spatial database, which assumed a 90 nm section thickness. Freeze-fracture studies have revealed that gap junctions of the rodent IPL exist in a variety of configurations (Kamasawa et al., 2006). Our analyses are restricted to the ON sublamina, where string and ribbon configurations are virtually absent. Thus, the gap junctions described in this report likely exist in plaque (conventional crystalline or non-crystalline) or reticular (containing small voids) configurations, supporting our methodology for size estimation. Plasticity evoked by light adaptation and neurotransmission primarily alters the open conductance of existing channels by controlling their phosphorylation state, rather than promoting changes in the abundance or type of channels. Furthermore, while light-dependent changes in gap junctional area (arising from changes in connexon density) have been reported for gap junctions coupling horizontal cells in teleosts (Kurz-Isler and Wolburg, 1986, 1988; Baldridge et al., 1989; Kohler et al., 1990; Washioka et al., 1991; Kurz-Isler et al., 1992), no such changes in connexon density nor changes in the number or distribution of gap junction configurations were reported in the IPL of rat or mice under different light adaptation conditions and points in the circadian cycle (Kamasawa et al., 2006). As each gap junction is represented by two linked gap junction annotations, one belonging to each of the coupled parent cells, size estimates for only one annotation was used to prevent overrepresentation of homocellular gap junctions during analyses, as appropriate. The size distributions for gap junctions mediating various

JNeurosci Accepted Manuscript

283 coupling modes both in sum and within classes were compared using pairwise Wilcoxon rank-sum tests
284 with continuity correction using the R software environment. All reported *p* values were adjusted for
285 multiple comparisons using the Benjamini-Hochberg procedure (α = 0.5).

286

287 **Spatial distribution of gap junctions**

288 Positions of the 1339 gap junctions formed by the 37 ON CBCs detailed in this study were assessed in
289 the horizontal plane as a function of distance from the geometric center of the parent cell's convex hull
290 using the spatial properties derived by Cell Sketches. Using the 2D (XY) position of location annotations
291 in the RC1 database, Cell Sketches computes the convex hull of structures using an implementation of
292 Andrew's Monotone Chain Algorithm (Bostock et al., 2011). Geometric centroids of these convex hulls
293 are then used to compute the 2D distance between a child structure and the parent cell's axonal
294 territory. As bipolar cell axonal arbors are best described as star domains, in order to evaluate the
295 distribution of gap junctions relative to arbor boundaries, the vertices of the convex hull for each cell
296 were located, annotated as child structures, and distances computed as for gap junctions. As each gap
297 junction is represented by two linked gap junction annotations, one belonging to each of the coupled
298 parent cells, distance measures for only one annotation were used to prevent overrepresentation of
299 homocellular gap junctions in the analyses, as appropriate. The spatial distributions for gap junctions
300 mediating various coupling modes and convex hull vertices were compared using pairwise Wilcoxon
301 rank-sum tests with continuity correction using the R software environment. All reported *p* values were
302 adjusted for multiple comparisons using the Benjamini-Hochberg procedure (α = 0.5).

303

304 **Glycine signatures**

JNeurosci Accepted Manuscript

The use of quantitative small molecule signatures, including glycine to define ON CBC cells coupled to GACs and Aii cells has been described previously (Marc, 1999; Anderson et al., 2011b; Marc et al., 2014). Every ON CBC in RC1 has its soma or axon aligned with sections 1, 30 and/or 152 containing quantitative grey-scale imagery of glycine immunoreactivity (Anderson et al., 2011b), spanning intracellular concentrations ranging from ≈ 0.4 - 10 mM (Jones et al., 2003; Marc and Jones, 2003). All retinal cells contain measurable levels of glycine. Most cells (e.g. rod bipolar cells, OFF CBCs, Müller cells) maintain very low levels at 0.1 mM or less, while true GACs reach 0.6-10 mM (Kalloniatis et al., 1996; Marc et al., 2014). ON CBCs lie in between, with pixel values corresponding to 0.2-0.5 mM. Such glycine signals have been interpreted as arising from gap junctional coupling (Marc and Liu, 1984; Cohen and Sterling, 1986; Pourcho and Goebel, 1987; Vaney et al., 1998; Pow and Hendrickson, 2000; Petrides and Trexler, 2008; Marc et al., 2014). Histograms of quantitative glycine signal were obtained for each bipolar cell in RC1 and the mean pixel value calculated using ImageJ (RRID:SCR_003070). Glycine values reported here are higher than those reported previously (Anderson et al., 2011b) due to sampling using a larger region of interest that better matches full cell histograms, but changes no cell assignments. Glycine signal in ON versus OFF CBCs was compared using conventional parametric statistics (Welch two sample t-test, 2 tailed, heteroscedastic) using the R software environment.

Image preparation

Viking (Anderson et al., 2009; Anderson et al., 2011a; Lauritzen et al., 2013; Marc et al., 2014; Lauritzen et al., 2019) was used for all TEM image viewing, small molecule overlays and image annotation. Small molecule optical overlays combined TEM grayscale data with hue and saturation of the small molecule optical signal as described previously (Anderson et al., 2011b). Pseudocoloring of cells in TEM images for figures was accomplished in Adobe Photoshop CC 2018 (Adobe, San Jose, CA, USA; RRID: SCR_014199)

JNeurosci Accepted Manuscript

by creating separate color layers in either color or overlay blend mode with an opacity of 40-70% that were then merged with the original TEM image. High resolution TEM recaptures (40,000 x mag, 0.27 nm/pixel resolution) and "zoomed" native views of structures directly from Viking were min-max contrast stretched and gamma remapped to 1.3 in Adobe Photoshop CC 2018 to improve visualization, unless noted otherwise. Density plots were acquired with Fiji (ImageJ 1.52p; RRID: SCR_002285) for the region of interest denoted in the figures. Graphs were generated in Microsoft Excel 2016. 3D cell reconstructions were rendered in MATLAB (RRID:SCR_001622) from Viking annotations (Anderson et al., 2011b; Anderson et al., 2011a) and displayed using VikingPlot. Cell features (synapses, adherens junctions, etc.) are shown unscaled, unless noted otherwise, and rendered in 3D visualizations as volumetric shapes from circles with a diameter equal to that of the summed polyline lengths on each section. Cells in figures 1A and 7A illustrating stratification were chosen for their close proximity and rendered together but with only one cell visible at a time to maintain spatial relationships. Renderings were layered and cells moved laterally to facilitate visibility and ordering. Inherent volume curvature was corrected for using two CBb3 cells on either side for the Y axis and the CBbwf arbor along the X axis based on reference to Aii cells. IPL and ON/OFF boundaries were defined using neighboring Aii cell morphology and connectivity compartmentalization. Connectivity graphs were generated using Graffinity. All graphs and images were imported into Adobe Illustrator CC 2018 (Adobe, San Jose, CA, USA; RRID: SCR_010279) for final figure organization.

Experimental Design and Statistical Analysis

All results were derived from the RC1 dataset, a single volume of retinal tissue containing at least 16 cells for every ON CBC class (except CBbwf). At least 5 fully reconstructed and mapped cells from each class were used to compile synaptology and coupling profiles. Data from 2 incomplete cells were

JNeurosci Accepted Manuscript

reported, where possible, for the wide field ON cone bipolar (CBbwf) class. Analyses used the 1339 gap junctions formed by the 37 ON CBCs or 455 gap junctions formed by the four Aii cells detailed in this paper. The numbers of cells, synapses or gap junctions for each statistic are provided in the Results sections. All values are reported as the mean ± standard deviation (SD), unless otherwise noted. Statistical analyses of network features are detailed in the Methods sections describing the analyses. Statistical analyses were performed in Microsoft Excel 2016 (RRID:SCR_016137) or R version 3.6.1 (RRID:SCR_001905), as indicated. The R software environment reports p values < $2.2E^{-16}$ as zero. We report these as *** in figures and $p < 2.2E^{-16}$ in the text. The following sections detail the analyses performed in this publication.

Software Accessibility

The custom, open-source software tools are freely available: Viking (RRID:SCR_005986) (Anderson et al., 2009), VikingPlot (DOI: 10.5281/zenodo.3234870, https://zenodo.org/record/3234870#.XO7Y7IhKguU) (Anderson et al., 2011b; Anderson et al., 2011a), VikingView (DOI: 10.5281/zenodo.3267451, https://zenodo.org/record/3267451#.XSUW1OhKguU; available for download here: https://connectomes.utah.edu/export/vikingview.html), Tulip (http://tulip.labri.fr/TulipDrupal/), TulipPaths (DOI: 10.5281/zenodo.1346342, https://zenodo.org/record/1346342) (Lauritzen et al., 2019), Blender (http://www.blender.org/), Cell Sketches (DOI: 10.5281/zenodo.1346344, https://zenodo.org/record/1346344), and Graffinity (DOI: 10.5281/zenodo.1422851, https://zenodo.org/record/1422851) (Kerzner et al., 2017). Export of Viking data for these and other programs (e.g. Microsoft Excel) is available here: http://connectomes.utah.edu/export/toctree.html.

JNeurosci Accepted Manuscript

374 **Code Accessibility**

375 All Microsoft SQL queries utilized in this paper are freely available:
376 (https://github.com/connectomes/Archive/tree/2018_OnBipolarCoupling) (Anderson et al., 2019).
377 Specific cell numbers, labels, and synapse types contained within these queries can be changed
378 according to the provided database schema. For specific cell and structure identification numbers, refer
379 to the figure legends.

380

381 **RESULTS**

382 During reconstruction of the ON CBCs in RC1 in our previous work (Marc et al., 2014; Lauritzen et al.,
383 2019), we discovered that gap junctions between ON CBCs were more common than those formed with
384 Aii cells. As this contradicts the general belief that Aii cells are in fact the dominate coupling partner of
385 ON CBCs and has implications on visual processing in the retina, we sought to investigate these specific
386 motifs in more detail. Doing so first required a comprehensive classification of the ON CBCs in RC1. This
387 classification required additional parameters beyond conventional morphological measures, namely
388 connectivity, in which several coupling motifs proved valuable in achieving complete classification.
389 Therefore, we first describe and evaluate the classification of ON CBCs in rabbit retina into seven classes.
390 We then detail their coupling profiles, including the prevalence and distribution of gap junctions and the
391 specificity of coupling partnerships, size and spatial topologies. Lastly, we explore the implications of
392 these coupling motifs on retinal networks, particularly on the distribution of scotopic signals by Aii cells,
393 and the potential mixing of parallel processing streams for input to ganglion cells.

394

395 **Classification of ON CBCs**

396 Here, we use terminology based on computational classification theory where a *class* is a collection of
397 members sharing certain attributes and separable from other classes. If further separation is not

JNeurosci Accepted Manuscript

398 possible, these may reflect natural classes (Marc and Jones, 2002; Marc et al., 2018). Accordingly, we
399 have distinguished seven classes of ON CBCs in rabbit retina: CBb3, CBb3n, CBb4, CBb4w, CBb5, CBb6,
400 and CBbwf (Figure 1A). We previously adopted a nomenclature (Marc et al., 2018; Lauritzen et al., 2019)
401 that merged our early classifications (Lauritzen et al., 2013; Marc et al., 2014) with those of MacNeil and
402 colleagues (2004) and McGillem and Dacheux (2001), and retain it here, for purposes of consistency.
403 One exception is the renaming of the CBb7 class from our previous publication (Marc et al., 2014) to
404 CBb6. We stress, however, that our numbers *do not* reflect positioning within the historical, five equal
405 strata divisions of the retinal IPL as was common in many early classification schemes.
406
407 Manual classification in RC1 began with a small set of ~40 fully reconstructed and centrally located
408 bipolar cells. Historically, classification of ON CBCs relied heavily on axon arbor area and the
409 stratification depth and breadth of the axonal arbors within the IPL (Famiglietti, 1981; McGuire et al.,
410 1984; Cohen and Sterling, 1990; Strettoi et al., 1994; Jeon and Masland, 1995; Massey and Mills, 1996;
411 Brown and Masland, 1999; McGillem and Dacheux, 2001; Casini et al., 2002; MacNeil et al., 2004;
412 Pignatelli and Strettoi, 2004; MacNeil and Gaul, 2008; Wassle et al., 2009; Helmstaedter et al., 2013;
413 Greene et al., 2016; Shekhar et al., 2016). In RC1 (mid-peripheral rabbit retina), only 3 ON CBC classes
414 could be readily distinguished using these variables (Figure 1A; Table 1). CBbwf was easily identified due
415 to its notably large arbor size. Its axonal arbor begins to spread laterally at the top of stratum 4 with
416 processes terminating deep within stratum 5. The CBb5 and CBb6 classes could be distinguished by their
417 smaller arbors and distinct, albeit overlapping, depth of axonal stratification. CBb5 cells stratify largely
418 within stratum 4, while CBb6 cells span strata 4 and 5. The remaining four classes (CBb3/3n/4/4w) fully
419 costratify within the proximal IPL, occupying the lower three quarters of stratum 3 and extending into
420 the top half of stratum 4. Detailed analysis of Aii cell morphology and connectivity compartmentalization

JNeurosci Accepted Manuscript

421 are consistent with the slightly deeper ON/OFF boundary implied by the top of these arborizations (Aii
422 cell ON/OFF boundary = 46% ± 3%, *n* = 8 Aii cells).
423
424 Much like the four costratifying classes of mouse Type 5 ON CBCs (Helmstaedter et al., 2013; Greene et
425 al., 2016; Shekhar et al., 2016; Tsukamoto and Omi, 2017), the costratified rabbit CBb3/3n/4/4w classes
426 lack obvious discriminating morphological features. Therefore, additional variables were needed for
427 further classification. Recent CBC classification schemes in mouse found the frequency or distribution of
428 synaptic ribbons provided discriminatory power (Tsukamoto and Omi, 2014, 2017), but we found no
429 obvious trends. Target-specific connectivity has also aided CBC classification, including GC target
430 specificity and coupling with Aii cells (Cohen and Sterling, 1990; Helmstaedter et al., 2013; Greene et al.,
431 2016). In RC1, GC dendritic processes are sufficiently spaced such that some ON CBCs may not have an
432 opportunity for connectivity, despite class specificity. Aii cells are narrow field and their arbors highly
433 overlapping, providing ample contact opportunity. Thus, much like the separability achieved for the b_3
434 and b_4 classes using Aii connectivity in cat retina (Cohen and Sterling, 1990), connectivity with Aii cells
435 divided the shallowly stratifying ON CBCs of RC1 into two groups based on a virtually binary
436 presence/absence of gap junctions with Aii cells. Cells within the resulting groups still exhibited
437 significant arbor overlap (lack of tiling), suggesting that at least two classes remained intermingled in
438 both the Aii-coupled and -noncoupled groups. The Aii-coupled grouped showed some differences in
439 arbor size among the cells, but cells of the Aii-noncoupled group were very similar. Examining
440 synaptology and non-Aii coupling partners revealed that cells of both groups formed frequent gap
441 junctions with some cells of the other group, but rare or no coupling with other cells of the group,
442 despite opportunity afforded by costratified and overlapping arbors. Using these coupling patterns,
443 together with 3D plots to assess tiling and compare arbor sizes, the cells within each resultant group
444 were finally resolved: the Aii-coupled group resolved into the narrow field CBb3n and wide field CBb4w

JNeurosci Accepted Manuscript

445 classes while the Aii-noncoupled group resolved into the CBb3 and CBb4 classes. The discriminating
446 coupling patterns were therefore the high frequency of coupling of CBb3 cells with CBb3n cells and of
447 CBb4 cells with CBb4w cells, and the virtual lack of coupling of CBb3 cells with CBb4w and of CBb4 cells
448 with CBb3n (detailed in following sections).
449
450 The virtually binary nature of discriminating coupling relationships (with Aii, CBb4w and CBb3n), enabled
451 us to rapidly extend classification across the entire RC1 volume after an initial segregation based on
452 stratification. Notably, this scheme often allowed classification of even partial cells. Thus, of the 178
453 whole or partial ON CBCs identified in RC1, 156 (88%) were classified as one of the seven classes, 40 of
454 which had at least some portion of their arbors extending beyond volume boundaries. Of the remaining
455 22 unclassified cells, 14 somas had descending axons that extended outside of the volume boundaries
456 and another 8 had significant portions of their arbors lost due to a block refacing event in strata 4/5 of
457 the IPL that affected tracing of some ON CBCs in the northeast corner of the volume.
458
459 Notably, every cell with complete arbor reconstruction was readily classified as one of the seven classes
460 and no intermediate forms were identified (Cohen and Sterling, 1990). The conformity ratios (Table 1) of
461 the resulting class mosaics are consistent with those reported for identified neuronal mosaics in the
462 mammalian retina (Wassle and Riemann, 1978; Cook, 1996; Reese, 2008; Marc, 2009). Tiling of
463 neighboring arbors without (or with only minimal) overlap is a fundamental rule that holds for many
464 neuronal classes and has been shown for all known CBC classes where evaluated (Wassle et al., 2009;
465 Helmstaedter et al., 2013; Euler et al., 2014; Tsukamoto and Omi, 2014; Greene et al., 2016; Tsukamoto
466 and Omi, 2016; Kantor et al., 2017; Tsukamoto and Omi, 2017). With the possible exception of the
467 CBbwf class, which exhibited some arbor overlap, our classification resulted in sheets of cells that tiled
468 the volume (Figure 1B), further supporting each as a pure class.

JNeurosci Accepted Manuscript

Is this class list complete? Such a “parts list” is essential in the study of networks. Our classifications reveal that RC1 contains >15 cells of all but one ON CBC class, and importantly, at least two of the rarest class (CBbwf). Targeted searches using spatial queries and brute force surveys for unannotated or unclassified bipolar processes within the ON sublamina failed to identify additional candidates. Therefore, any additional classes must 1) be extremely sparse, 2) lack coupling with Aii cells, 3) lack coupling with all other ON CBC classes, and/or 4) stratify outside the ON sublamina of the IPL. There is no evidence suggesting a sparser class than CBbwf. Of the synaptic ribbon-forming cells fitting criteria 2-4, all exhibit Aii connectivity characteristic of either OFF CBCs or rod bipolar cells.

Ultrastructural identification of intercellular contacts

ON CBC axon terminals participate in a number of synapse types within the retinal IPL. In addition to electrical synapses mediated by gap junctions, these terminals provide excitatory glutamatergic drive via ribbon- and bipolar conventional-type synapses to GC and AC processes, and receive inhibitory conventional-type input from ACs. The connectomics strategy employed in the construction and annotation of RC1 provides unparalleled visualization and quantification of connectivity. Figures 2A,A’ and 2B,B’ are 3D reconstructions of the soma and axonal arbor of an ON CBC from RC1 illustrating the relative size and distribution of all identified synaptic contacts. At 2.18 nm/pixel (native RC1 resolution), all types of synaptic and structural contacts are directly discernable (Figure 2C-G). Importantly, even intercellular synaptic and structural contacts at non-optimal orientations are discernable from nonsynaptic membrane-to-membrane appositions, enabling us to take advantage of the unique capabilities of serial section TEM to perform high magnification reimaging with goniometric tilt. This is particularly relevant for the validation of gap junctions as they are indistinguishable from adherens junctions at oblique angles. At native resolution, a gap junction in RC1 oriented perpendicularly to the

JNeurosci Accepted Manuscript

493 section plane appears as a single, thin, electron dense band between two cells (Figure 2F,F') (Anderson
494 et al., 2011b; Marc et al., 2014; Marc et al., 2018). The membranes of the two cells appear to "pinch"
495 together at this location, obliterating any visible extracellular space between the two cells. This
496 presentation has been confirmed through extensive reimaging at high resolution and goniometric tilt (*n*
497 = 40; 40,000 X magnification = 0.27 nm/pixel resolution) to observe the pentalaminar profile (alternating
498 dark-light-dark-light-dark bands; Figure 2H,H') characteristic of gap junctions under these staining
499 conditions (Peters, 1962; Nagy et al., 2018). An electrical synapse density is often observed within the
500 cytoplasm beneath the membrane at sites of gap junctions and can be symmetric or asymmetric, usually
501 correlating with symmetry/asymmetry of participating cell classes and believed to arise as a
502 consequence of differences in molecular composition of the connexons formed by each cell class
503 (Strettoi et al., 1992; Anderson et al., 2011b; Pereda et al., 2013; Marc et al., 2014; Pereda, 2014; Marsh
504 et al., 2017; Miller et al., 2017; Tsukamoto and Omi, 2017; Nagy and Lynn, 2018). In contrast, adherens
505 junctions present as feathery membrane densities of variable thickness and symmetry, but with a
506 distinct extracellular space between the two cells that is wider, more uniform, and more electron dense
507 than surrounding nonjunctional extracellular space (Figure 2G, 2H"). Often, gap junctions are flanked by
508 adherens junctions (Figure 2H) (Nagy and Lynn, 2018). For the purposes of this paper, all densities with
509 oblique native orientations between CBCs and Aii cells or other CBCs were annotated as gap junction
510 candidates until reimaging proved otherwise. Of the 1339 gap junction instances described in this
511 report, 484 are confirmed, 429 (32%) without the need for reimaging. Between this and our previous
512 studies, 41 of 160 candidate RC1 gap junctions have been refuted (12 remain inconclusive due to
513 insufficient tilt capacity).
514
515 **Prominence of gap junctions in ON CBC circuitry within the IPL**

JNeurosci Accepted Manuscript

To assess the contribution of gap junctions to ON CBC axonal circuitry, we focused on a total of 37 cells, five to seven per class, reconstructed to statistical completion. The CBbwf class remains an exception, as we have only identified two class members within RC1 due to their low frequency, and neither are completely contained within the volume due to their large size. We find that all rabbit ON CBCs form gap junctions, at least 20 per cell, with some cells forming upwards of 80 (Table 2). Thus, electrical synapses can constitute upwards of 25% of an ON CBC's total synaptic contacts within the IPL, similar to that observed for Aii cells (total gap junctions = 114 ± 11, 0.09 CV; % total synaptic contact = 24.2% ± 2.8%, 0.11 CV; *n* = 4 cells). For four of the seven ON CBC classes, electrical synapses constitute at least 10% of their total synaptic contacts. Assuming these coupling sites are indeed functionally bidirectional (Xin and Bloomfield, 1999; Trexler et al., 2001; Veruki and Hartveit, 2002a, b) (c.f. Vaney, 1997), electrical synapses may constitute upwards of 50% of a given cell's total potential synaptic input or 40% of its total potential synaptic output. Similarly, electrical synapses constitute nearly two-thirds of an Aii cell's total potential synaptic output (64.0% ± 4.4%, 0.07 CV, *n* = 4), but only a quarter of its total potential input (28.0% ± 2.9%, 0.10 CV, *n* = 4). In terms of a cell's potential electrical conductivity, gap junctions account for 4-25% of the total channel-occupied membrane area in ON CBCs and 40-42% in Aii cells. While class-specific differences exist in both the frequency of gap junctions and their overall contribution to a cell's synaptic contacts, it is clear that electrical synapses are a prevalent form of synaptic communication and can represent a significant component of ON CBC circuitry within the IPL.

Coupling partnerships of ON CBCs

Before examining the specific coupling partnerships of ON CBC classes, we first wish to clarify terminology regarding *modes* of coupling. Here, we define heterocellular coupling as that between cells of different superclasses. In the retina, these are the categories of photoreceptors, horizontal cells, bipolar cells, amacrine cells, and ganglion cells. Homocellular coupling occurs between cells of the same

JNeurosci Accepted Manuscript

superclass. Historically, heterologous/homologous has been used in place of heterocellular/homocellular, but these terms evoke evolutionary considerations. This is also distinct from the uses of heteromeric/homomeric to describe the connexin protein composition of individual hexameric connexons and of heterotypic/homotypic to describe the composition of the two connexons comprising a gap junction channel. Homocellular coupling requires further distinctions. *Cross-class* homocellular coupling refers to coupling between two cells of same superclass, but different class (e.g. a CBb3n cell coupling with CBb3 cell). *In-class* involves coupling between pairs of cells from the same class (e.g. CBb3n cell coupling with a neighbor CBb3n cell). Lastly, *self* gap junctions, formed between processes originating from the same neuron, often called "sister" branches, are a specific type of in-class coupling (e.g. gap junction between two branches of CBb5 593). For ON CBCs in RC1, the sister branch often originates locally or is an extension of an adjacent varicosity. Such self gap junctions are worth differentiating as these may have limited contribution to the lateral spread of signals between cells and many neurons have been shown to distinguish processes arising from sister branches versus another cell of the same class and to initiate divergent growth behaviors accordingly, which underlie tiling and self-avoidance (Cameron and Rao, 2010; Grueber and Sagasti, 2010; Jan and Jan, 2010; Lefebvre, 2017; Mountoufaris et al., 2018).

Evaluation of ON CBC coupling partnerships in RC1 revealed two critical points. *First, noncanonical partnerships dominate ON CBC coupling in the IPL*. Of the 1339 gap junctions involving at least one of the 37 ON CBCs previously described, only 30% are the canonical heterocellular gap junctions with Aii cells responsible for transmission of scotopic signals through the mammalian rod pathway (Kolb and Famiglietti, 1974; McGuire et al., 1984; Strettoi et al., 1992; Anderson et al., 2011b; Marc et al., 2014). The other 70% mediate homocellular coupling between ON CBCs (62%) and heterocellular coupling with other noncanonical AC partners (8%). At the individual class level, homocellular coupling dominates for

JNeurosci Accepted Manuscript

four of the seven ON CBC classes, with a fifth class exhibiting a roughly equal distribution (Figure 3A). Detailed examination reveals that cells of each ON CBC class form coupling partnerships according to specific rulesets: a unique combination of partners and/or frequencies (Figure 3B; Figure 3-1). This underscores the second point, that *ON CBC coupling partnerships are class-specific*. In the following sections, we expand upon these partnerships in turn.

Canonical heterocellular coupling with Aii cells

Coupling with Aii cells has been presented as a hallmark of mammalian ON CBC identity, despite reports to the contrary in various species (*cat*: Cohen and Sterling, 1990; *rabbit*: Petrides and Trexler, 2008; *mouse*: Tsukamoto and Omi, 2017). Indeed, most rabbit ON CBCs in RC1 form gap junctions with Aii cells (Figure 4A-C). However, we also confirm that some rabbit ON CBCs lack direct coupling with Aii cells (Figure 3B; detailed in Figure 3-1). Cells of the CBb3 class appear to never form gap junctions with Aii cells. This is not due to a lack of opportunity. We have identified six validated contacts between CBb3 axonal processes and the arboreal dendrites of Aii cells. Recaptures of these sites confirm the absence of gap junctions at all six (Figure 4E-H). In fact, two of these contacts lacked any membrane density, while adherens junctions (n = 2) or bipolar conventional synapses (n = 2) were identified at the other four. Both the CBb6 (previously CBb7 class, Marc et al., 2014) and CBbwf cells are also sparsely presynaptic to Aii cells via ribbon synapses. CBb3 cells also lack the canonical inhibition from Aii lobules characteristic of OFF CBCs and clearly stratify below these Aii lobules within the ON sublamina (Figure 4F), fully costratify (Figure 4F) and couple with (Figure 4J) other Aii-coupled ON CBC classes (Figure 4I), supporting their classification within the ON CBC superclass. Three of the six fully reconstructed CBb4 cells are also devoid of gap junctions with Aii cells and the three that do form gap junctions with Aii cells do so infrequently (1-3 gap junctions per cell). These CBb4 cells fully stratify with CBb3 arbors below Aii lobules in the ON sublamina, couple with other Aii-coupled ON CBCs, and are also never postsynaptic to

JNeurosci Accepted Manuscript

588 inhibitory conventional synapses from Aii lobules, arguing that they too belong within the ON CBC
589 superclass.
590
591 ***Noncanonical heterocellular coupling with unclassified ACs***
592 Approximately 8% of the 1339 gap junctions formed by the 37 ON CBCs detailed in this study mediate
593 coupling with AC targets lacking the classical morphology and synaptology of Aii cells (Figure 4K-Q),
594 referred to hereafter as xACs. To date, we have confirmed gap junctions between xACs and only 3 ON
595 CBC classes (CBb3, CBb4, and CBb5) (Figure 3B; detailed in Figure 3-1). CBb3 cells are the primary
596 partner, forming gap junctions with xACs nearly twice as often as any other ON CBC class (8.4 ± 2.2 gap
597 junctions with xACs/CBb3 cell; CV = 0.26; *n* = 5 CBb3 cells). Interestingly, xACs provide the sole source of
598 heterocellular coupling in which the CBb3 class participates. Similarly, CBb4 cells, many of which lack
599 coupling with Aii cells, also form gap junctions with xACs (4.7 ± 3.4 gap junctions with xACs/CBb4 cell; CV
600 = 0.73; *n* = 6 CBb4 cells; Figure 4K-M). Thus, as a consequence of this xAC coupling, all ON CBC classes
601 participate in heterocellular coupling motifs. CBb5 cells were also observed to form gap junctions with
602 xACs (Figure 4N-Q), making them the only class of ON CBCs that participates in both canonical and
603 noncanonical heterocellular coupling.
604
605 The processes of xACs present with medium-to-dark electron dense cytoplasm, irregular lobular
606 varicosities and/or very thin, tortuous extensions. Reconstruction of three of these (and partial
607 reconstruction of several more) suggest at least two separate classes of small diameter (50-100 µm),
608 diffusely-stratified arbors with somas containing high levels of glycine, consistent with narrow-field
609 glycinergic ACs (Figure 4K,N). However, none of these resemble the characteristic morphology of the
610 narrow-field glycinergic A8 AC shown to couple with ON CBCs in mouse (Kolb and Nelson, 1996; Lee et
611 al., 2015; Yadav et al., 2019), despite identification of a homologous A8 cell in rabbit (*DAPI-3*: Vaney,

JNeurosci Accepted Manuscript

1990; Bloomfield, 1992; Wright et al., 1997; or *flat bistratified*: MacNeil and Masland, 1998; Macneil et al., 1999). Moreover, these reconstructed xACs are also inconsistent with the non-GABAergic non-Glycinergic Gbx2+ ACs recently reported to couple with presumed ON CBCs in strata 3 and/or 5 of mouse retina (Kerstein et al., 2019). The coupling profiles of these xACs also supports at least two classes: one that couples with at least CBb3 and CBb4 cells (CBb3n are also candidate partners, but no gap junctions have been confirmed) and a second that may couple exclusively with CBb5 cells. Further classification of these xACs and detailing of their connectomes is beyond the scope of this manuscript, but will be the subject of a future publication.

In-class homocellular coupling among ON CBCs

Coupling among neighboring cells of the same class is a common motif within the retina (Volgyi et al., 2013), although a rarer occurrence among mammalian bipolar cells (Raviola and Gilula, 1975; Kolb, 1979; Cohen and Sterling, 1990; Luo et al., 1999; Mills, 1999; Dacey et al., 2000; Jacoby and Marshak, 2000; Arai et al., 2010; Kantor et al., 2016; Kantor et al., 2017; Tsukamoto and Omi, 2017) than those of lower vertebrates (Marc et al., 1988; Umino et al., 1994; Arai et al., 2010). Here, we find that five of the seven rabbit ON CBC classes form in-class gap junctions (Figure 3B; detailed in Figure 3-1). Overall, in-class gap junctions tend to be less frequent than other coupling modes, but this is not surprising given the limited contact opportunities afforded by tiling among neighboring cells. Both CBb5 and CBb4w classes exhibit the highest frequency of gap junctions mediating in-class partnerships, and both have high coverage factors (CF = 1.25 and 0.92, respectively; Table 1) and nearly perfectly tile the retinal plane (Figure 1D). Recapture of all candidate in-class contacts for a CBb5 cell reveals a single gap junction at virtually every contact with each of its five immediate CBb5 neighbors (*n* = 8/9 contacts; 1/9 inconclusive; Figure 5A-I). Likewise, for two of the six completed CBb4w cells, all in-class contacts with neighbors contain confirmed gap junctions, while the remaining four cells have over 80% of their in-class

JNeurosci Accepted Manuscript

636 gap junctions with neighbors confirmed (the remaining 20% present obliquely). Based on the very high
637 coverage factor (0.98; Table 1) and observed near-perfect tiling (Figure 1D), the CBb3n class was also
638 predicted to have a high frequency of in-class gap junctions. Although branches of neighboring CBb3n
639 cells often contact and form gap junctions (Figure 5J-K), CBb3n cells form half as many gap junctions
640 with in-class neighbors than either the CBb5 or CBb4w classes (Figure 3B). Closer investigation revealed
641 that in many cases, Aii coupling appeared to bridge CBb3n in-class coupling, in which the branches of
642 two neighboring CBb3n cells terminate with gap junctions onto an intervening arboreal dendrite of an
643 Aii cell, often immediately opposite each other, or a short distance apart (Figure 5L-O). In contrast, the
644 relatively high frequency of CBb4 in-class coupling was unexpected in light of the low coverage factor
645 (0.61) leaving large gaps and few opportunities for contact with neighboring CBb4 cells (Figure 1B; Table
646 1). In this case, we discovered that many of the in-class gap junctions are in fact self gap junctions
647 formed between sister branches of the same cell (Figure 3-1). Self gap junctions within other ON CBC
648 classes is rare, except the CBb4w class, which exhibit similar self gap junction frequencies as the CBb4
649 class. Thus, it appears that these ON CBC classes will participate in in-class motifs whenever the
650 opportunity presents. It was therefore surprising to find that while cells of the CBb3 class participate in
651 in-class coupling motifs, they may decline a large portion of coupling opportunities, both with in-class
652 neighbors and between sister branches. Recapture of representative contact sites confirmed the
653 presence of gap junctions at only two of five validated encounters between CBb3 processes originating
654 from neighboring CBb3 cells (Figure 5P-Q) and one of three validated encounters between sister
655 branches.
656
657 This propensity for in-class coupling is not shared among all classes of ON CBCs, and in fact, is in stark
658 contrast to the CBb6 class, which expressly decline in-class coupling opportunities. CBb6 cells also tile
659 the retinal plane affording in-class opportunities, but when processes of neighboring CBb6 cells contact

JNeurosci Accepted Manuscript

each other, gap junctions are never present (*n* = 5 validated instances; Figure 6A-E). Such contact sites often contain adherens junctions (Figure 6C) indicative of cell-cell recognition and the ability to recruit and assemble protein complexes at these sites. The absence of gap junctions at these sites is not due to a lack of connexin trafficking, as gap junctions with Aii cells are often found nearby or even immediately adjacent within the same varicosity (Figure 6A',B,D,E). Importantly, these Aii processes do not intervene, possibly preventing or obviating the contact of CBb6 processes, as seen for many potential CBb3n in-class coupling opportunities. Moreover, unlike the CBb4 class, we have yet to confirm the formation of self gap junctions by CBb6 cells and only a few candidate sites have been identified (*n* = 8 contacts). Like the CBb6 class, CBbwf cells may also decline in-class coupling. With only two identified CBbwf cells, both of which having arbors that extend beyond the boundaries of the RC1 volume, only one in-class contact site has been identified. Despite a discernable membrane density at this site, recaptures of both serial sections containing membrane density clearly revealed the presence of an adherens junction lacking any gap junctional zippering (Figure 6F-H). This lack of in-class coupling is a feature the CBb6 and CBbwf classes share with rod bipolar cells, which were also never observed to form gap junctions within the IPL of RC1 (*n* = 104 cells), despite having a number of contact opportunities within their incomplete packing of the retinal plane (Lauritzen et al., 2019).

Cross-class homocellular coupling among ON CBCs

Cross-class coupling among ON CBCs is extensive, accounting for 78% of the homocellular motifs. Every class of ON CBCs participates in cross-class homocellular coupling with at least one and up to five other classes, although typically dominated by a single cross-class partner (Figure 3B; detailed in Figure 3-1). Consistent with all reported cross-class coupling motifs in other mammalian species (Raviola and Gilula, 1975; Kolb, 1979; Cohen and Sterling, 1990; Luo et al., 1999; Mills, 1999; Dacey et al., 2000; Jacoby and Marshak, 2000; Arai et al., 2010; Kantor et al., 2016; Kantor et al., 2017; Tsukamoto and Omi, 2017),

JNeurosci Accepted Manuscript

684 cross-class coupling motifs of ON CBCs in RC1 respect ON/OFF functional segregation. Coupling between
685 ON CBCs and OFF CBCs was never observed. Importantly, both the CBb3 and CBb4 classes, which exhibit
686 few to zero canonical heterocellular gap junctions with Aii cells, routinely form a large number of cross-
687 class gap junctions with other classes that do participate in this classic ON CBC coupling motif, further
688 supporting the classification of the CBb3 and CBb4 classes within the ON superclass.
689
690 Cross-class coupling opportunities are afforded by the costratification of ON CBC axonal arborizations
691 within the rabbit IPL (Figure 7A). The extensive costratification of the CBb3/3n/4/4w classes within
692 strata 3 and 4 is reflected in their coupling partnerships. All four classes couple with each other (Figure
693 7B-K), with the possible exception of the CBb3 and CBb4w classes with each other (Figure 7L-M).
694 Coupling frequencies among the other class pairings are variable, ranging from averaging a few gap
695 junctions per cell to over 30 per cell (Figure 3B), and suggests that these classes preferentially select
696 some classes over others as coupling partners. In contrast, the more deeply stratifying CBb5/6/wf
697 classes in strata 4 and 5 infrequently form gap junctions with each other, despite also exhibiting
698 significant costratification. For example, the CBb5 and CBb6 arbors theoretically overlap by
699 approximately 75% (but, branches trend deeper as they branch out from the descending axon), yet CBb5
700 cells average 0.3 gap junctions with the CBb6 class (± 0.5 gap junctions; 1.55 CV; *n* = 6 CBb5 cells) and
701 CBb6 cells average 0.8 gap junctions with the CBb5 class (± 0.8 gap junctions; 1.05 CV; *n* = 5 CBb6 cells).
702 Recapture of three instances revealed gap junctions at only two of these sites (Figure 8A-B), suggesting
703 that not all sites of membrane contact contain gap junctions. CBb6 cross-class coupling appears
704 restricted to the CBb5 class, despite costratification with the majority of the CBbwf arbor and five
705 validated contacts (Figure 8C-D). CBbwf arbors also overlap with CBb5 arbors, albeit to a lesser extent
706 than between the CBb5, and exhibit rare instances of coupling (Figure 8E-F). Although the CBb5 class
707 shares roughly 50% arbor overlap with the CBb3, CBb3n, CBb4, and CBb4w classes, formation of gap

JNeurosci Accepted Manuscript

junctions has only been confirmed with CBb3n cells, and at only one of four validated contacts (Figure 8G-J). A single instance of CBb3n coupling with CBb6 was also found (Figure 8K-L), suggesting that the CBb3n class may be fairly indiscriminate towards coupling partners. Together, these data demonstrate that all ON CBC classes participate in cross-class coupling according to clear class-specific rulesets. However, *not all class pairings couple*, even when opportunity is afforded by the laminar organization of the retinal IPL, further demonstrating the specificity of these connections.

Geometric and anatomic opportunities only partially define ON CBC specificity

In the previous section, we detailed the rulesets of ON CBC coupling in the rabbit retina, revealing class-specific differences both in partner choice and frequency. We next sought to examine what confers this specificity. A common strategy for synaptic precision in chemical synapses is the sequential constraint of potential targets, turning connection availability on and off over time (Yogev and Shen, 2014). Initially, developmental processes regulating cell fate determination, cell migration, and the growth and branching of neuronal arbors restrict the pool of potential targets based on geometric and anatomic opportunity, which are later refined through the addition or removal of synapses at contact sites in response to molecular discrimination of partners and/or neural activity. Indeed, the restriction of geometric opportunity by cell spacing and tiling appears to account for much of the specificity observed for in-class coupling patterns. However, the specific rejection of in-class coupling by CBb6 cells, despite opportunity, demonstrates that additional molecular or activity-dependent mechanisms are involved.

Costratification of source and target arbors at specific depths of the IPL is often cited as a driving factor for synaptic precision within the retina. However, the observed stratification patterns in RC1 likely only limits connection availability between CBb6 and CBbwf classes with the shallowly stratified CBb3/3n/4/4w classes and cannot account for the divergence in coupling frequencies among the fully

JNeurosci Accepted Manuscript

732 costratifying CBb3/3n/4/4w classes or CBb5/6/wf classes. To further assess the coupling specificity of
733 cross-class homocellular and heterocellular modes, we examined the frequency of coupling as a function
734 of geometric opportunity afforded by the degree of planar overlap in axonal territory between pairs of
735 cells (the intersection area illustrated in Figure 9A). Importantly, all class pairings exhibited a broad
736 range of intersection areas, even when cell spacing produced large gaps in the tile. Many class pairings
737 exhibited a trend of increased coupling with increased intersection area (Figure 9B), demonstrating that
738 these coupling motifs are often generated according to specific patterns. By extension, this also suggests
739 that the variability in coupling frequencies observed among individual cells of the same class (Figure 3-1)
740 may in part be due to variability in arbor size or distribution within the mosaic or tile. In support of the
741 former, CBb4 595 forms 34 gap junctions with the CBb4w class while CBb4 5292 only forms 19. This 56%
742 reduction in coupling frequency can largely be explained by the fact that CBb4 5292 has approximately
743 50% of the field area as CBb4 595. More importantly, the rate at which coupling frequency increases
744 with intersection area often differs among the different partners of a given ON CBC class, demonstrating
745 that ON CBC classes can have unique patterns with each of their partners, even within coupling modes.
746 Arbor branching patterns differ among the various partner classes and can influence anatomic
747 encounter rates that would in turn contribute to the specific patterns of coupling. While this is difficult
748 to quantify, qualitative evaluation suggests that for at least some class pairings, anatomic encounter
749 rates cannot fully account for the observed specificity. For example, the CBb3n coupling partners, CBb4
750 and CBb4w exhibit nearly identical stratification features, but CBb4 cells have fewer branch terminals
751 and an overall lower branch path complexity, suggesting a lower potential anatomic encounter rate than
752 CBb4w cells with CBb3n. Yet, CBb3n cells are six times as likely to couple with the CBb4 class compared
753 to the CBb4w class. Thus, while the contributions of molecular discrimination and activity-dependent
754 refinement cannot be evaluated here, neither geometric opportunity nor anatomic encounter rates are

JNeurosci Accepted Manuscript

sufficient to fully account for the observed coupling specificity of ON CBC classes, arguing that these other mechanisms are likely involved.

Specificity beyond numerical fractions

Synaptic specificity extends beyond partner choice and frequency (Yogev and Shen, 2014). Class-specific differences in postsynaptic density sizing among chemical synapses based on input source identity or output target identity exist (Lauritzen et al., 2019) and can influence synaptic strength (Minerbi et al., 2009). The positioning of inhibitory synapses can function as powerful veto synapses (Sivyer and Williams, 2013) or provide differential regulation of sodium- versus calcium-dependent action potentials in the same neuron (Miles et al., 1996). Likewise, gap junction size has been shown to correlate with coupling strength (Flores et al., 2012; Szoboszlay et al., 2016), while positioning can facilitate interactions with chemical synapses and regulate current flow (Yang et al., 1990; Pereda, 2014).

Size specificity

ON CBCs form gap junctions varying in plaque area over 200-fold (min = 0.0022 μm^2; max = 0.46 μm^2; mean = 0.041 μm^2 ± 0.053 SD, 1.3 CV; *n* = 1339). The smallest validated gap junction formed by an ON CBC measures 43 nm in diameter and was present on a single section. Freeze-fracture analyses of connexon spacing within gap junction plaques in the IPL of rodent retinas (Raviola and Gilula, 1973, 1975; Reale et al., 1978; Kamasawa et al., 2006) suggests this small gap junction corresponds to a plaque comprised of only three or four connexons across and one to nine connexons deep (3-36 connexons in total). In contrast, the largest identified gap junction exhibits a maximum diameter of 680 nm and spans 11 sections (minimally 900 nm), corresponding to a plaque containing 2050-4600 connexons.

JNeurosci Accepted Manuscript

778 Parsing the size distribution by coupling mode reveals mode-dependent sizing rules. The median size of
779 gap junction plaques formed by ON CBCs with Aii cells is three times greater than those formed with
780 other ON CBCs (Aii partners: median = 0.061 μm^2, n = 404; ON CBC partners: median = 0.017 μm^2, n =
781 825; W = 277973, $p < 2.2E^{-16}$, Wilcoxon rank-sum with continuity correction) and seven times greater
782 than those formed with xACs (median = 0.0084 μm^2, n = 110; W = 42532, $p < 2.2E^{-16}$, Wilcoxon rank-sum
783 with continuity correction). Among homocellular gap junctions, those mediating in-class coupling are
784 larger than their cross-class counterparts (in-class: median = 0.022 μm^2, n = 211; cross-class: median =
785 0.016 μm^2, n = 605; W = 72205, p = 0.0045, Wilcoxon rank-sum with continuity correction). Individual
786 ON CBC classes also exhibit differences in the size distributions for gap junctions mediating different
787 coupling modes (Figure 10A), suggesting these sizing rules are common across all CBC classes. For
788 several classes (CBb3, CBb4, CBb6 and possibly CBbwf), these mode-dependent sizing rules had little
789 effect on a class' relative distribution of gap junctions among its partners (Figure 10B), possibly because
790 these classes are dominated by either a single coupling partner or those of the same mode (e.g. cross-
791 class homocellular partners only). The most striking change was for the CBb3n class, where homocellular
792 partners accounted for 73% of the gap junctions formed by this class, but only 33% of the total gap
793 junctional area. Likewise, Aii coupling accounts for a greater proportion of CBb5 and CBb4w gap
794 junctions when measured as a function of gap junctional area rather than frequency, resulting in
795 canonical heterocellular coupling dominating the CBb5 profile. Additionally, the relatively smaller plaque
796 size of cross-class versus in-class gap junctions formed by the CBb4w class, combined with the larger
797 representation by Aii gap junctions, completely reorders the representation of coupling modes within
798 the CBb4w profile.
799
800 ***Subcellular targeting***

JNeurosci Accepted Manuscript

Subcellular synaptic specificity is abundant in the laminar architecture of the mammalian retina. Synapses and partnerships of the Aii cell are highly compartmentalized. Gap junctions with ON CBCs are restricted to the waist and arboreal dendrites of Aii cells that are positioned within the ON sublamina (Marc et al., 2014). Consistent with this, gap junctions with Aii cells are never observed on the descending axon proximal to the bifurcation that initiates ON CBC terminal arborization (*n* = 404 gap junctions). In fact, such coupling opportunities are specifically rejected between known coupling partners when contact occurs with inappropriate topology (*n* = 2 contacts, Figure 4A-D). In addition, several ON CBCs (*n* = 8 cells: one CBb4w, six CBb5, and one CBb6) extend a single, often short process within the OFF sublamina, well above their primary axonal arborization within the ON sublamina (e.g. CBb5 cell in Figure 1A, 4M; several CBb5 and CBb6 cells in Figure 8), which has also been observed in the cat retina (Cohen and Sterling, 1990). These branches participate in both input and output synapses, but appear to not form gap junctions with Aii cells. However, since we have yet to identify a validated contact, it remains unclear whether these branches would specifically reject these as coupling sites.

The positioning of in-class gap junctions at tip-to-tip or tip-to-shaft topologies is striking (Figure 5). At least one branch terminates in virtually every instance, creating near perfect tiling for several ON CBC classes. Violation of tiling and tip-to-tip or tip-to-shaft topologies is rare with only three instances of significant in-class branch overlap identified in RC1 (CBb5: *n* = 1; CBb3n: *n* = 2; open arrowhead in Figure 5L). In two of the three cases, the offending branches share membrane contact and gap junction at the site of crossing, but in all three cases, these branches then gap junction and terminate upon contact with another process from the same or another class. This observation prompted us to evaluate the potential for spatial rules to govern coupling specificity across ON CBC arbors. Gap junction formation occurs along the full central to peripheral extent of ON CBC arbors (Figure 11). As expected, the distribution of in-class gap junctions tends to be shifted farther from the geometric center than other

JNeurosci Accepted Manuscript

coupling modes. This is likely a consequence of the tip-to-tip or tip-to-shaft topologies of in-class gap junctions obviating the opportunity of an individual branch to form another gap junction after an in-class. The distribution of in-class gap junctions was occasionally more central than the vertices of the convex hull itself, but this likely reflects the poor approximation of ON CBC axonal territories by convex hulls (Marc et al., 2014; Lauritzen et al., 2019). Star domains provide better approximations but are difficult to assess mathematically. Interestingly, the distributions of gap junctions mediating canonical heterocellular coupling with Aii cells were shifted more centrally than those mediating in-class coupling for the CBb4w and CBb5 classes, but not for the CBb3n class, consistent with the previously noted tendency for Aii processes to be positioned between branches of in-class neighbors. Additionally, in the absence of in-class coupling, the distribution of gap junctions mediating Aii coupling appeared to occur with a higher frequency towards the hull vertices. Together these findings support at least a spatial rule for the positioning of in-class gap junctions, although whether their positioning at CBC axonal boundaries are a consequence of, or provide direction for, axonal tiling remains unclear.

Glycine as a marker of ON CBCs

An important feature of gap junctional coupling is the diffusion of small molecules. Indeed, accumulation of the neurotransmitter glycine in ON CBCs is dependent upon heterocellular coupling with glycinergic ACs (Vaney et al., 1998), and glycine is commonly used as a marker to distinguish ON CBCs from OFF CBCs and rod bipolar cells (Cohen and Sterling, 1986; Yang and Yazulla, 1988; Marc et al., 1995; Vaney et al., 1998; Haverkamp and Wassle, 2000; Deans et al., 2002; Marc et al., 2007; c.f. Petrides and Trexler, 2008; Jones et al., 2011; Lauritzen et al., 2013; Jones et al., 2016; Lauritzen et al., 2019),(c.f. Petrides and Trexler, 2008). The Aii cell has long been considered the source of this glycine signal. Evidence for glycine-negative and/or Aii-noncoupled populations of rabbit ON CBCs prompted the suggestion that only directly Aii-coupled ON CBCs accumulate glycine (Petrides and Trexler, 2008). Here,

JNeurosci Accepted Manuscript

we demonstrate that the rabbit CBb3 and CBb4 classes virtually lack gap junctions with Aii cells, but we also reveal that both classes have two alternative routes for glycine diffusion: 1) through direct coupling with glycinergic ACs other than the Aii cell (e.g. glycinergic xACs; Figure 4K-O), or 2) through indirect coupling with Aii cells via gap junctions formed with other ON CBC classes (Figure 3B; Figure 3-1). We therefore wondered whether CBb3 and CBb4 cells would exhibit glycine accumulation. The RC1 dataset uniquely allows quantification of glycine and other small molecule signals in the same cells for which connectivity is mapped (Figure 12A,A'). We observed robust glycine signals in the somas of cells from all seven ON CBC classes, including both the CBb3 and CBb4 classes (Figure 12B). In fact, of all 99 evaluated ON CBC somas, which included 20 CBb3 and 11 CBb4 cells, only one cell did not contain glycine at levels above at least one standard deviation from the mean observed for OFF CBCs. Coupling of this cell (CBb4 364) with an Aii or other glycinergic AC has not been detected, but annotation remains incomplete. The stratification of CBb4 364 and frequent coupling with cells of the CBb4w and CBb3n classes, however, argues that it is not a misclassified OFF CBC or rod bipolar cell and that its classification as a CBb4 is robust. Although the connexin composition and modulation of these gap junctions remains ambiguous, it is clear that at least one of these routes is functional and sufficient to allow accumulation of glycine, consistent with previous discoveries in mouse of functional coupling between ON CBCs and other non-Aii ACs (Farrow et al., 2013; Lee et al., 2015; Kerstein et al., 2019).

ON CBC coupling in retinal networks

In the previous sections we have detailed the class-specific coupling patterns of rabbit ON CBCs. We next sought to place these findings in the context of the larger retinal networks, particularly on the distribution of scotopic signals and the potential mixing of parallel processing streams prior to input to GCs.

JNeurosci Accepted Manuscript

Distribution of rod signals through the Aii cell

Previously, we reported a large-scale connectivity and partnership mapping of Aii cells, including their collection of rod-generated scotopic signals from rod bipolar cell terminals (Marc et al., 2014). However, we did not detail Aii cell output to CBCs with class specificity. Our discovery of class-specific coupling patterns between ON CBCs and Aii cells together with anatomical and physiological reports of differentially weighted Aii output in other species (*cat*: McGuire et al., 1984; Cohen and Sterling, 1990; *rat*: Veruki and Hartveit, 2002a; *mouse*: Tsukamoto and Omi, 2017), prompted a re-examination of the potential signal flow through the scotopic network in the rabbit retina.

The distribution of Aii output to the various ON CBC classes in RC1 was assessed by reanalyzing the coupling partnerships of Aii cells 476, 514, 2610, and 3679 from our previous study (Marc et al., 2014). Each Aii cell forms an average of 114 ± 11 gap junctions (0.12 CV; n = 4 Aii cells). Over 53% of these gap junctions mediate homocellular coupling among Aii cells, and therefore dominate the coupling profile (Figure 13A). This homocellular coupling was found to occur both between neighboring Aii cells and between sister branches of the same Aii cell (Figure 3-1). Although Aii lobular dendrites tile the OFF sublamina, their arboreal dendrites within the ON sublamina extensively overlap, such that any point may be sampled by up to four separate Aii cells (Marc et al., 2014). This affords numerous in-class contact opportunities for homocellular coupling among the arboreal dendrites, and accordingly, these gap junctions are typically not found among the lobular dendrites. Heterocellular coupling with ON CBCs was dominated by three classes, together representing over 86% of the heterocellular gap junctions (36% by CBb6, 32% by CBb3n, and 19% by CBb5). Although the distributions of plaque sizes diverge across the coupled partners, including between different classes of ON CBCs (Figure 13B), these same three ON CBC classes accounted for almost 90% of the total heterocellular gap junction area (Figure 13C). However, the relative representation by these three classes shifted, such that the CBb3n class

JNeurosci Accepted Manuscript

accounts for over half of the heterocellular area, rather than more equal representations by the CBb3n and CBb6 classes when based on gap junction frequency alone (Figure 13C). No gap junctions were found between any of these Aii cells and the CBb3 class and only one candidate has been identified with the CBb4 class (Figure 13A; detailed in Figure 3-1). Importantly, the identity of all but three coupled partners were determined. Of these, only one could be identified as a bipolar cell, but all were found deep within the IPL making it unlikely that any of these partners belong to the CBb3 or CBb4 class.

The Aii cell is also a component of all but one known motif predicted to mediate rod-driven cross-suppression of photopic signals (Lauritzen et al., 2019). In motifs R1, R2 and R25, the activation of Aii-coupled ON CBCs drives narrow and widefield ACs to directly suppress ON CBCs. While the preference of rod inhibitory motifs for the suppression of particular ON CBC classes will require further evaluation, the preferential coupling of Aii cells with specific ON CBC classes, by either numerical counts or cumulative area metrics, suggests that the ON CBC targets of CBb3n, CBb6 and possibly CBb5-driven ACs should provide important insight.

Potential mixing of ON CBC input to GCs

Coupling between ON CBC classes provides numerous potential lateral paths for signal flow (Figure 14A), yet individual CBC classes have long been thought to transmit separate parallel channels of visual information to GCs (Masland, 2001; Euler et al., 2014). While connexin composition and modulation of gating will undoubtably regulate the strength and effect of these lateral paths, we sought to explore their potential impact on GC input. Exploration of this question required analysis beyond the direct coupling of the 37 ON CBCs described in this study and, rather, use of the entire annotated connectivity in the RC1 dataset. Graffinity was developed for rapid visualization and exploration of complex connectivity in large datasets (Kerzner et al., 2017). In an initial exploration of the potential mixing of ON

JNeurosci Accepted Manuscript

CBC signals cross-class coupling may afford, we chose three distinct and well-annotated GCs in RC1. Each receives unique combinations of direct ON CBC drive (→) via ribbon- or bipolar conventional-type synapses (1-hop path: [CBbx → GC]; Figure 14B). Expanding the path length to include direct ON CBC coupling (2-hop path: [CBb :: CBb → GC]), potentially alters the input profile of these GCs in two important ways: First, the number of paths for each direct ON CBC input increased due to the recruitment of neighboring cells via in-class homocellular coupling, indicative of greater synaptic input. Second, and more importantly, cross-class homocellular coupling provides potential paths for indirect signal flow from an additional 2 or 3 ON CBC classes, which likely contribute to the shaping of the output response of the GC's direct ON CBC input class (Demb and Singer, 2016; Kuo et al., 2016). In the case of the transient ON directionally-selective (tON DS) GC 606, which already directly samples broadly from the ON CBC classes, cross- and in-class coupling has the potential to alter the relative path contribution among the ON CBC classes. Further extension of the path length by additional hops eventually reveals paths from all ON CBC classes, as early as three hops for the selected GCs, especially as Aii and CBb3n hubs are incorporated through heterocellular and cross-class coupling, respectively.

DISCUSSION

We report the participation of rabbit ON CBCs in extensive coupling, each forming 20-81 candidate gap junctions (5-25% total axonal synaptic contacts; ≤40% total IPL input/output). Reports in other species suggest ≤20 per cell (≤15% synaptic contact) (*cat*: McGuire et al., 1984; Cohen and Sterling, 1990; *mouse*: Tsukamoto and Omi, 2017). Is rabbit the exception or do species truly differ in their extent of ON CBC coupling? Our approach has the highest base resolution, recapture ability with goniometric tilt, a large contiguous volume for high copy numbers, and a coherent toolset for network exploration, leaving the possibility that extensive coupling is the rule. However, preliminary findings in our comparable mouse volume support species-specific differences in retinal connectivity. More importantly, how do

JNeurosci Accepted Manuscript

these models compare to human? Ultrastructure-based analysis of coupling motifs in humans or nonhuman primates is lacking, and we suggest that 63% of ON CBC gap junctions (77% homocellular; 98% xAC; 24% Aii) are undetectable by traditional light or confocal microscopy. Nonetheless, CX36 colocalization suggests homocellular gap junctions are prominent in human OFF CBC circuitry and possibly ON CBC circuitry as well (Kantor et al., 2017).

Within coupling modes, some features appear conserved while others are species-specific. Like cat (Cohen and Sterling, 1990) and mouse (Tsukamoto and Omi, 2017), rabbit ON CBCs exhibit class-specific Aii coupling frequencies and areas, suggesting differential Aii output to the various ON CBC classes. Similarities with mouse are striking. Three classes (*rabbit*: CBb3n, CBb6, CBb5; *mouse*: T6, T7, T5a) collect the vast majority of Aii output, one completely lacks Aii coupling (*rabbit*: CBb3; *mouse*: T5b) and a second rarely couples (*rabbit*: CBb4; *mouse*: T5c). Moreover, these classes exhibit similar stratification (shallow = strata 3/4 versus deep = strata 4/5). In cat, only one shallow class (b_3) lacks Aii coupling, but uniquely, so does a deep (b_5). Additionally, frequency counts and area measures suggest a differential output preference to deep versus shallow classes in cat, but the converse in rabbit and mouse. Assessments of noncanonical heterocellular AC partners are incomplete, but we identified novel xAC class(es) inconsistent with known mouse AC partners (Kolb and Nelson, 1996; Lee et al., 2015; Kerstein et al., 2019; Yadav et al., 2019). Homocellular coupling varies more. In rabbit, 5/7 classes in-class couple according to axonal tiling patterns, in contrast to a single class in cat and none in mouse, owing to lack of contact. Tiling in macaque (Tsukamoto and Omi, 2016) suggests abundant opportunities for 3/6 classes and in-class coupling was reported for at least one human ON CBC class, despite limited opportunity (Kantor et al., 2017), suggesting in-class coupling may be the rule. Cross-class coupling appears considerably more extensive in rabbit, with all seven classes participating to some extent. Cross-class coupling is generally more pervasive among shallow classes, although robust coupling between the deep

JNeurosci Accepted Manuscript

T6 and T7 classes in mouse is a clear exception. Even in RC1, such gap junctions among the deep classes are sparse (average: <2/cell) and small, possibly causing them to have been missed in previous datasets. Colocalization of CX36 interior to DB6 branch tips and not with Aii processes supports cross-class dominancy in human ON CBC coupling as well (Kantor et al., 2017).

Despite possible divergence in overall coupling extent, the underlying motifs appear fairly conserved, facilitating class correlation across species (Table 3). We define seven classes in rabbit, consistent with previous classification schemes, but contrasting with eight in mouse and five in cat. Notably, comparisons with mouse using morphology or Aii coupling alone yielded incongruent schemes. We prioritized connectivity, as this more likely correlates with function (Vlasits et al., 2019), and underlies the discrepancy between our alignment of cat b_2 with mouse T7 rather than mouse T8 proposed by Tsukamoto and Omi (2017). We also predict the existence of two additional classes in cat retina (b_{3b} and b_{4b}), proposing their resolution by Cohen and Sterling (1990) was limited by small sample sizes and similar Aii connectivity. True functional correlation across species requires additional features. It will be interesting to see how these hold up as additional connectivity and physiology features become available.

Irrespective of species, coupling profiles are class-specific: cells accept and reject unique combinations of Aii and ON CBC partnerships according to robust rulesets. The differences reported here in the frequency, size and spatial distributions of gap junctions across motifs, argue that coupling specificity is as rigorous as chemical synaptic specificity. Costratification is often touted as the critical mechanism conferring specificity within retina, but, as shown here, is a poor indicator of coupling specificity and synaptic specificity in general (e.g. GC 8575, Figure 14). Geometric and anatomic opportunity also fail to confer specificity. Thus, as demonstrated for chemical synaptic precision, including in ON CBCs (Morgan

JNeurosci Accepted Manuscript

et al., 2011; Yogev and Shen, 2014), coupling specificity requires molecular partner discrimination or activity-dependent refinement. Invertebrate innexin-based gap junctions play dual roles, conferring target specificity by acting as “lock and key recognition” factors (Baker and Macagno, 2014). A general lack of connexin diversity and extensive Cx36/45-mediated motifs (Lin et al., 2005; Li et al., 2008; Kantor et al., 2017) opposes a similar role in mammalian ON CBCs.

How might ON CBC coupling influence retinal networks? Uneven distribution of Aii signals to ON CBC classes has clear implications on scotopic signaling (Figure 14A). Some GCs exhibiting high scotopic thresholds appear to lack primary pathway input, relying instead upon secondary (direct rod-cone photoreceptor coupling) and/or tertiary (direct rod-to-CBC synapses) pathways (Deans et al., 2002; Volgyi et al., 2004; Seilheimer et al., 2020). Non-Aii-coupled CBb3 and CBb4 classes may provide the predominant input for such GCs. Alternatively, these classes may not participate in scotopic retinal circuitry at all, as some GCs exhibit only photopic responses (Deans et al., 2002). However, rod-cone coupling is extensive (Owen, 1985; Wu and Yang, 1988; Tsukamoto et al., 2001; Massey, 2008; Asteriti et al., 2017), making it difficult to conceive of CBCs that would not participate in the secondary pathway. Moreover, both CBb3 and CBb4 indirectly couple with Aii cells through other ON CBC classes, although differential regulation, as described for homocellular Aii-Aii and heterocellular Aii-ON CBC coupling (Mills and Massey, 1995; Xia and Mills, 2004; Petrides and Trexler, 2008), may effectively block such paths.

ON CBC coupling also has implications for photopic networks (Figure 14A). Gap junction-mediated photopic signal spread among ON CBCs generates nonlinear amplification of CBC output at chemical synapses to some GCs, increasing GC sensitivity to spatiotemporally correlated stimuli (Kuo et al., 2016). Although we find some ON CBC gap junctions exist in “mixed” (chemical plus electrical) synapses, none

JNeurosci Accepted Manuscript

1017 are with GCs, consistent with the proposition that this modulation occurs through lateral motifs within
1018 the coupled Aii-ON CBC network (Demb and Singer, 2016; Kuo et al., 2016). Indirect coupling mediated
1019 by Aii cells may contribute, as Aii-ON CBC gap junctions are bidirectional (Xin and Bloomfield, 1999;
1020 Trexler et al., 2001; Demb and Singer, 2012), despite ~2-fold rectification (Veruki and Hartveit, 2002a).
1021 However, we reveal potential direct paths through homocellular motifs. Contribution by in-class
1022 coupling is intuitive, or these motifs may facilitate enhanced signal saliency as reported for cone
1023 photoreceptors (DeVries et al., 2002). The mixing of parallel channels afforded by cross-class coupling
1024 could also contribute. Alternatively, mixing may shape more complex temporal output (Euler et al.,
1025 2014) and/or desynchronization (Vervaeke et al., 2010), although sustained and transient classes tend to
1026 segregate with stratification depth (Baden et al., 2013), similar to cross-class coupling. In support of the
1027 latter, oscillations emerge from the Aii-ON CBC network when photoreceptor input is blocked (Trenholm
1028 et al., 2012).
1029
1030 Our method provides no indication of open probability. Moreover, connexin composition (which
1031 remains ambigous, but likely differs between coupling modes - Lin et al., 2005; c.f. Li et al., 2008) and
1032 modulatory mechanisms (which can differ for the same connexin in different cell classes - O'Brien, 2019)
1033 will clearly regulate when and to what degree signals flow along these paths (Veenstra, 1996; Nielsen et
1034 al., 2012). However, effects on network activity are often poorly predicted by coupling coefficients
1035 (Haas, 2015) and even a small fraction of open channels can confer network effects (Curti et al., 2012;
1036 Szoboszlay et al., 2016), including in the coupled CBC network of the retina (Farrow et al., 2013).
1037 Furthermore, coupling effects on networks depend on the spatial and temporal spread of signals and are
1038 therefore dynamic and context-dependent (Alcami and Pereda, 2019). In degenerated retinal networks,
1039 Cx36-expressing gap junctions within the extended Aii-ON CBC network mediate aberrant hyperactivity
1040 contributing to visual impairment (Trenholm et al., 2012; Ivanova et al., 2016), and an elevated fraction

JNeurosci Accepted Manuscript

of phosphorylated CX36 (Ivanova et al., 2015) suggests aberrant opening. Whether this reflects deregulation of normative or novel motifs remains unknown.

Our findings significantly expand the repertoire of motifs within the Aii-ON CBC network, providing additional sites for disruption in disease and possibly therapeutic targeting. Deciphering their contributions is vital to our understanding of visual processing in the retina. Here, we detail the available partnerships, frequencies, sizing and topology for future physiology and modeling studies assessing function.

JNeurosci Accepted Manuscript

REFERENCES

Alcami P, Pereda AE (2019) Beyond plasticity: the dynamic impact of electrical synapses on neural circuits. Nat Rev Neurosci 20:253-271.

Anderson JR, Sigulinsky CL, Nelson NT, Kerzner E (2019) OnBipolarCoupling Code. In.

Anderson JR, Mohammed S, Grimm B, Jones BW, Koshevoy P, Tasdizen T, Whitaker R, Marc RE (2011a) The Viking viewer for connectomics: scalable multi-user annotation and summarization of large volume data sets. J Microsc 241:13-28.

Anderson JR, Jones BW, Yang JH, Shaw MV, Watt CB, Koshevoy P, Spaltenstein J, Jurrus E, U VK, Whitaker RT, Mastronarde D, Tasdizen T, Marc RE (2009) A computational framework for ultrastructural mapping of neural circuitry. PLoS Biol 7:e1000074.

Anderson JR, Jones BW, Watt CB, Shaw MV, Yang JH, Demill D, Lauritzen JS, Lin Y, Rapp KD, Mastronarde D, Koshevoy P, Grimm B, Tasdizen T, Whitaker R, Marc RE (2011b) Exploring the retinal connectome. Mol Vis 17:355-379.

Arai I, Tanaka M, Tachibana M (2010) Active roles of electrically coupled bipolar cell network in the adult retina. J Neurosci 30:9260-9270.

Asteriti S, Gargini C, Cangiano L (2017) Connexin 36 expression is required for electrical coupling between mouse rods and cones. Vis Neurosci 34:E006.

Baden T, Berens P, Bethge M, Euler T (2013) Spikes in mammalian bipolar cells support temporal layering of the inner retina. Curr Biol 23:48-52.

Baker MW, Macagno ER (2014) Control of neuronal morphology and connectivity: emerging developmental roles for gap junctional proteins. FEBS Lett 588:1470-1479.

Baldridge WH, Ball AK, Miller RG (1989) Gap junction particle density of horizontal cells in goldfish retinas lesioned with 6-OHDA. J Comp Neurol 287:238-246.

JNeurosci Accepted Manuscript

1074 Bloomfield SA (1992) Relationship between receptive and dendritic field size of amacrine cells in the
1075 rabbit retina. J Neurophysiol 68:711-725.
1076 Bostock M, Ogievetsky V, Heer J (2011) D(3): Data-Driven Documents. IEEE Trans Vis Comput Graph
1077 17:2301-2309.
1078 Brown SP, Masland RH (1999) Costratification of a population of bipolar cells with the direction-selective
1079 circuitry of the rabbit retina. J Comp Neurol 408:97-106.
1080 Buhl DL, Harris KD, Hormuzdi SG, Monyer H, Buzsaki G (2003) Selective impairment of hippocampal
1081 gamma oscillations in connexin-36 knock-out mouse in vivo. J Neurosci 23:1013-1018.
1082 Cameron S, Rao Y (2010) Molecular mechanisms of tiling and self-avoidance in neural development. Mol
1083 Brain 3:28.
1084 Casini G, Sabatini A, Catalani E, Willems D, Bosco L, Brecha NC (2002) Expression of the neurokinin 1
1085 receptor in the rabbit retina. Neuroscience 115:1309-1321.
1086 Cohen E, Sterling P (1986) Accumulation of (3H)glycine by cone bipolar neurons in the cat retina. J Comp
1087 Neurol 250:1-7.
1088 Cohen E, Sterling P (1990) Demonstration of cell types among cone bipolar neurons of cat retina. Philos
1089 Trans R Soc Lond B Biol Sci 330:305-321.
1090 Cook JE (1996) Spatial properties of retinal mosaics: an empirical evaluation of some existing measures.
1091 Vis Neurosci 13:15-30.
1092 Coulon P, Landisman CE (2017) The Potential Role of Gap Junctional Plasticity in the Regulation of State.
1093 Neuron 93:1275-1295.
1094 Curti S, Hoge G, Nagy JI, Pereda AE (2012) Synergy between electrical coupling and membrane
1095 properties promotes strong synchronization of neurons of the mesencephalic trigeminal
1096 nucleus. J Neurosci 32:4341-4359.

JNeurosci Accepted Manuscript

1097 Dacey D, Packer OS, Diller L, Brainard D, Peterson B, Lee B (2000) Center surround receptive field
1098 structure of cone bipolar cells in primate retina. Vision Res 40:1801-1811.
1099 Das S, Trona F, Khallaf MA, Schuh E, Knaden M, Hansson BS, Sachse S (2017) Electrical synapses mediate
1100 synergism between pheromone and food odors in Drosophila melanogaster. Proc Natl Acad Sci
1101 U S A 114:E9962-E9971.
1102 Deans MR, Volgyi B, Goodenough DA, Bloomfield SA, Paul DL (2002) Connexin36 is essential for
1103 transmission of rod-mediated visual signals in the mammalian retina. Neuron 36:703-712.
1104 Demb JB, Singer JH (2012) Intrinsic properties and functional circuitry of the AII amacrine cell. Vis
1105 Neurosci 29:51-60.
1106 Demb JB, Singer JH (2016) Mind the Gap Junctions: The Importance of Electrical Synapses to Visual
1107 Processing. Neuron 90:207-209.
1108 DeVries SH, Qi X, Smith R, Makous W, Sterling P (2002) Electrical coupling between mammalian cones.
1109 Curr Biol 12:1900-1907.
1110 Elliott H, Fischer RS, Myers KA, Desai RA, Gao L, Chen CS, Adelstein RS, Waterman CM, Danuser G (2015)
1111 Myosin II controls cellular branching morphogenesis and migration in three dimensions by
1112 minimizing cell-surface curvature. Nat Cell Biol 17:137-147.
1113 Euler T, Haverkamp S, Schubert T, Baden T (2014) Retinal bipolar cells: elementary building blocks of
1114 vision. Nat Rev Neurosci 15:507-519.
1115 Famiglietti EV, Jr. (1981) Functional architecture of cone bipolar cells in mammalian retina. Vision Res
1116 21:1559-1563.
1117 Farrow K, Teixeira M, Szikra T, Viney TJ, Balint K, Yonehara K, Roska B (2013) Ambient illumination
1118 toggles a neuronal circuit switch in the retina and visual perception at cone threshold. Neuron
1119 78:325-338.

JNeurosci Accepted Manuscript

1120 Flores CE, Nannapaneni S, Davidson KG, Yasumura T, Bennett MV, Rash JE, Pereda AE (2012) Trafficking
1121 of gap junction channels at a vertebrate electrical synapse in vivo. Proc Natl Acad Sci U S A
1122 109:E573-582.
1123 Frisch C, De Souza-Silva MA, Sohl G, Guldenagel M, Willecke K, Huston JP, Dere E (2005) Stimulus
1124 complexity dependent memory impairment and changes in motor performance after deletion of
1125 the neuronal gap junction protein connexin36 in mice. Behav Brain Res 157:177-185.
1126 Greene MJ, Kim JS, Seung HS, EyeWirers (2016) Analogous Convergence of Sustained and Transient
1127 Inputs in Parallel On and Off Pathways for Retinal Motion Computation. Cell Rep 14:1892-1900.
1128 Grueber WB, Sagasti A (2010) Self-avoidance and tiling: Mechanisms of dendrite and axon spacing. Cold
1129 Spring Harb Perspect Biol 2:a001750.
1130 Guldenagel M, Ammermuller J, Feigenspan A, Teubner B, Degen J, Sohl G, Willecke K, Weiler R (2001)
1131 Visual transmission deficits in mice with targeted disruption of the gap junction gene
1132 connexin36. J Neurosci 21:6036-6044.
1133 Haas JS (2015) A new measure for the strength of electrical synapses. Front Cell Neurosci 9:378.
1134 Haverkamp S, Wassle H (2000) Immunocytochemical analysis of the mouse retina. J Comp Neurol 424:1-
1135 23.
1136 Haverkamp S, Wassle H, Duebel J, Kuner T, Augustine GJ, Feng G, Euler T (2005) The primordial, blue-
1137 cone color system of the mouse retina. J Neurosci 25:5438-5445.
1138 Helmstaedter M, Briggman KL, Turaga SC, Jain V, Seung HS, Denk W (2013) Connectomic reconstruction
1139 of the inner plexiform layer in the mouse retina. Nature 500:168-174.
1140 Hormuzdi SG, Pais I, LeBeau FE, Towers SK, Rozov A, Buhl EH, Whittington MA, Monyer H (2001)
1141 Impaired electrical signaling disrupts gamma frequency oscillations in connexin 36-deficient
1142 mice. Neuron 31:487-495.

JNeurosci Accepted Manuscript

1143 Ivanova E, Yee CW, Sagdullaev BT (2015) Increased phosphorylation of Cx36 gap junctions in the AII
1144 amacrine cells of RD retina. Front Cell Neurosci 9:390.
1145 Ivanova E, Yee CW, Baldoni R, Jr., Sagdullaev BT (2016) Aberrant activity in retinal degeneration impairs
1146 central visual processing and relies on Cx36-containing gap junctions. Exp Eye Res 150:81-89.
1147 Jacoby RA, Marshak DW (2000) Synaptic connections of DB3 diffuse bipolar cell axons in macaque
1148 retina. J Comp Neurol 416:19-29.
1149 Jan YN, Jan LY (2010) Branching out: mechanisms of dendritic arborization. Nat Rev Neurosci 11:316-
1150 328.
1151 Jeon CJ, Masland RH (1995) A population of wide-field bipolar cells in the rabbit's retina. J Comp Neurol
1152 360:403-412.
1153 Jones BW, Pfeiffer RL, Ferrell WD, Watt CB, Marmor M, Marc RE (2016) Retinal remodeling in human
1154 retinitis pigmentosa. Exp Eye Res 150:149-165.
1155 Jones BW, Watt CB, Frederick JM, Baehr W, Chen CK, Levine EM, Milam AH, Lavail MM, Marc RE (2003)
1156 Retinal remodeling triggered by photoreceptor degenerations. J Comp Neurol 464:1-16.
1157 Jones BW, Kondo M, Terasaki H, Watt CB, Rapp K, Anderson J, Lin Y, Shaw MV, Yang JH, Marc RE (2011)
1158 Retinal remodeling in the Tg P347L rabbit, a large-eye model of retinal degeneration. J Comp
1159 Neurol 519:2713-2733.
1160 Kalloniatis M, Marc RE, Murry RF (1996) Amino acid signatures in the primate retina. J Neurosci 16:6807-
1161 6829.
1162 Kamasawa N, Furman CS, Davidson KG, Sampson JA, Magnie AR, Gebhardt BR, Kamasawa M, Yasumura
1163 T, Zumbrunnen JR, Pickard GE, Nagy JI, Rash JE (2006) Abundance and ultrastructural diversity of
1164 neuronal gap junctions in the OFF and ON sublaminae of the inner plexiform layer of rat and
1165 mouse retina. Neuroscience 142:1093-1117.

JNeurosci Accepted Manuscript

1166 Kantor O, Varga A, Nitschke R, Naumann A, Enzsoly A, Lukats A, Szabo A, Nemeth J, Volgyi B (2017)
1167 Bipolar cell gap junctions serve major signaling pathways in the human retina. Brain Struct Funct
1168 222:2603-2624.
1169 Kantor O, Benko Z, Enzsoly A, David C, Naumann A, Nitschke R, Szabo A, Palfi E, Orban J, Nyitrai M,
1170 Nemeth J, Szel A, Lukats A, Volgyi B (2016) Characterization of connexin36 gap junctions in the
1171 human outer retina. Brain Struct Funct 221:2963-2984.
1172 Kawano T, Po MD, Gao S, Leung G, Ryu WS, Zhen M (2011) An imbalancing act: gap junctions reduce the
1173 backward motor circuit activity to bias C. elegans for forward locomotion. Neuron 72:572-586.
1174 Kerstein PC, Leffler J, Sivyer B, Taylor WR, Wright KM (2019) Gbx2 identifies and regulates the
1175 development of an atypical amacrine cell in the mouse retina. Investigative Ophthalmology &
1176 Visual Science 60:541-541.
1177 Kerzner E, Lex A, Sigulinsky CL, Umess T, Jones BW, Marc RE, Meyer M (2017) Graffinity: Visualizing
1178 Connectivity in Large Graphs. Comput Graph Forum 36:251-260.
1179 Kihara AH, Mantovani de Castro L, Belmonte MA, Yan CY, Moriscot AS, Hamassaki DE (2006) Expression
1180 of connexins 36, 43, and 45 during postnatal development of the mouse retina. J Neurobiol
1181 66:1397-1410.
1182 Kohler K, Kolbinger W, Kurz-Isler G, Weiler R (1990) Endogenous dopamine and cyclic events in the fish
1183 retina, II: Correlation of retinomotor movement, spinule formation, and connexon density of gap
1184 junctions with dopamine activity during light/dark cycles. Vis Neurosci 5:417-428.
1185 Kolb H (1979) The inner plexiform layer in the retina of the cat: electron microscopic observations. J
1186 Neurocytol 8:295-329.
1187 Kolb H, Famiglietti EV (1974) Rod and cone pathways in the inner plexiform layer of cat retina. Science
1188 186:47-49.

JNeurosci Accepted Manuscript

1189 Kolb H, Nelson R (1996) Hyperpolarizing, small-field, amacrine cells in cone pathways of cat retina.
1190 Journal of Comparative Neurology 371:415-436.
1191 Kuo SP, Schwartz GW, Rieke F (2016) Nonlinear Spatiotemporal Integration by Electrical and Chemical
1192 Synapses in the Retina. Neuron 90:320-332.
1193 Kurz-Isler G, Wolburg H (1986) Gap junctions between horizontal cells in the cyprinid fish alter rapidly
1194 their structure during light and dark adaptation. Neurosci Lett 67:7-12.
1195 Kurz-Isler G, Wolburg H (1988) Light-dependent dynamics of gap junctions between horizontal cells in
1196 the retina of the crucian carp. Cell Tissue Res 251:641-649.
1197 Kurz-Isler G, Voigt T, Wolburg H (1992) Modulation of connexon densities in gap junctions of horizontal
1198 cell perikarya and axon terminals in fish retina: effects of light/dark cycles, interruption of the
1199 optic nerve and application of dopamine. Cell Tissue Res 268:267-275.
1200 Lauritzen JS, Anderson JR, Jones BW, Watt CB, Mohammed S, Hoang JV, Marc RE (2013) ON cone bipolar
1201 cell axonal synapses in the OFF inner plexiform layer of the rabbit retina. J Comp Neurol
1202 521:977-1000.
1203 Lauritzen JS, Sigulinsky CL, Anderson JR, Kalloniatis M, Nelson NT, Emrich DP, Rapp C, McCarthy N,
1204 Kerzner E, Meyer M, Jones BW, Marc RE (2019) Rod-cone crossover connectome of mammalian
1205 bipolar cells. J Comp Neurol 527:87-116.
1206 Lee SCS, Meyer A, Schubert T, Huser L, Dedek K, Haverkamp S (2015) Morphology and connectivity of
1207 the small bistratified A8 amacrine cell in the mouse retina. Journal of Comparative Neurology
1208 523:1529-1547.
1209 Lefebvre JL (2017) Neuronal territory formation by the atypical cadherins and clustered protocadherins.
1210 Semin Cell Dev Biol 69:111-121.
1211 Li X, Kamasawa N, Ciolofan C, Olson CO, Lu S, Davidson KG, Yasumura T, Shigemoto R, Rash JE, Nagy JI
1212 (2008) Connexin45-containing neuronal gap junctions in rodent retina also contain connexin36

JNeurosci Accepted Manuscript

1213 in both apposing hemiplaques, forming bihomotypic gap junctions, with scaffolding contributed
1214 by zonula occludens-1. J Neurosci 28:9769-9789.
1215 Lin B, Jakobs TC, Masland RH (2005) Different functional types of bipolar cells use different gap-
1216 junctional proteins. J Neurosci 25:6696-6701.
1217 Long MA, Landisman CE, Connors BW (2004) Small clusters of electrically coupled neurons generate
1218 synchronous rhythms in the thalamic reticular nucleus. J Neurosci 24:341-349.
1219 Luo X, Ghosh KK, Martin PR, Grunert U (1999) Analysis of two types of cone bipolar cells in the retina of
1220 a New World monkey, the marmoset, Callithrix jacchus. Vis Neurosci 16:707-719.
1221 MacNeil MA, Masland RH (1998) Extreme diversity among amacrine cells: Implications for function.
1222 Neuron 20:971-982.
1223 MacNeil MA, Gaul PA (2008) Biocytin wide-field bipolar cells in rabbit retina selectively contact blue
1224 cones. J Comp Neurol 506:6-15.
1225 Macneil MA, Heussy JK, Dacheux RF, Raviola E, Masland RH (1999) The shapes and numbers of amacrine
1226 cells: Matching of photofilled with Golgi-stained cells in the rabbit retina and comparison with
1227 other mammalian species. Journal of Comparative Neurology 413:305-326.
1228 MacNeil MA, Heussy JK, Dacheux RF, Raviola E, Masland RH (2004) The population of bipolar cells in the
1229 rabbit retina. J Comp Neurol 472:73-86.
1230 Marc R (2009) Functional Neuroanatomy of the Retina. In: Duane's Ophthalmology (Tasman W, Jaeger
1231 EA, eds). Philadelphia, United States: Lippincott Williams and Wilkins.
1232 Marc RE (1999) Kainate activation of horizontal, bipolar, amacrine, and ganglion cells in the rabbit
1233 retina. J Comp Neurol 407:65-76.
1234 Marc RE, Liu WL (1984) Horizontal cell synapses onto glycine-accumulating interplexiform cells. Nature
1235 312:266-269.
1236 Marc RE, Jones BW (2002) Molecular phenotyping of retinal ganglion cells. J Neurosci 22:413-427.

JNeurosci Accepted Manuscript

1237 Marc RE, Jones BW (2003) Retinal remodeling in inherited photoreceptor degenerations. Mol Neurobiol
1238 28:139-147.
1239 Marc RE, Liu WL, Muller JF (1988) Gap junctions in the inner plexiform layer of the goldfish retina. Vision
1240 Res 28:9-24.
1241 Marc RE, Murry RF, Basinger SF (1995) Pattern recognition of amino acid signatures in retinal neurons. J
1242 Neurosci 15:5106-5129.
1243 Marc RE, Anderson JR, Jones BW, Sigulinsky CL, Lauritzen JS (2014) The AII amacrine cell connectome: a
1244 dense network hub. Front Neural Circuits 8:104.
1245 Marc RE, Jones BW, Watt CB, Anderson JR, Sigulinsky C, Lauritzen S (2013) Retinal connectomics:
1246 Towards complete, accurate networks. Prog Retin Eye Res 37:141-162.
1247 Marc RE, Sigulinsky CL, Pfeiffer RL, Emrich D, Anderson JR, Jones BW (2018) Heterocellular Coupling
1248 Between Amacrine Cells and Ganglion Cells. Front Neural Circuits 12:90.
1249 Marc RE, Jones BW, Anderson JR, Kinard K, Marshak DW, Wilson JH, Wensel T, Lucas RJ (2007) Neural
1250 reprogramming in retinal degeneration. Invest Ophthalmol Vis Sci 48:3364-3371.
1251 Marder E (1998) Electrical synapses: beyond speed and synchrony to computation. Curr Biol 8:R795-797.
1252 Marsh AJ, Michel JC, Adke AP, Heckman EL, Miller AC (2017) Asymmetry of an Intracellular Scaffold at
1253 Vertebrate Electrical Synapses. Curr Biol 27:3561-3567 e3564.
1254 Masland RH (2001) The fundamental plan of the retina. Nat Neurosci 4:877-886.
1255 Massey SC (2008) Circuit functions of gap junctions in the mammalian retina. In: The Senses: Vision
1256 (Masland RH, Albright T, eds), pp 457-472. Oxford: Elsevier.
1257 Massey SC, Mills SL (1996) A calbindin-immunoreactive cone bipolar cell type in the rabbit retina. J
1258 Comp Neurol 366:15-33.
1259 Maxeiner S, Dedek K, Janssen-Bienhold U, Ammermuller J, Brune H, Kirsch T, Pieper M, Degen J, Kruger
1260 O, Willecke K, Weiler R (2005) Deletion of connexin45 in mouse retinal neurons disrupts the

JNeurosci Accepted Manuscript

rod/cone signaling pathway between AII amacrine and ON cone bipolar cells and leads to impaired visual transmission. J Neurosci 25:566-576.

McGillem GS, Dacheux RF (2001) Rabbit cone bipolar cells: correlation of their morphologies with whole-cell recordings. Vis Neurosci 18:675-685.

McGuire BA, Stevens JK, Sterling P (1984) Microcircuitry of bipolar cells in cat retina. J Neurosci 4:2920-2938.

Miles R, Toth K, Gulyas AI, Hajos N, Freund TF (1996) Differences between somatic and dendritic inhibition in the hippocampus. Neuron 16:815-823.

Miller AC, Whitebirch AC, Shah AN, Marsden KC, Granato M, O'Brien J, Moens CB (2017) A genetic basis for molecular asymmetry at vertebrate electrical synapses. Elife 6.

Mills SL (1999) Unusual coupling patterns of a cone bipolar cell in the rabbit retina. Vis Neurosci 16:1029-1035.

Mills SL, Massey SC (1995) Differential properties of two gap junctional pathways made by AII amacrine cells. Nature 377:734-737.

Minerbi A, Kahana R, Goldfeld L, Kaufman M, Marom S, Ziv NE (2009) Long-term relationships between synaptic tenacity, synaptic remodeling, and network activity. PLoS Biol 7:e1000136.

Morgan JL, Soto F, Wong RO, Kerschensteiner D (2011) Development of cell type-specific connectivity patterns of converging excitatory axons in the retina. Neuron 71:1014-1021.

Mountoufaris G, Canzio D, Nwakeze CL, Chen WV, Maniatis T (2018) Writing, Reading, and Translating the Clustered Protocadherin Cell Surface Recognition Code for Neural Circuit Assembly. Annu Rev Cell Dev Biol 34:471-493.

Nagy JI, Lynn BD (2018) Structural and Intermolecular Associations Between Connexin36 and Protein Components of the Adherens Junction-Neuronal Gap Junction Complex. Neuroscience 384:241-261.

JNeurosci Accepted Manuscript

1285 Nagy JI, Pereda AE, Rash JE (2018) Electrical synapses in mammalian CNS: Past eras, present focus and
1286 future directions. Biochim Biophys Acta Biomembr 1860:102-123.
1287 Nielsen MS, Axelsen LN, Sorgen PL, Verma V, Delmar M, Holstein-Rathlou NH (2012) Gap junctions.
1288 Compr Physiol 2:1981-2035.
1289 O'Brien J (2019) Design principles of electrical synaptic plasticity. Neurosci Lett 695:4-11.
1290 Owen WG (1985) Chemical and electrical synapses between photoreceptors in the retina of the turtle,
1291 Chelydra serpentina. J Comp Neurol 240:423-433.
1292 Pereda AE (2014) Electrical synapses and their functional interactions with chemical synapses. Nat Rev
1293 Neurosci 15:250-263.
1294 Pereda AE, Curti S, Hoge G, Cachope R, Flores CE, Rash JE (2013) Gap junction-mediated electrical
1295 transmission: regulatory mechanisms and plasticity. Biochim Biophys Acta 1828:134-146.
1296 Peters A (1962) Plasma membrane contacts in the central nervous system. J Anat 96:237-248.
1297 Petrides A, Trexler EB (2008) Differential output of the high-sensitivity rod photoreceptor: AII amacrine
1298 pathway. J Comp Neurol 507:1653-1662.
1299 Pignatelli V, Strettoi E (2004) Bipolar cells of the mouse retina: a gene gun, morphological study. J Comp
1300 Neurol 476:254-266.
1301 Pourcho RG, Goebel DJ (1987) A combined Golgi and autoradiographic study of 3H-glycine-accumulating
1302 cone bipolar cells in the cat retina. J Neurosci 7:1178-1188.
1303 Pow DV, Hendrickson AE (2000) Expression of glycine and the glycine transporter Glyt-1 in the
1304 developing rat retina. Vis Neurosci 17:1R-9R.
1305 Rash JE, Curti S, Vanderpool KG, Kamasawa N, Nannapaneni S, Palacios-Prado N, Flores CE, Yasumura T,
1306 O'Brien J, Lynn BD, Bukauskas FF, Nagy JI, Pereda AE (2013) Molecular and functional asymmetry
1307 at a vertebrate electrical synapse. Neuron 79:957-969.

JNeurosci Accepted Manuscript

1308 Raviola E, Gilula NB (1973) Gap junctions between photoreceptor cells in the vertebrate retina. Proc Natl
1309 Acad Sci U S A 70:1677-1681.
1310 Raviola E, Gilula NB (1975) Intramembrane organization of specialized contacts in the outer plexiform
1311 layer of the retina. A freeze-fracture study in monkeys and rabbits. J Cell Biol 65:192-222.
1312 Reale E, Luciano L, Spitznas M (1978) Communicating junctions of the human sensory retina. A freeze-
1313 fracture study. Albrecht Von Graefes Arch Klin Exp Ophthalmol 208:77-92.
1314 Reese BE (2008) Mosaics, tiling and coverage by retinal neurons. In: The Senses: Vision (Masland RH,
1315 Albright T, eds), pp 439-456. Oxford: Elsevier.
1316 Saint-Amant L, Drapeau P (2001) Synchronization of an embryonic network of identified spinal
1317 interneurons solely by electrical coupling. Neuron 31:1035-1046.
1318 Seilheimer RL, Sabharwal J, Wu SM (2020) Genetic dissection of rod and cone pathways mediating light
1319 responses and receptive fields of ganglion cells in the mouse retina. Vision Res 167:15-23.
1320 Shekhar K, Lapan SW, Whitney IE, Tran NM, Macosko EZ, Kowalczyk M, Adiconis X, Levin JZ, Nemesh J,
1321 Goldman M, McCarroll SA, Cepko CL, Regev A, Sanes JR (2016) Comprehensive Classification of
1322 Retinal Bipolar Neurons by Single-Cell Transcriptomics. Cell 166:1308-1323 e1330.
1323 Sivyer B, Williams SR (2013) Direction selectivity is computed by active dendritic integration in retinal
1324 ganglion cells. Nat Neurosci 16:1848-1856.
1325 Strettoi E, Raviola E, Dacheux RF (1992) Synaptic connections of the narrow-field, bistratified rod
1326 amacrine cell (AII) in the rabbit retina. J Comp Neurol 325:152-168.
1327 Strettoi E, Dacheux RF, Raviola E (1994) Cone bipolar cells as interneurons in the rod pathway of the
1328 rabbit retina. J Comp Neurol 347:139-149.
1329 Szoboszlay M, Lorincz A, Lanore F, Vervaeke K, Silver RA, Nusser Z (2016) Functional Properties of
1330 Dendritic Gap Junctions in Cerebellar Golgi Cells. Neuron 90:1043-1056.

JNeurosci Accepted Manuscript

1331 Trenholm S, Borowska J, Zhang J, Hoggarth A, Johnson K, Barnes S, Lewis TJ, Awatramani GB (2012)
1332 Intrinsic oscillatory activity arising within the electrically coupled AII amacrine-ON cone bipolar
1333 cell network is driven by voltage-gated Na+ channels. J Physiol 590:2501-2517.
1334 Trexler EB, Li W, Mills SL, Massey SC (2001) Coupling from AII amacrine cells to ON cone bipolar cells is
1335 bidirectional. J Comp Neurol 437:408-422.
1336 Tsukamoto Y, Omi N (2014) Some OFF bipolar cell types make contact with both rods and cones in
1337 macaque and mouse retinas. Front Neuroanat 8:105.
1338 Tsukamoto Y, Omi N (2016) ON Bipolar Cells in Macaque Retina: Type-Specific Synaptic Connectivity with
1339 Special Reference to OFF Counterparts. Front Neuroanat 10:104.
1340 Tsukamoto Y, Omi N (2017) Classification of Mouse Retinal Bipolar Cells: Type-Specific Connectivity with
1341 Special Reference to Rod-Driven AII Amacrine Pathways. Front Neuroanat 11:92.
1342 Tsukamoto Y, Morigiwa K, Ueda M, Sterling P (2001) Microcircuits for night vision in mouse retina. J
1343 Neurosci 21:8616-8623.
1344 Umino O, Maehara M, Hidaka S, Kita S, Hashimoto Y (1994) The network properties of bipolar-bipolar
1345 cell coupling in the retina of teleost fishes. Vis Neurosci 11:533-548.
1346 Uylings HB, van Pelt J (2002) Measures for quantifying dendritic arborizations. Network 13:397-414.
1347 Vaney DI (1990) The mosaic of amacrine cells in the mammalian retina. In: Progress in Retinal Research
1348 (Osborne NN, Chader G, eds), pp 49-100. Oxford: Pergamon Press.
1349 Vaney DI (1997) Neuronal coupling in rod-signal pathways of the retina. Invest Ophthalmol Vis Sci
1350 38:267-273.
1351 Vaney DI, Nelson JC, Pow DV (1998) Neurotransmitter coupling through gap junctions in the retina. J
1352 Neurosci 18:10594-10602.
1353 Veenstra RD (1996) Size and selectivity of gap junction channels formed from different connexins. J
1354 Bioenerg Biomembr 28:327-337.

JNeurosci Accepted Manuscript

1355 Veenstra RD, Wang HZ, Beblo DA, Chilton MG, Harris AL, Beyer EC, Brink PR (1995) Selectivity of
1356 connexin-specific gap junctions does not correlate with channel conductance. Circ Res 77:1156-
1357 1165.
1358 Veruki ML, Hartveit E (2002a) Electrical synapses mediate signal transmission in the rod pathway of the
1359 mammalian retina. J Neurosci 22:10558-10566.
1360 Veruki ML, Hartveit E (2002b) AII (Rod) amacrine cells form a network of electrically coupled
1361 interneurons in the mammalian retina. Neuron 33:935-946.
1362 Vervaeke K, Lorincz A, Gleeson P, Farinella M, Nusser Z, Silver RA (2010) Rapid desynchronization of an
1363 electrically coupled interneuron network with sparse excitatory synaptic input. Neuron 67:435-
1364 451.
1365 Vlasits AL, Euler T, Franke K (2019) Function first: classifying cell types and circuits of the retina. Curr
1366 Opin Neurobiol 56:8-15.
1367 Volgyi B, Deans MR, Paul DL, Bloomfield SA (2004) Convergence and segregation of the multiple rod
1368 pathways in mammalian retina. J Neurosci 24:11182-11192.
1369 Volgyi B, Kovacs-Oller T, Atlasz T, Wilhelm M, Gabriel R (2013) Gap junctional coupling in the vertebrate
1370 retina: variations on one theme? Prog Retin Eye Res 34:1-18.
1371 Washioka H, Watanabe H, Negishi K, Tonosaki A (1991) Horizontal-cell gap junction in the goldfish
1372 retina: area and density of particles as revealed by complementary freeze replicas. Arch Histol
1373 Cytol 54:181-188.
1374 Wassle H, Riemann HJ (1978) The mosaic of nerve cells in the mammalian retina. Proc R Soc Lond B Biol
1375 Sci 200:441-461.
1376 Wassle H, Puller C, Muller F, Haverkamp S (2009) Cone contacts, mosaics, and territories of bipolar cells
1377 in the mouse retina. J Neurosci 29:106-117.

JNeurosci Accepted Manuscript

1378 Wright LL, Macqueen CL, Elston GN, Young HM, Pow DV, Vaney DI (1997) The DAPI-3 amacrine cells of
1379 the rabbit retina. Vis Neurosci 14:473-492.
1380 Wu SM, Yang XL (1988) Electrical coupling between rods and cones in the tiger salamander retina. Proc
1381 Natl Acad Sci U S A 85:275-278.
1382 Xia XB, Mills SL (2004) Gap junctional regulatory mechanisms in the AII amacrine cell of the rabbit retina.
1383 Vis Neurosci 21:791-805.
1384 Xin D, Bloomfield SA (1999) Comparison of the responses of AII amacrine cells in the dark- and light-
1385 adapted rabbit retina. Vis Neurosci 16:653-665.
1386 Yadav SC, Tetenborg S, Dedek K (2019) Gap Junctions in A8 Amacrine Cells Are Made of Connexin36 but
1387 Are Differently Regulated Than Gap Junctions in AII Amacrine Cells. Front Mol Neurosci 12:99.
1388 Yang CY, Yazulla S (1988) Light microscopic localization of putative glycinergic neurons in the larval tiger
1389 salamander retina by immunocytochemical and autoradiographical methods. J Comp Neurol
1390 272:343-357.
1391 Yang XD, Korn H, Faber DS (1990) Long-term potentiation of electrotonic coupling at mixed synapses.
1392 Nature 348:542-545.
1393 Yogev S, Shen K (2014) Cellular and molecular mechanisms of synaptic specificity. Annu Rev Cell Dev Biol
1394 30:417-437.

1395

1396

JNeurosci Accepted Manuscript

TABLES/TABLE LEGENDS

JNeurosci Accepted Manuscript

1398 Table 1. Morphometric features of rabbit ON CBC classes.

Class	# of identified cells	Density (cells/mm^2)	Stratification depth (%IPL)	Axonal field area (µm^2)	Max axonal diameter (µm)	# of branch terminals/cell	Branch path complexity[1]	CF[2]	CR
CBb3	29 (5 incomplete)	784	45 - 75	1059 ± 192 SD, 0.18 CV	44 ± 5 SD, 0.11 CV	51.4 ± 12.6 SD, 0.26 CV	8.6 ± 1.0 SD, 0.11 CV	0.83	3.52
CBb3n	47 (8 incomplete)	1101	44 - 69	895 ± 200 SD, 0.22 CV	40 ± 5 SD, 0.12 CV	28 ± 6.5 SD, 0.23 CV	7.1 ± 0.8 SD, 0.11 CV	0.98	3.92
CBb4	18 (4 incomplete)	505	44 - 73	1215 ± 328 SD, 0.27 CV	49 ± 9 SD, 0.18 CV	18.5 ± 3.6 SD, 0.20 CV	6.0 ± 0.8 SD, 0.14 CV	0.61	5.72
CBb4w	19 (9 incomplete)	394	45 – 72	2186 ± 297 SD, 0.14 CV	67 ± 7 SD, 0.10 CV	21.7 ± 3.6 SD, 0.17 CV	6.5 ±0.4 SD, 0.06 CV	0.92	3.32
CBb5	24 (5 incomplete)	725	59 - 86	1676 ± 318 SD, 0.19 CV	59 ± 5 SD, 0.09 CV	29.5 ± 5.6 SD, 0.19 CV	7.4 ± 1.3 SD, 0.18	1.25	2.45
CBb6	17 (7 incomplete)	719	65 - 95	1223 ± 112 SD, 0.09 CV	51 ± 6 SD, 0.11 CV	24.2 ± 8.6 SD, 0.35 CV	6.8 ± 1.5 SD, 0.22 CV	0.88	3.44
CBbwf	2 (2 incomplete)	n.d.	62 - 105	>3800	>100	n.d.	n.d.	n.d.	n.d.

1399

1400 [1]Branch path complexity per Elliott and colleagues (2015). [2]Coverage factor (CF) for axonal arbors within the IPL were computed as the product of the average
1401 axonal field area (mm^2/cell) and the class density (cells/mm^2). Idealized patterns include: 1) *packings*: CF < 1, arbors do not overlap, but possible gaps; 2)
1402 *coverings*: CF > 1, arbors do not leave gaps, but may overlap; 3) *tilings*: CF = 1, arbors neither overlap nor leave gaps (Marc, 2009). Abbreviations: CF,
1403 coverage factor; CR, conformity ratio; *n.d.* not determined.

JNeurosci Accepted Manuscript

1404 Table 2. Synaptology of core set of ON CBC axonal arbors.

Cell ID	Class	# PSDs	# Ribbons	# BCSs	# GJs (confirmed)[1]	% Synaptic Contact	% Total input	% Total output	% Total channel area[3] (um^2)
909	CBb3	131	177	47	48 (19)	11.9	26.8	17.6	7.0
3756	CBb3	161	215	39	64 (16)	13.4	28.4	20.1	8.1
5278	CBb3	111	136	28	31 (10)	10.1	21.8	15.9	4.6
5297	CBb3	111	166	21	45 (10)	13.1	28.8	19.4	7.6
5531	CBb3	131	215	34	51 (13)	11.8	28.0	17.0	9.0
	CBb3 Class	**129 ± 20, 0.16 CV**	**182 ± 34, 0.19 CV**	**34 ± 10, 0.30 CV**	**48 ± 12, 0.25 CV**	**12.3 ± 1.4, 0.11 CV**	**27.3 ± 2.9, 0.11 CV**	**18.4 ± 1.9, 0.10 CV**	**7.2 ± 1.7, 0.23 CV**
142	CBb3n	223	106	15	59 (21)	14.6	20.9	32.8	9.8
176	CBb3n	273	112	32	64 (19)	13.3	19.0	30.8	10.3
5279	CBb3n	163	86	8	45 (15)	14.9	21.6	32.4	13.8
5284	CBb3n	210	110	13	69 (27)	17.2	24.7	35.9	12.9
5561	CBb3n	147	76	15	59 (18)	19.9	28.6	39.3	12.0
5598	CBb3n	226	90	16	81 (26)	19.6	26.4	43.3	17.3
6050	CBb3n	236	95	14	60 (26)	14.8	20.3	35.5	11.6
	CBb3n Class	**211 ± 43, 0.20 CV**	**96 ± 13, 0.14 CV**	**16 ± 7, 0.46 CV**	**62 ± 11, 0.18 CV**	**16.3 ± 2.6, 0.16 CV**	**23.1 ± 3.6, 0.15 CV**	**35.7 ± 4.4, 0.12 CV**	**12.5 ± 2.5, 0.20 CV**
595	CBb4	82	175	14	75 (16)	21.7	47.8	28.4	21.5
1021	CBb4	110	198	14	62 (16)	16.1	36.0	22.6	16.2
4877	CBb4	98	179	17	62 (20)	17.4	38.8	24.0	15.7
5292	CBb4	63	125	6	67 (25)	25.7	51.5	33.8	21.0
5499	CBb4	99	183	18	63 (20)	17.4	38.9	23.9	17.9

JNeurosci Accepted Manuscript

20136	CBb4	90	133	19	35 (12)	12.6	28.0	18.7	8.7
	CBb4 Class	**90 ± 16, 0.18 CV**	**166 ± 29, 0.18 CV**	**15 ± 5, 0.32 CV**	**61 ± 14, 0.22 CV**	**18.5 ± 4.6, 0.25 CV**	**40.2 ± 8.4, 0.21 CV**	**25.2 ± 5.2. 0.21 CV**	**16.8 ± 4.7, 0.28 CV**
170	CBb4w	152	98	4	48 (24)	15.9	24.0	32.0	21.5
5530	CBb4w	182	109	2	72 (31)	19.7	28.3	39.3	23.7
5601	CBb4w	179	122	3	57 (29)	15.8	24.2	31.3	24.2
5650	CBb4w	178	129	9	55 (27)	14.8	23.6	28.5	17.5
6117	CBb4w	179	125	5	50 (24)	13.9	21.8	27.8	17.6
7024	CBb4w	160	103	2	57 (15)	17.7	26.3	35.2	17.6
	CBb4w Class	**172 ± 12, 0.07 CV**	**114 ± 13, 0.11 CV**	**4 ± 3, 0.63 CV**	**56 ± 8, 0.15 CV**	**16.3 ± 2.1, 0.13 CV**	**24.7 ± 2.3, 0.09 CV**	**32.4 ± 4.3, 0.13 CV**	**20.3 ± 3.2, 0.16 CV**
485	CBb5	264	230	65	35 (12)	5.9	11.7	10.6	4.9
593	CBb5	305	211	109	23 (13)	3.5	7.0	6.7	4.4
5562	CBb5	288	206	73	39 (19)	6.4	11.9	12.3	5.8
5649	CBb5	200	184	79	30 (15)	6.1	13.0	10.2	5.3
6115	CBb5	256	203	59	35 (12)	6.3	12.0	11.8	4.6
6997	CBb5	283	244	54	34 (15)	5.5	10.7	10.2	4.3
	CBb5 Class	**266 ± 37, 0.14 CV**	**213 ± 21, 0.10 CV**	**73 ± 20, 0.27 CV**	**33 ± 6, 0.17 CV**	**5.6 ±1.1, 0.19 CV**	**11.1 ± 2.1, 0.19 CV**	**10.3 ± 2.0, 0.19 CV**	**4.9 ± 0.6, 0.12 CV**
180	CBb6	185	163	27	22 (8)	5.5	10.6	10.4	7.2
419	CBb6	239	251	34	34 (13)	6.1	12.5	10.7	7.9
6156	CBb6	220	211	32	26 (7)	5.3	10.6	9.7	6.1
9693	CBb6	149	182	33	21 (11)	5.5	12.4	8.9	5.2
16026	CBb6	228	203	45	28 (12)	5.6	10.9	10.1	7.4
	CBb6	**204 ± 37,**	**202 ± 33,**	**34 ± 7,**	**26 ± 5, 0.20**	**5.6 ± 0.3,**	**11.4 ± 0.9,**	**9.9 ± 0.7,**	**6.8 ± 1.1,**

JNeurosci Accepted Manuscript

	Class	0.18 CV	0.16 CV	0.19 CV	CV	0.05 CV	0.08 CV	0.07 CV	0.12 CV
5283[2]	CBbwf	138	149	19	26 (2)	7.8	15.9	13.4	5.0
6589[2]	CBbwf	97	126	19	20 (7)	7.6	17.1	12.1	6.0

Detailed synaptology and class designations for each of the 37 completely reconstructed (core) ON CBCs as well as the percentage contribution of gap junctions to the total synaptic contact, total input and total output of each ON CBC axonal arbor. [1]Number of confirmed gap junctions, determined either from native capture resolution or through recapture at 0.27 nm/pixel resolution with goniometric tilt. [2]Incomplete arbors. [3]Channel area is defined as the total membrane area occupied by both gap junctions and postsynaptic densities. Abbreviations: BCSs, bipolar cell conventional pre-synapses; GJs, gap junctions; LB, lower boundary; PSDs, postsynaptic densities.

JNeurosci Accepted Manuscript

Table 3. Class alignment with literature and across species.

Class	Historical[1]	Reference	Mouse Type[2]	Mouse Type (Morph.)[3]	Mouse Type (Aii output)[4]	Cat Type[5]
CBb3	nab CBnb3-4 CBb3/3-4	Famiglietti, 1981 McGillem & Dacheux, 2001 MacNeil et al., 2004	5b	5c	5b	$b_{3(a)}$
CBb3n	nab CBnb3 CBb3n	Famiglietti, 1981 McGillem & Dacheux, 2001 MacNeil et al., 2004	5a	5b	6	$b_{4(a)}$
CBb4	CBnb4 CBb4	McGillem & Dacheux, 2001 MacNeil et al., 2004	5c	5a	5c? / 9?	$b_{3(b)}$
CBb4w	CBmb4 NK1+ CBb4	McGillem & Dacheux, 2001 Casini et al., 2002 MacNeil et al., 2004	5d	5d	8	$b_{4(b)}$
CBb5	nb1, nb2 S4 CD15+ CBmb4-5	Famiglietti, 1981 Strettoi et al., 1994 Brown & Masland, 1999 McGillem & Dacheux, 2001	7	7	5a	b_2
CBb6	nb1, nb2 CaBP+ CBmb5 CBb5	Famiglietti, 1981 Massey & Mills, 1996 McGillem & Dacheux, 2001 MacNeil et al., 2004	6	8	7	b_1
CBbwf	Wb Biocytin+	Famiglietti, 1981 Jeon & Masland, 1995; MacNeil & Gaul, 2008	9	9	5d	b_5[6]
n.c.c.			8	6		

[1]Alignment to nomenclature in previous rabbit ON CBC classification schemes or descriptions of classes identified using cell-specific markers. [2]Alignment with mouse ON CBC types utilizing the unified nomenclature proposed by Tsukamoto and Omi (2017). The alignment used class descriptions from additional relevant references (Haverkamp et al., 2005; Wassle et al., 2009; Helmstaedter et al., 2013; Greene et al., 2016; Shekhar et al., 2016; Tsukamoto and Omi, 2017). [3]Alignment with mouse ON CBC types based on morphological features alone (e.g. axonal stratification, arbor breadth and diameter). [4]Alignment with mouse ON CBC types based on the differential output of Aii cells to the various ON CBC classes (Tsukamoto and Omi, 2017). Alignment with cat ON CBC types as described by Cohen and Sterling (1990). Note our proposal for the splitting of the original b_3 class into b_{3a} and b_{3b} and original b_4

JNeurosci Accepted Manuscript

1426 class into b_{4a} and b_{4b}. [6]Cohen and Sterling (1990) describe b_5 as a widefield ON CBC lacking input from

1427 overlying pedicles, but may align with the blue cone bipolar cell described by Famiglietti (1981).

1428 Abbreviations: Morph., morphology; n.c.c., no comparable class.

1429

1430

JNeurosci Accepted Manuscript

FIGURE LEGENDS

Figure 1.

Classification of rabbit ON CBCs from connectome RC1. ***A***, 3D reconstructions of representative cells for each class. All cells stratify in the ON sublamina (strata 3-5) of the IPL. A rod bipolar cell is shown for reference. Dendrites and some somas are not shown. ***B***, Horizontal views of identified ON CBCs by class. Cells within class sheets are differentially colored for clarity. Cells in "All CBb" are colored by class label according to the scheme in ***A***, and overlaid onto TEM ultrastructure at the level of the ON sublamina of the IPL. White circles approximate the volume boundaries of RC1. Scale bars: ***A***, 10 µm; ***B***, 50 µm. Abbreviations: GCL, ganglion cell layer; INL, inner nuclear layer; IPL, inner plexiform layer; RBC, rod bipolar cell.

Figure 2.

Ultrastructural identification and visualization of connectivity. ***A***, Horizontal view of a 3D rendering of the soma and axonal arbor reconstruction of cell 5598 and its 413 synaptic structures. The synaptology includes ribbons (*n* = 90, green), bipolar conventional presynapses (*n* = 16, light blue), postsynaptic densities to presynaptic conventional synapses from amacrine cells (*n* = 226, red) and gap junctions (*n* = 81, white). Synapses are rendered as volumetric shapes using circles having a diameter equal to the summed segment length of the open curve annotation for the visible structure on each section. ***A'***, Vertical view of ***A***. ***B***, ***B'***, Cell morphology rendered transparent to visualize synaptic structures from ***A***, ***A'***, respectively. ***C-G***, TEM images of representative synaptic structures from Viking at native 2.18 nm resolution. Arrows indicate direction of signaling. ***C***, Ribbon 38955 mediates signaling from cell 5598 (orange) to two postsynaptic cells (yellow, blue) in a classic dyad arrangement. ***D***, Bipolar cell conventional presynapse 91577 exhibits all the features of a traditional ribbon synapse, including vesicles present at the plasma membrane, but lacks the ribbon structure. ***E***, Postsynaptic density 114606 to an AC (yellow) conventional presynapse. ***F***, Gap junction 56921 mediates coupling with an ON CBC (pink). ***F'***, Enlarged view of ***F***. Gap junction located between arrows. ***G***, Adherens junction 124245 formed with a cell of unknown identity (yellow). ***G'***, Enlarged view of ***G***. Adherens junction boundaries indicated by arrowheads. ***H***, Gap junction 56921 from ***F*** reimaged at 40,000X magnification (resolution = 0.27 nm/pixel) with goniometric tilt (10°). Gap junction boundaries indicated by arrows and adjacent adherens junction boundaries by arrowheads. ***H'***, Enlarged view of gap junction from ***H*** with an overlay of the corresponding density plot obtained from the region between the dashed lines. Peaks (1,3,5) and valleys (2,4) in the density plot that generate the characteristic pentalaminar profile are labeled. ***H"***, Enlarged view of

JNeurosci Accepted Manuscript

adjacent adherens junction from ***H*** at 15° tilt. Corresponding density plot obtained from the region between the dashed lines and overlaid. Note the prominent extracellular space (asterisk) between the membrane peaks. Scale bars: ***A***, 10 µm; ***C-G,F',G'***, 250 nm; ***H-H"***, 50 nm. Abbreviations: a, adherens junction; bc, bipolar conventional synapse; c, conventional pre-synapse; g, gap junction; p, post-synaptic density; r, ribbon. Image max-min contrast stretched (***E,F',G'***).

Figure 3.

Graphical summaries of ON CBC coupling. ***A***, Proportion of homocellular versus heterocellular gap junctions by class based on frequency counts. ***B***, Coupling profiles of ON CBC classes. The matrix reports the mean number of gap junctions formed by a given ON CBC class (row) with each partner class (column), as assessed from the core set of 37 ON CBCs in RC1 detailed in this paper. The matrix is therefore asymmetrical, as classes differ in arbor diameter, coverage factors, etc. Values are encoded by the linear heat map scale below. Asterisks indicate class pairings where coupling has not been confirmed. The profile for the CBbwf class is preliminary due to the incompleteness of available arbors. Detailed coupling profiles for individual cells and class statistics are provided in Figure 3-1.

Figure 4.

Heterocellular coupling topologies. ***A-D***, Canonical heterocellular coupling between ON CBCs and Aii cells. ***A***, Contact sites between CBb3n 5279 (orange) and Aii 514 (light blue), including two canonical heterocellular gap junctions (dark blue; arrowheads). ***B***, Vertical view of the region between the dotted lines in ***A***. ***C***, Gap junction 6171 (arrowhead 'C' in ***B***) between CBb3n 5279 axonal terminal (orange) and Aii 514 arboreal dendrite (light blue). ***C'***, Enlarged view of boxed region in ***C***. ***D***, TEM showing membrane contact (arrow 'D' in ***B***) between the descending axon of CBb3n 5279 and lobule of Aii 514. The Aii lobule forms a conventional presynapse (between arrowheads) onto a passing OFF CBC (Cba) process. ***D'***, Enlarged view of boxed region in ***D***. ***E-J***, CBb3 rejects canonical heterocellular coupling with Aii cells, but couples with the Aii-coupled CBb3n class. ***E,F***, CBb3 5641 (maroon) exhibits territory overlap (***E***) and costratification (***F***) below the lobular dendrites of Aii 7113 (light blue) and fully costratifies with CBb3n 5598 (orange). Horizontal dotted line in ***F*** delineates the ON/OFF boundary of the IPL. ***F'***, Enlarged view of the boxed region in ***F*** (arrow in ***E***). ***G***, Single TEM image showing bipolar conventional synapse 124055 from CBb3 5641 onto Aii 7113, cross-class homocellular gap junction 114999 between CBb3 5641 and CBb3n 5598, and canonical heterocellular gap junction 115004 between CBb3n 5598 and Aii 7113. ***H,I***, Reimaging of boxed regions in

JNeurosci Accepted Manuscript

G at 0.27 nm/px resolution with goniometric tilt. ***J,J'***, Enlarged view of boxed region in ***G*** on section 245 (***J***) and adjacent section 244 (***J'***). ***K-Q***, Noncanonical coupling between ON CBCs and xACs. ***K***, Two of five noncanonical gap junctions (mint; arrow and arrowhead in ***K'***) between CBb4 595 (lime) and xAC 7576 (teal) are visible. ***K'***, Enlarged view of boxed region in ***K***. ***L***, TEM image of gap junction 54868 (arrow in ***K'***). ***L'***, Reimaging of boxed region in ***E*** at 0.27 nm/pixel resolution with goniometric tilt. ***M***, Noncanonical heterocellular gap junctions (mint, arrows in ***M',M"***) between xAC 7231 (teal) and two CBb5 cells, 5536 (cyan) and 15977 (powder blue). ***M',M"***, Enlarged views of the boxed regions in ***M***. ***N***, TEM image of gap junction 116945 (arrow in ***M'***) between a branch of CBb5 5536 in the OFF sublamina and small extension off the soma of xAC 7231. ***N'***, Reimaging of boxed region in ***N*** at 0.27 nm resolution with goniometric tilt. ***O***, TEM image of gap junction 116987 (arrow in ***M"***) between CBb5 15977 and xAC 7231 in the ON sublamina. ***O'***, Enlarged view of boxed region in ***O***. Gap junctions scaled by a factor of 2 (***A,B***) or 4 (***K,K',M,M',M"***) for visualization. Scale bars: ***A,E,F,K,M***, 10 µm; ***B***, 5 µm ; ***D,G,L***, 1 µm; ***C,D',N,O***, 500 nm; ***C',H,I,J,J',L',N',O'***, 100 nm. Abbreviations: bcs, bipolar conventional presynapse; cs, conventional presynapse; gj, gap junction; psd, postsynaptic density.

Figure 5.

In-class homocellular coupling topologies. ***A-I***, CBb5 in-class coupling. ***A***, Horizontal view showing the locations of eight in-class gap junctions (yellow) between cell 593 (cyan) and its immediate CBb5 neighbors, cells 166 (forest green), 6115 (powder blue), 5649 (teal), 5562 (powder blue), and 6997 (forest green). One gap junction (72657, white circle) remains inconclusive even at maximum tilt (± 65°). ***B-I***, TEM images for regions indicated in ***A*** (white boxes). CBb5 593 forms gap junctions 60046 (***E***) and 60010 (***F***) with cell 166, 55890 (***G***) with cell 6115, 53818 (***H***) with cell 5649, 49434 (***I***) and 79658 (***J***) with cell 5562, and 52441 (***K***) and 59747 (***L***) with cell 6997. ***B'-I'***, Reimaging of boxed regions in ***B-I*** at 0.27 nm/pixel resolution with goniometric tilt. Brackets notate gap junction boundaries based on tilt series. ***J-K***, In-class coupling between neighboring CBb3n cells. ***J***, Five in-class gap junctions (yellow; arrow and arrowheads) between CBb3n cells 5284 (brown) and 6050 (tan). ***J'***, Enlarged and rotated view of circled region in ***J***. Arrowheads in ***J'*** indicate different gap junctions than in ***J***. ***K***, TEM image of gap junction 57071 (arrow in ***J'***). ***K'***, Reimaging of boxed region in ***K*** at 0.27 nm/pixel resolution with goniometric tilt confirms gap junction identity. ***L-O***, Aii coupling bridging CBb3n in-class coupling. ***L***, Some branches of neighboring CBb3n cells 6118 (tan) and 6120 (orange) terminate in tip-to-tip topology with in-class gap junctions (yellow, arrowheads), while others terminate without contact, forming gap junctions with Aii cells (dark blue) at their tips instead (asterisks). Cross-class (magenta) and heterocellular xACs (mint) gap junctions also shown. Rare case of tiling violation (open arrowhead). ***L'***, Rotated

JNeurosci Accepted Manuscript

view of the circled area in ***L*** rendered with coupling partner Aii 7904 (light blue). ***M***, TEM image showing gap junction 111592 (***N***) between CBb3n 6120 and Aii 7904 directly opposite gap junction 119474 (***O***) between Aii 7904 and CBb3n 6118. ***N***, Reimaging of boxed region in ***M*** at 0.27 nm resolution with goniometric tilt. ***O***, Zoomed view of boxed region in ***M***. ***P-Q***, CBb3 in-class coupling. ***P***, Two in-class gap junctions (yellow) formed at a single contact site between neighboring CBb3 cells 909 (maroon) and 5297 (peach). ***P'***, Enlarged and rotated view of encircled region in ***P***. ***Q***, TEM image of gap junction 121062 (arrow in ***P'***). ***Q'***, Reimaging of boxed region in ***Q*** at 0.27 nm/pixel resolution with goniometric tilt. Gap junctions scaled by a factor of 6 (***A***), 4 (***J,P,P'***), or 2 (***J',L,L'***) for visibility. Scale bars: ***A,J,L,P***, 10 µm; ***L'***, 5 µm; ***Q***, 1 µm; ***B-I,K,M***, 500 nm; ***B'-I',K',N,O,Q'***, 100 nm. Abbreviations: gj, gap junction.

Figure 6.

ON CBC classes lacking in-class homocellular coupling. ***A-E***, Rejection of in-class coupling by the CBb6 class. ***A***, Presence of an adherens junction (tan) at site of contact between neighboring CBb6 cells 400 (magenta) and 9693 (purple). ***A'***, Enlarged view of the boxed area in ***A*** rendered with the processes of Aii cells 2610 (slate) and 304 (blue) and relevant gap junctions (arrowheads; canonical heterocellular in blue and homocellular Aii in white). ***B-E***, TEM images of select serial sections. ***B***, Section 240: Heterocellular gap junction 18732 between CBb6 9693 (purple) and Aii 2610 (slate). ***C***, Section 242: Adherens junction 59565 between CBb6 9693 (purple) and CBb6 400 (pink) (arrow in ***A'***). ***D***, Section 244: Heterocellular gap junction 59564 between CBb6 9693 (purple) and Aii 304 (blue). ***E***, Section 254: Heterocellular gap junction 130578 between CBb6 400 (pink) and Aii 304 (blue). Homocellular gap junction also present between Aii 2610 (slate) and Aii 304 (blue) (bracket in ***E***). ***B',D',E'***, Reimaging of boxed regions in ***B,D,E*** at 0.27 nm/pixel resolution with goniometric tilt. Brackets notate structure boundaries. ***C'***, "Zoomed" view of boxed region in ***C***. ***F-H***, Absence of in-class coupling between CBbwf cells. ***F***, Adherens junction (tan, arrow) present at the only contact site between CBbwf cells 5283 (slate) and 6589 (gold). Inset shows enlarged and rotated view of the site of interaction. ***G,H***, TEM images from serial sections 267 and 268 showing membrane contact between the branches of CBbwf 6589 (gold) and CBbwf 5283 (slate) at the site indicated by the arrow in ***F***. A density is present in both sections. ***G',H'***, Reimaging of boxed regions in ***G,H*** at 0.27 nm/pixel resolution with goniometric tilt reveals adherens junction 123847 and no evidence of an adjacent gap junction. Scale bars: ***F***, 20 µm; ***A***, 10 µm; ***B-E***, 1 µm; ***G,H***, 500 nm; ***B'-E',G',H'***, 100 nm. Abbreviations: a, adherens junction; gj, gap junction; sec, section.

Figure 7.

JNeurosci Accepted Manuscript

Cross-class homocellular coupling topologies of CBb3/3n/4/4w. ***A***, Extensive costratification of ON CBC axonal arborizations. ***B-C***, Extensive CBb3n coupling with CBb3. ***B***, Twelve of the 22 cross-class gap junctions (magenta; arrow and arrowheads in ***B,B'***) between CBb3n 176 (orange) and CBb3 5531 (maroon) are visible. ***B'***, Enlarged view of boxed region in ***B***. ***C***, TEM image of gap junction 54567 (arrow in ***B'***). ***C'***, Reimaging of boxed region in ***C*** at 0.27 nm/pixel resolution with goniometric tilt. ***D-E***, Frequent CBb4w coupling with CBb4. ***D***, Six of the ten cross-class gap junctions (magenta; arrow, arrowheads in ***D,D'***) between CBb4w 6117 (green) and CBb4 5292 (lime) are visible. ***D'***, Enlarged view of boxed region in ***D***. ***E***, TEM image showing gap junction 51346 (arrow in ***D'***). ***E'***, Reimaging of boxed region in ***E*** at 0.27 nm/pixel resolution with goniometric tilt. ***F-G***, Frequent CBb3n coupling with CBb4. ***F***, Two of three cross-class gap junctions (magenta; arrow, arrowheads in ***F,F'***) between CBb4 595 (lime) and CBb3n 176 (orange) are visible. ***F'***, Enlarged view of boxed region in ***F***. ***G***, TEM image showing gap junction 46663 (arrow in ***F'***). ***G'***, Reimaging of boxed region in ***G*** at 0.27 nm/pixel resolution with goniometric tilt. ***H-I***, CBb4w coupling with CBb3n. ***H***, One of two cross-class gap junctions (magenta, arrow in ***H'***) between CBb4w 6117 (green) and CBb3n 176 (orange). ***H'***, Enlarged view of boxed region in ***H***. ***I***, TEM image showing gap junction 58716 (arrow in ***H'***). ***I'***, Reimaging of boxed region in ***I*** at 0.27 nm/pixel resolution with goniometric tilt. ***J-K***, Sparse CBb4 coupling with CBb3. ***J***, Single cross-class gap junction (magenta, arrow in ***J'***) between CBb4 595 (lime) and CBb3 5531 (maroon). ***J'***, Enlarged view of boxed region in ***J***. ***K***, TEM image showing gap junction 91490 (arrow in ***J'***). ***K'***, Reimaging of boxed region in ***K*** at 0.27 nm/pixel resolution with goniometric tilt. ***L-M***, Rejection of coupling between CBb3 and CBb4w. ***L***, Costratification of CBb4w 5530 (green) and CBb3 5531 (maroon) axonal arbors. ***L'***, enlarged view of boxed region showing position of adherens junction 81621 (tan; arrow). ***M***, TEM image showing a strong density at the location of contact indicated by the arrow in ***L'***. ***M'***, Reimaging of boxed region in ***M*** at 0.27 nm/pixel resolution with goniometric tilt reveals an adherens junction with strong asymmetric densities, but no gap junction. Gap junctions scaled by a factor of 4 (***B,B',D,D',F,F',H,H',J,J'***) for visualization. Most cells form additional gap junctions within these specific motifs, but with additional cells (Figure 3-1). Scale bars: ***A,B,D,F,H,J,L***, 10 µm; ***C,E,G,I,K,M***, 1 µm; ***C',E',G',I',K',M'***, 100 nm . Abbreviations: a, adherens junction; gj, gap junction; RBC, rod bipolar cell.

Figure 8.

Cross-class homocellular coupling topologies of CBb5/6/wf. ***A-B***, Rare CBb5 coupling with CBb6. ***A***, Single cross-class gap junction (magenta; arrow in inset) between CBb6 5515 (purple) and CBb5 5623 (cyan). Inset, enlarged view of boxed region. ***B***, TEM image of gap junction 119263 (arrow in ***A***). ***B'***, Reimaging of boxed region in ***B*** at 0.27 nm/pixel resolution with goniometric tilt. ***C-D***, Rejection of coupling between CBb6 and CBbwf. ***C***, Costratification and

JNeurosci Accepted Manuscript

overlapping arbors affords two sites of membrane contact, but only a single adherens junction (tan; arrow in inset) between the axonal arbors of CBb6 180 (purple) and CBbwf 5283 (gray) and no gap junctions. Inset, enlarged view of boxed region. ***D***, TEM image of adherens junction 66309 (arrow in ***C***). ***D'***, Reimaging of boxed region in ***D*** at 0.27 nm/pixel resolution with goniometric tilt. ***E-F***, Rare CBb5 coupling with CBbwf. ***E***, Single cross-class gap junction (magenta; arrow in inset) between CBb5 6997 (cyan) and CBbwf 6589 (gray). Inset, enlarged view of boxed region. ***F***, TEM image of gap junction 130564 (arrow in ***E***). ***F'***, Reimaging of boxed region in ***F*** at 0.27 nm/pixel resolution with goniometric tilt. ***G-H***, Rare CBb5 coupling with CBb3n. ***G***, Single cross-class gap junction (magenta; arrow in inset) between CBb5 5649 (cyan) and CBb3n 6120 (orange). Inset, enlarged view of boxed region. ***H***, TEM image of gap junction 111023 (arrow in ***G***). ***H'***, Reimaging of boxed region in ***H*** at 0.27 nm/pixel resolution with goniometric tilt. ***I-J***, Rejection of coupling between CBb5 and CBb3n. ***I***, Presence of an adherens junction (tan; arrow in inset) between CBb5 483 (cyan) and CBb3n 1724 (orange), but no gap junctions. Inset, enlarged view of boxed region. ***J***, TEM image of adherens junction 101900 (arrow in ***I***). ***J'***, Reimaging of boxed region in ***J*** at 0.27 nm/pixel resolution with goniometric tilt. ***K-L***, Rare CBb6 coupling with CBb3n. ***K***, Single cross-class gap junction (magenta; arrow in ***K'***) between CBb3n 5284 (orange) and CBb6 16026 (purple). ***K'***, Enlarged view of boxed region in ***K***. Gap junction scaled by a factor of 4 for visualization. ***L***, TEM image of gap junction 113383 (arrow in ***K'***). ***L'***, Reimaging of boxed region in ***L*** at 0.27 nm/pixel resolution with goniometric tilt. Scale bars: ***A,C,E,G,I***, 10 µm; ***K***, 20 µm; ***B,D,H,J***, 1 µm; ***F,L***, 500 nm ***B',D',F',H',J',L'***, 100 nm. Abbreviations: a, adherens junction; gj, gap junction.

Figure 9.

Geometry accounts for the variation in, but not specificity of, ON CBC coupling. ***A***, Calculating the 2D (XY) intersection of the convex hulls for each CBb4 cell with that of each member of the CBb3 class. *Left,* Convex hulls of CBb4 cells. *Right,* Convex hulls of CBb3 cells. *Middle*, the portion of each CBb4 cell's convex hull that intersects in XY with the convex hull of a CBb3 cell. ***B***, Comparisons of coupling frequency as a function of the degree of axonal field intersection between cell pairings (computed in ***A***) for each class. Each point represents a single calculated area of intersection between two cells, regardless of the presence/absence of coupling. Thus, many points have an intersection area > 0, but no gap junctions. Since each point represents a single cell-cell pairing (e.g. CBb4 4877 with CBb4w 5601), every cell contributes multiple points due to multiple pairings. Note the different X-axis scaling used for the CBb3 and CBb3n graphs. Data was fitted to a linear model with y-intercept of zero and the adjusted R^2 values reported adjacent to each model. Significance (*p*) values from the *post-hoc* Scheffe test are presented in the

JNeurosci Accepted Manuscript

corresponding matrix for each class' graph with the difference (D) statistic in parentheses below. Significance (p < 0.05) is highlighted in yellow. *** denotes instances where the R software environment computed $p < 2.2E^{-16}$.

Figure 10.

Size distribution of gap junction plaques. ***A***, Histograms comparing the frequency distributions of gap junction plaque size (area) by coupling mode for each ON CBC class. Median values are indicated by vertical dashed lines. Note the change in Y-axis scaling for the CBb5, CBb6, and CBbwf class graphs. Adjusted significance (p) values (corrected for multiple comparisons) from the Wilcoxon rank-sum tests with continuity correction are presented in the corresponding matrix for each class' graph with the test statistic (W) in parentheses below; n (in-class, cross-class, xAC, Aii) = CBb3 (13, 183, 42, 0), CBb3n (32, 279, 11, 106), CBb4 (30, 297, 28, 7), CBb4w (68, 188, 0, 60), CBb5 (63, 8, 29, 79), CBb6 (5, 9, 0, 116), CBbwf (0, 9, 0, 36). Significance (p < 0.05) is highlighted with yellow shading. *** denotes instances where the R software environment computed $p < 2.2E^{-16}$. ***B***, Proportion of gap junctions with different partners based on numerical frequency or cumulative area. Values reported as the mean ± 1SD. Abbreviations: cross, cross-class; in, in-class.

Figure 11.

Spatial distribution of gap junctions across ON CBC axonal arbors. ***A***, Spatial distribution of gap junctions across a representative ON CBC arbor, color coded by coupling mode: heterocellular with Aii (dark blue) or xACs (mint, none), homocellular *in-class* (yellow), *self* (orange), or *cross-class* (magenta). All gap junctions scaled by a factor of 4 for visualization. ***B***, Histograms comparing the frequency distributions of gap junction distance by coupling mode for each ON CBC class. Distance is calculated in the XY plane from the geometric center of the parent cell's convex hull. The distribution of distances for the vertices forming the convex hull (CHV) for the parent cells is included for comparison as an approximation of the arbor boundaries. Median values are indicated by vertical dashed lines. Note the change in Y-axis scaling for the CBb5 and CBb6 class graphs. The CBbwf class is not shown due to the incompleteness of the representative cells' arbors. Adjusted significance (p) values from the Wilcoxon rank-sum tests with continuity correction are presented in the corresponding matrix for each class' graph with the test statistic (W) in parentheses below; n (in-class, self, cross-class, xAC, CHV, Aii) = CBb3 (10, 6, 183, 42, 50, 0), CBb3n (34, 5, 279, 11, 66, 106), CBb4 (4, 27, 297, 28, 49, 7), CBb4w (62, 27, 188, 0, 59, 60), CBb5 (68, 10, 8, 29, 62, 75), CBb6 (2, 4, 9, 0, 46, 116). Significance (p < 0.05) is highlighted with yellow shading. *** denotes instances where the R software

JNeurosci Accepted Manuscript

environment computed $p < 2.2E^{-16}$. ***C***, Model illustrating the spatial distribution of gap junctions according to coupling mode across a generalized ON CBC arbor. Abbreviations: CHV, convex hull vertices; cross, cross-class; in, in-class.

Figure 12.

Glycine accumulation in ON CBCs. ***A***, TEM image from Viking of section 30 of the RC1 volume displaying the somas of seven ON CBCs (circles) and one Aii (pentagon). ***A'***, Section 30 glycine channel showing intermediate glycine signals in the somas of all ON CBCs (circles) and the Aii (pentagon), including members of the CBb3 and CBb4 classes (asterisks). ***B***, Plot quantifying the glycine signals recorded for the somas of ON CBCs. Glycine signals are reported as the average mean pixel value (0-255) ± 1SD; $n = 17$ (CBa, CBb5), 20 (CBb3), 34 (CBb3n), 11 (CBb4), 10 CBb4w), 6 (CBb6), 1 (CBbwf), 105 (all CBb). Asterisks denotes significance ($t(38) = 19.08$, $p < 2E^{-16}$, Welsh two sample t-test, 2-tailed). Scale bars: ***A***, 20 µm. Abbreviations: TEM, transmission electron microscopy.

Figure 13.

Differential distribution of Aii output to ON CBCs. ***A***, Coupling profile of the Aii cell class. Each column reports the mean number of gap junctions formed by an Aii cell with ON CBC classes and other Aii cells, as assessed from four Aii cells in RC1. Values are encoded by the linear heat map scale below. Asterisk indicates a pairing where coupling has not been confirmed. Note that this is not the reciprocal of the Aii column presented in Figure 3, as the frequencies here are calculated per Aii cell, whereas Figure 3 calculates Aii coupling frequencies per ON CBC. Detailed coupling profiles for individual Aii cells and extended class statistics are provided in Figure 3-1. ***B***, Partner class-dependent sizing rules for Aii cell gap junction plaques. Histogram comparing the frequency distributions of gap junction plaque size (area) by partner ON CBC class. Median values are indicated by vertical dashed lines. Adjusted significance (p) values from the Wilcoxon rank-sum tests with continuity correction are presented in the corresponding matrix with the test statistic (W) in parentheses below; $n = 184$ Aii, 66 CBb3n, 13 CBb4w, 39 CBb5, 73 CBb6, 17 CBbwf. Significance ($p < 0.05$) is highlighted with yellow shading. ***C***, The proportion of gap junctions with different partners based on numerical frequency or cumulative area. Values reported as the mean ± 1SD.

Figure 14.

JNeurosci Accepted Manuscript

ON CBC coupling motifs within retinal networks. ***A***, Models of the scotopic and photopic networks of the light-adapted rabbit retina involving ON CBCs. Arrows indicate chemical synapses (ribbon) while plain lines indicate gap junctions. In the primary rod pathway, rod photoreceptor signals are unevenly distributed through canonical heterocellular gap junctions to the seven classes of ON CBCs. Multipoint coupling mediated by in-class homocellular gap junctions among neighboring cells of the same class (not shown) produces sheets of coupled cells (albeit to differing degrees). Cross-class homocellular coupling potentially allows lateral spread of signals across parallel ON CBC channels. CBb6 and CBbwf classes contact Aii cells with both electrical (plain lines) and chemical (arrows) synapses. These ON CBCs then transfer these processed rod signals to ON and ON-OFF GCs. In the photopic network, M/L cone signals are collected by six classes of ON CBCs while S cone signals are collected by the CBbwf class. Mixing of these parallel ON CBC channels may occur directly through cross-class homocellular coupling or indirectly through the Aii cell, despite rectification of these canonical heterocellular gap junctions. ON CBCs then transfer the processed signals on to ON and ON-OFF GCs. ***B***, Potential mixing of parallel ON CBC channel input to GCs via gap junctional coupling (::). Connectivity matrices generated by Graffinity for paths of different lengths (hops) between ON CBCs and GCs. Note that the data include all cells and synapses currently annotated in connectome RC1, including incompletely annotated cells. The CBb label contains all partial cells or fragments that could not be classified beyond the ON superclass. Empty tiles indicate instances of zero identified paths. The path count is encoded using the linear color scale below. Abbreviations: ::, coupling; RBC, rod bipolar cell; tON DS GC, transient ON directionally selective GC.

JNeurosci Accepted Manuscript

EXTENDED DATA LEGENDS

Figure 3-1.

Detailed individual cell coupling profiles and class statistics for the core set of 37 ON CBC and four Aii cells. [1]The CBb label contains all partial cells or fragments that could not be classified beyond the ON superclass. The number of coupled cells and number of gap junctions per cell were not quantified. [2]Most partner xACs exist as fragments, only sufficiently traced and annotated to confirm they were not Aii cells. Thus, the number of coupled cells and number of gap junctions per cell were not quantified. [3]Two Aii cell partners could not be traced far enough to determine whether they were of amacrine or bipolar cell identity.

JNeurosci Accepted Manuscript

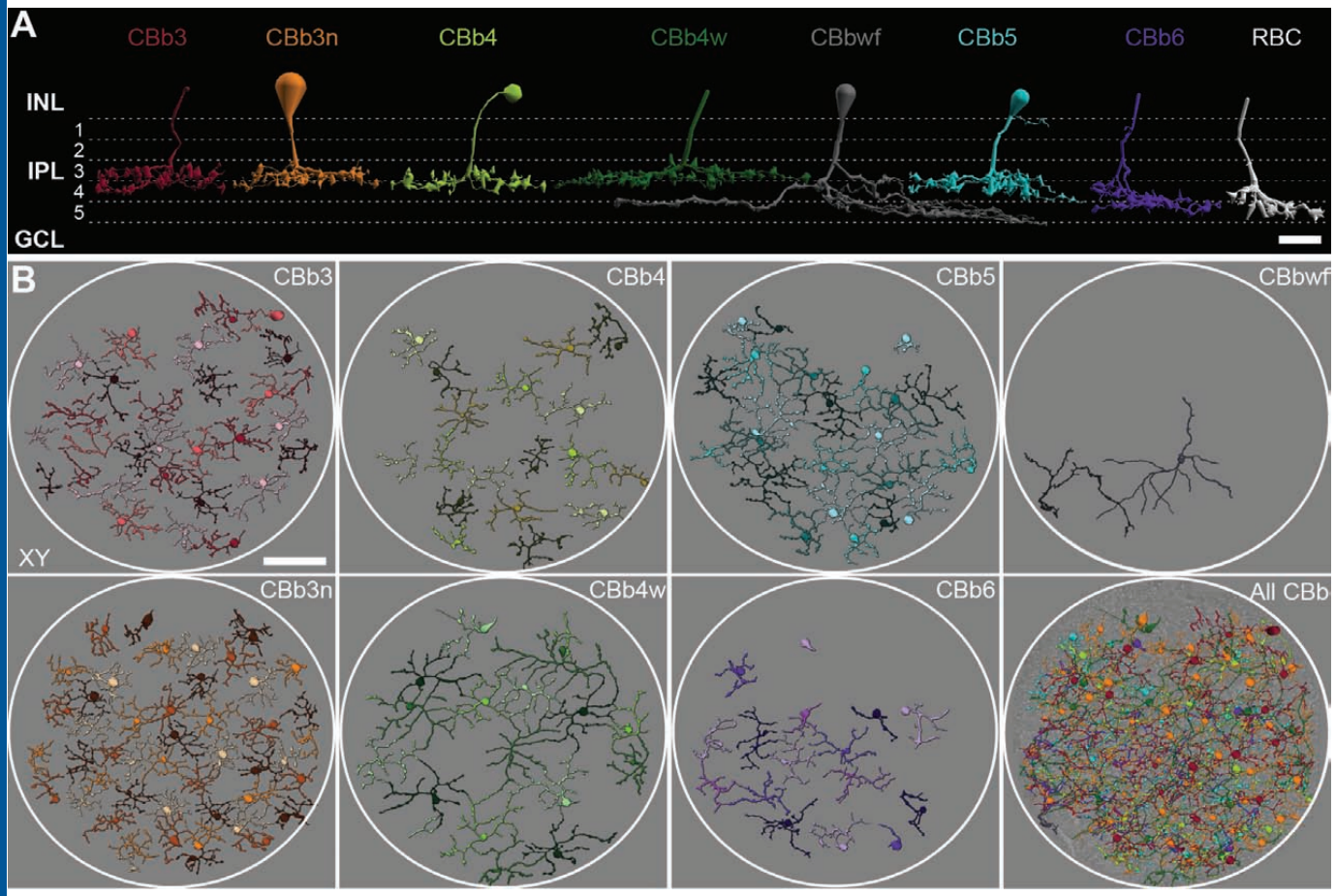

JNeurosci Accepted Manuscript

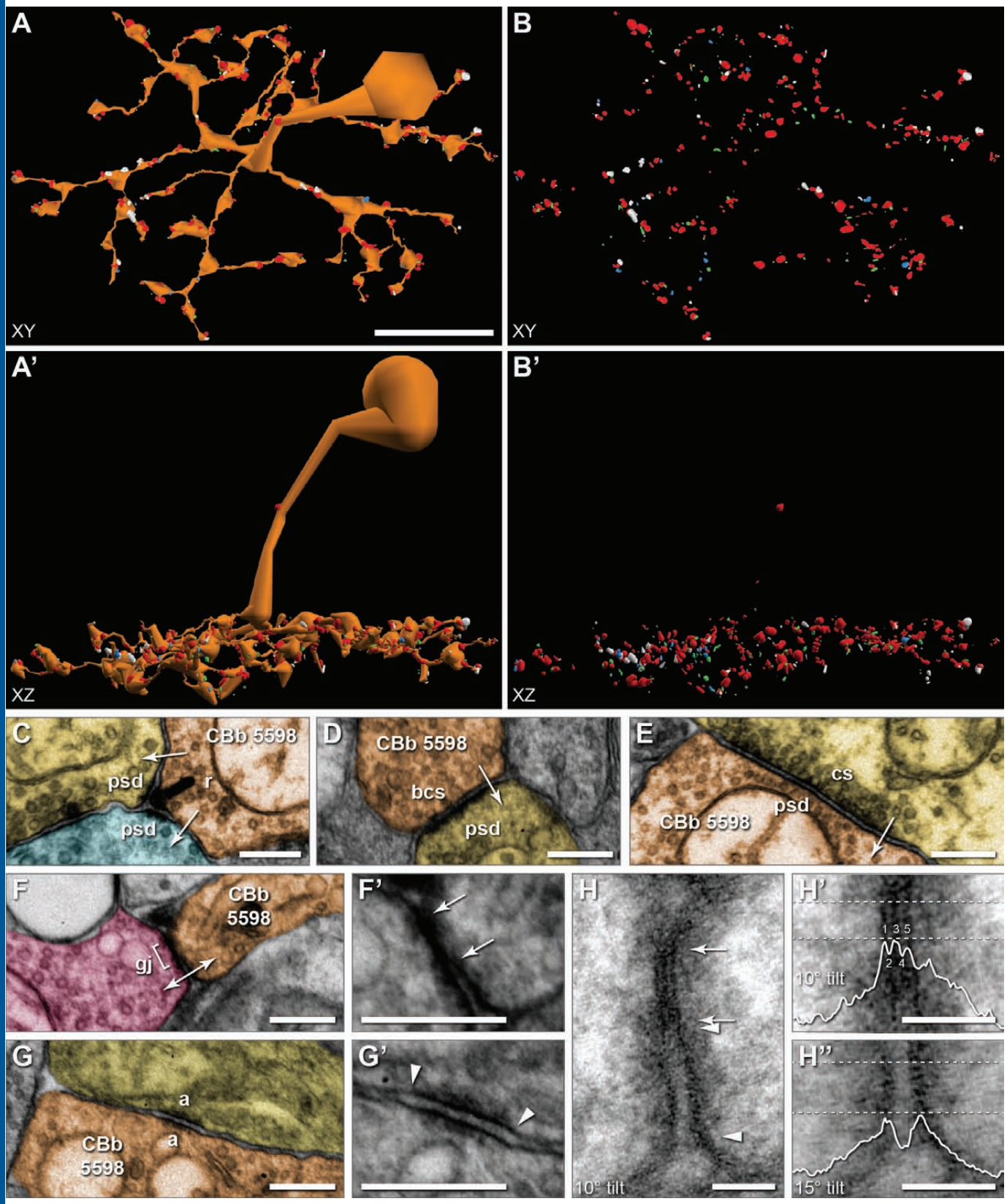

JNeurosci Accepted Manuscript

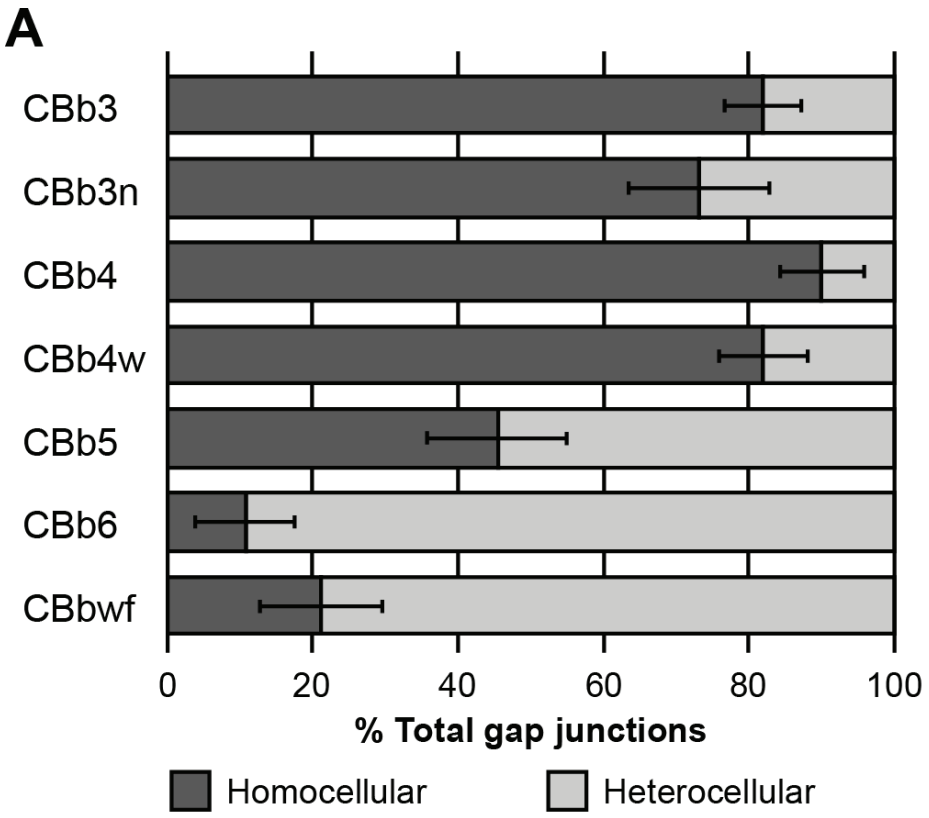

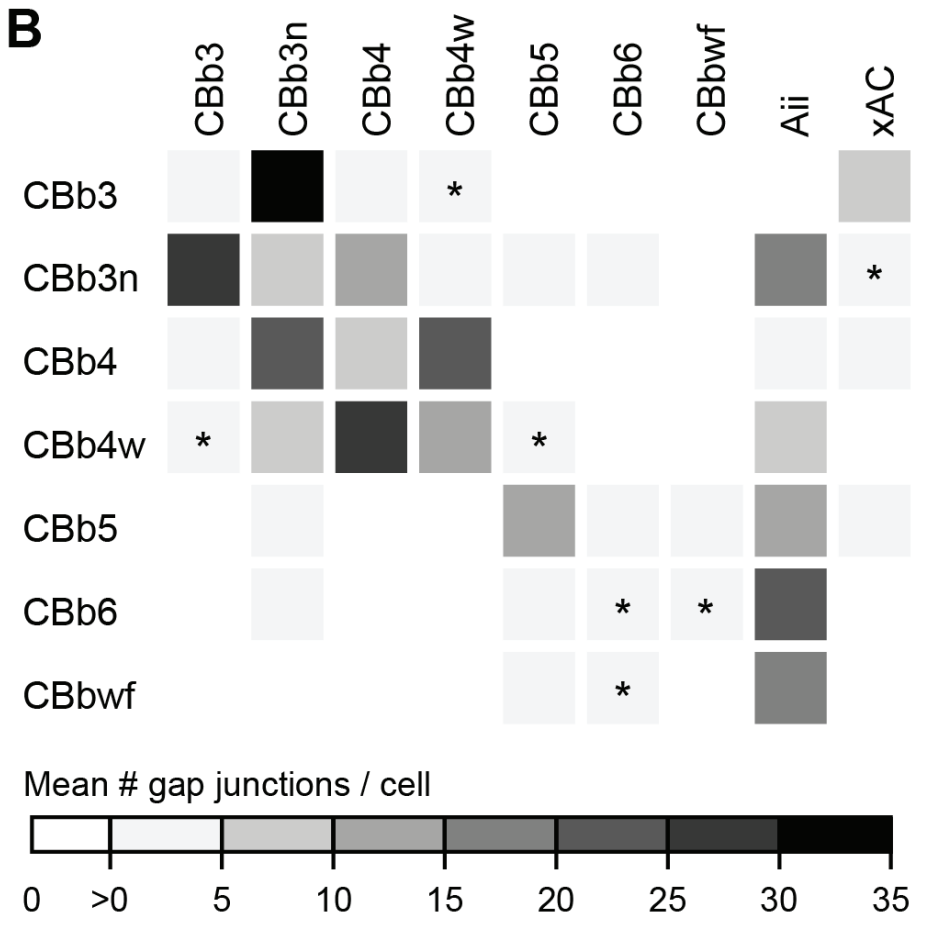

JNeurosci Accepted Manuscript

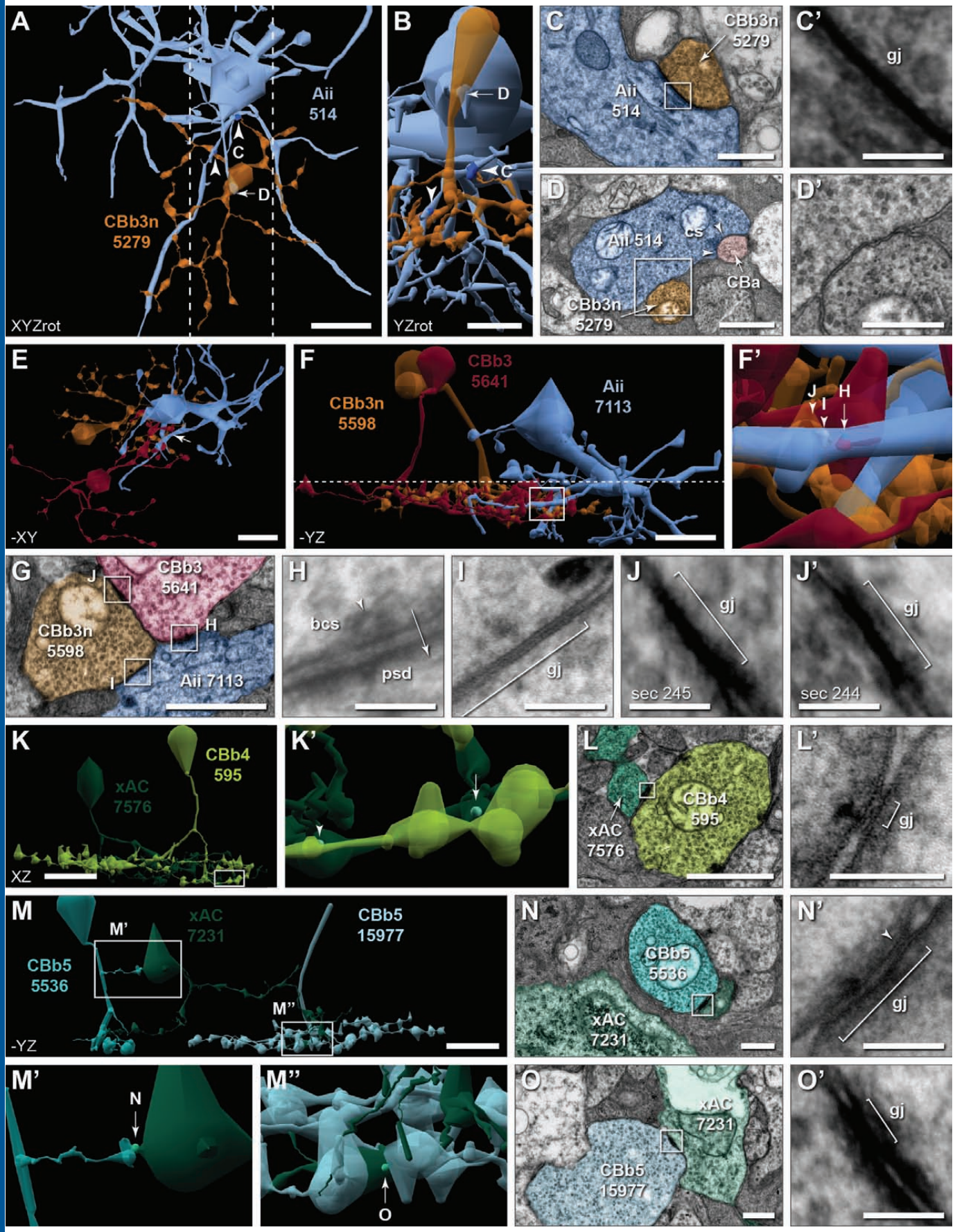

JNeurosci Accepted Manuscript

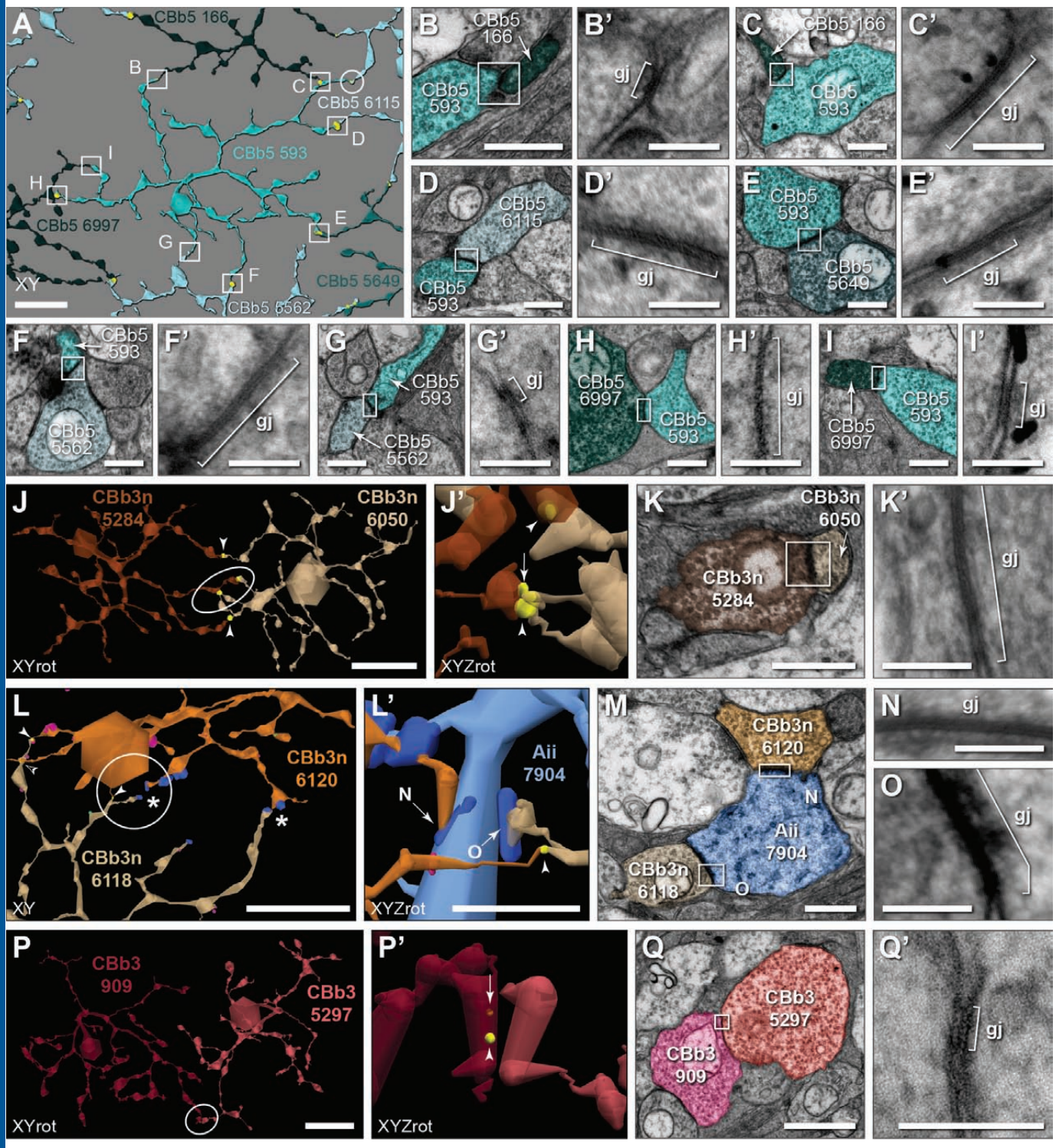

JNeurosci Accepted Manuscript

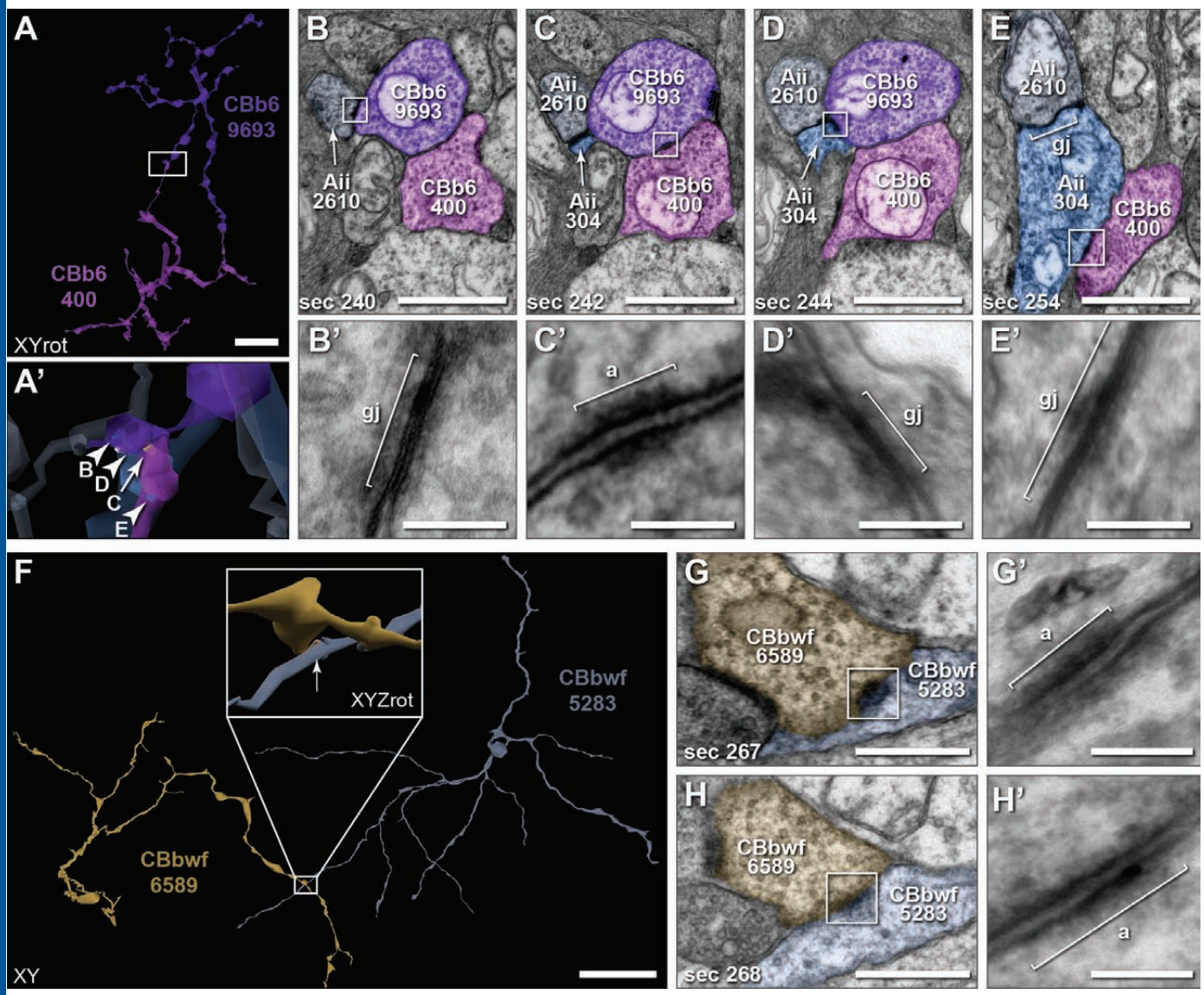

JNeurosci Accepted Manuscript

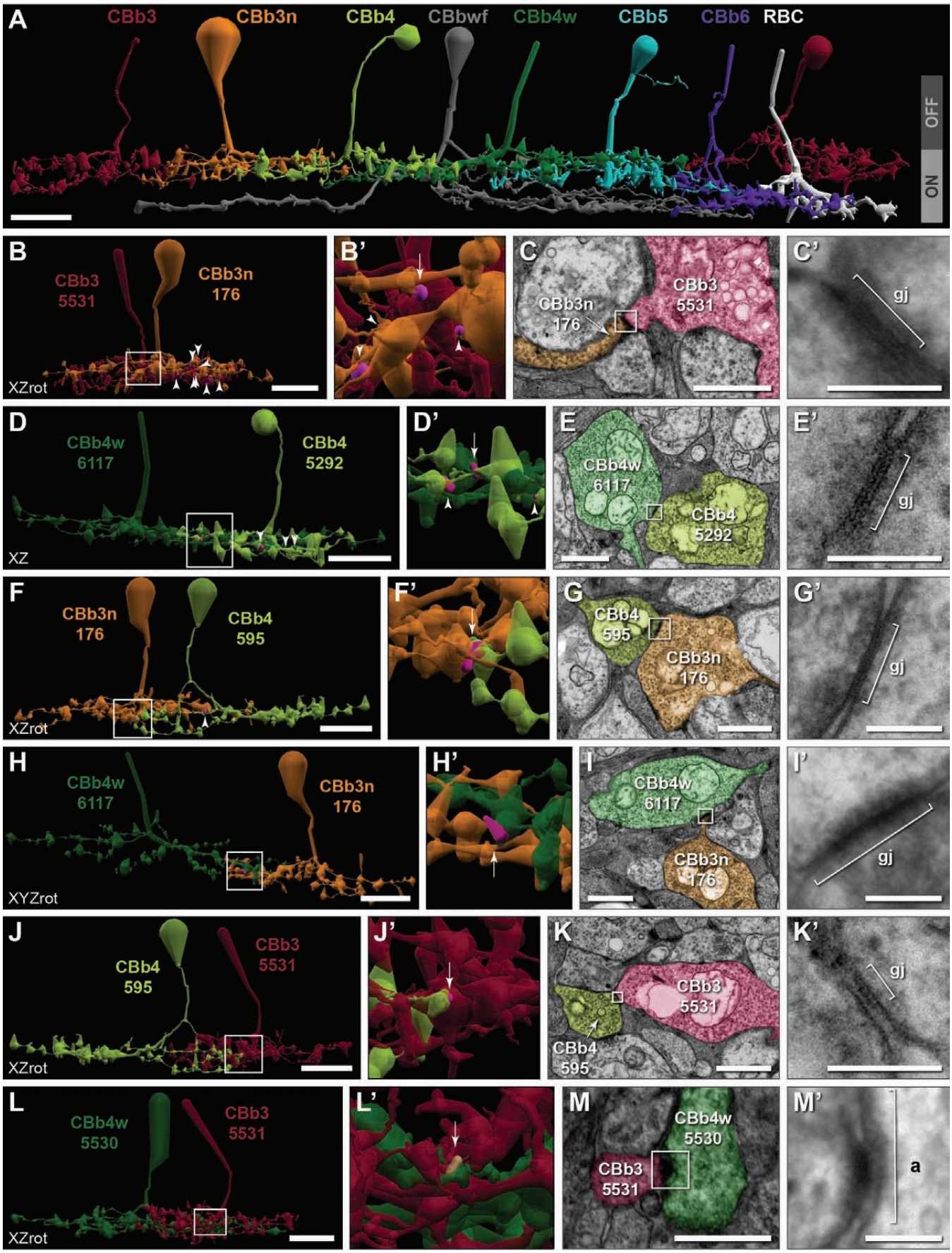

JNeurosci Accepted Manuscript

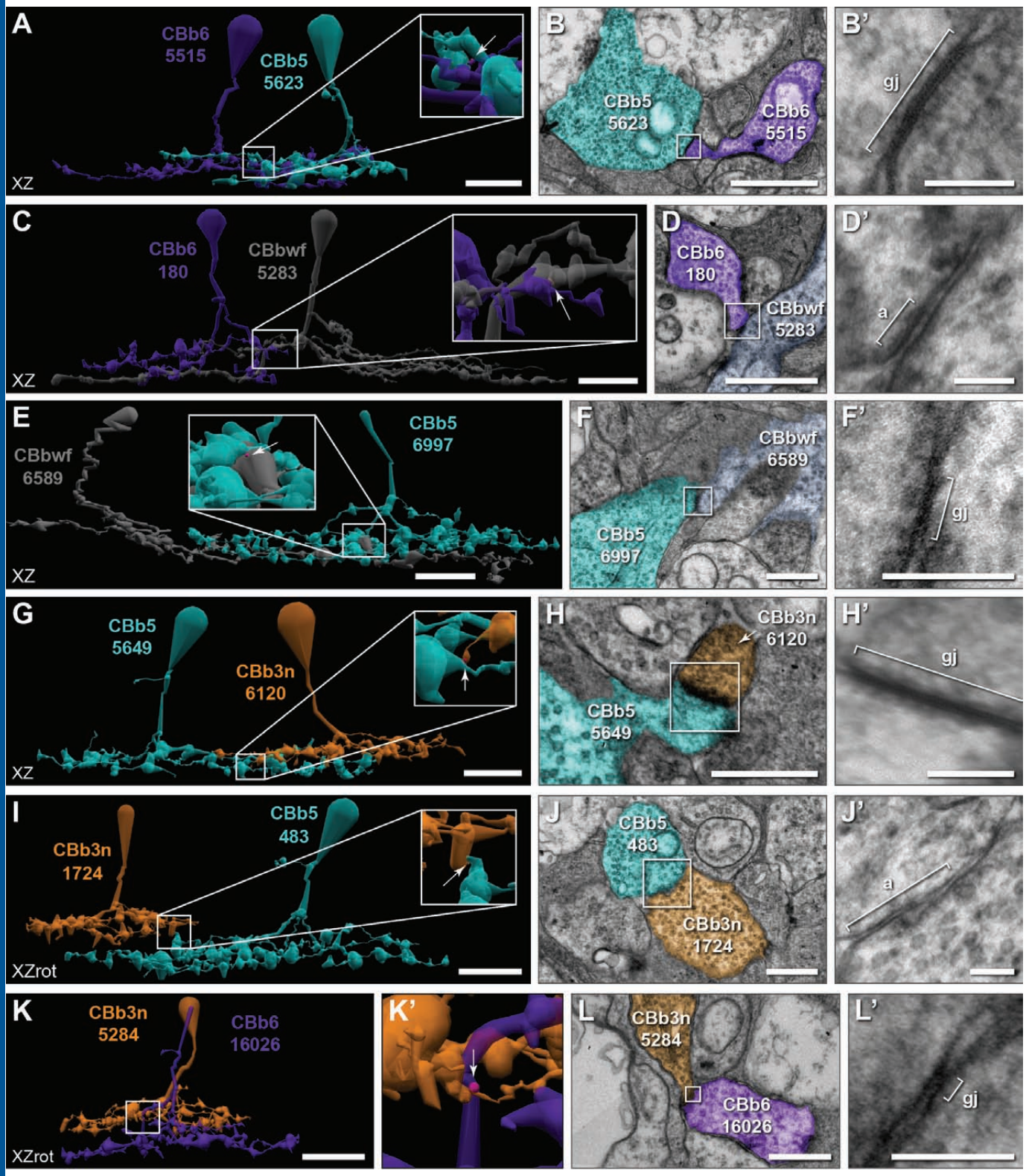

JNeurosci Accepted Manuscript

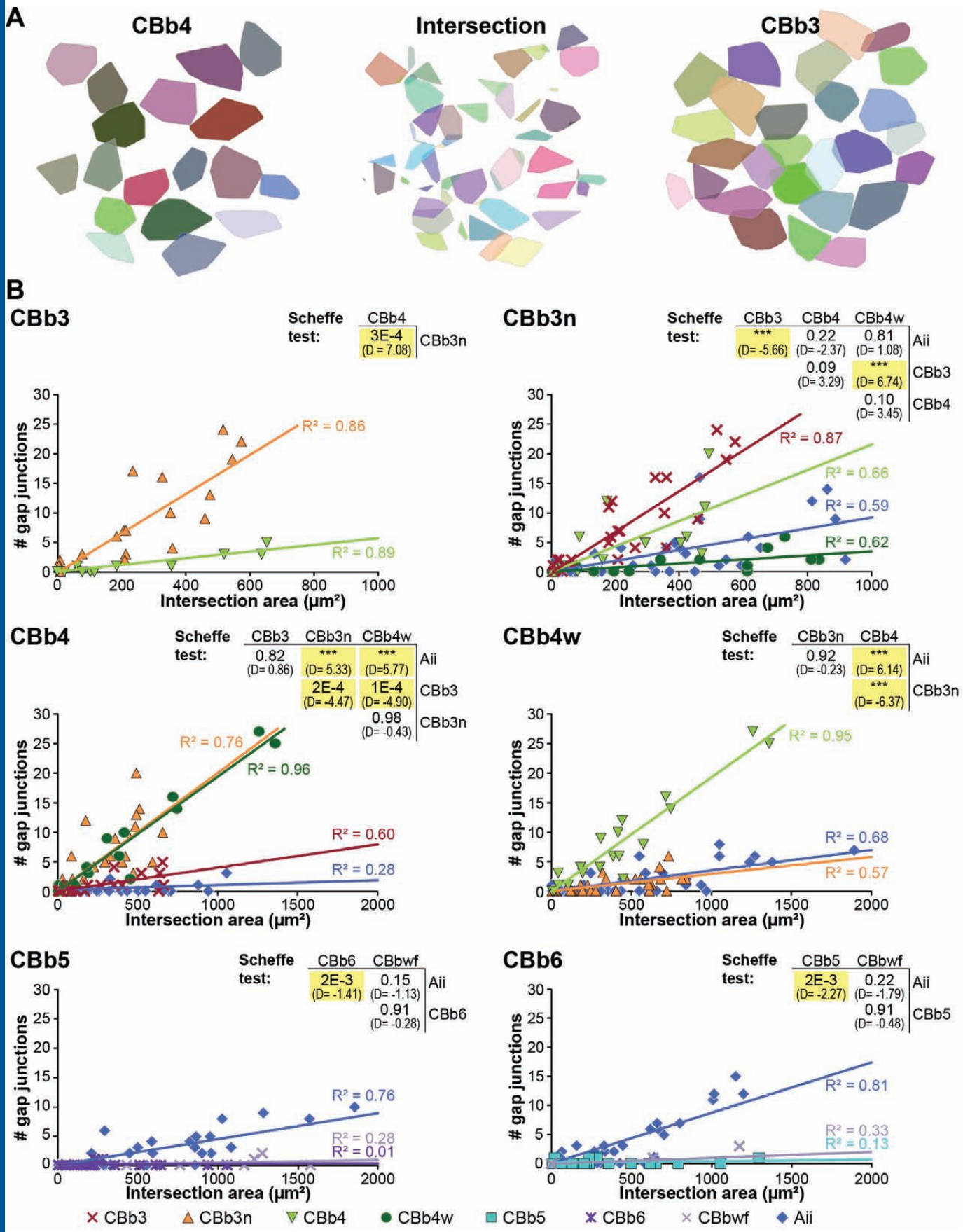

JNeurosci Accepted Manuscript

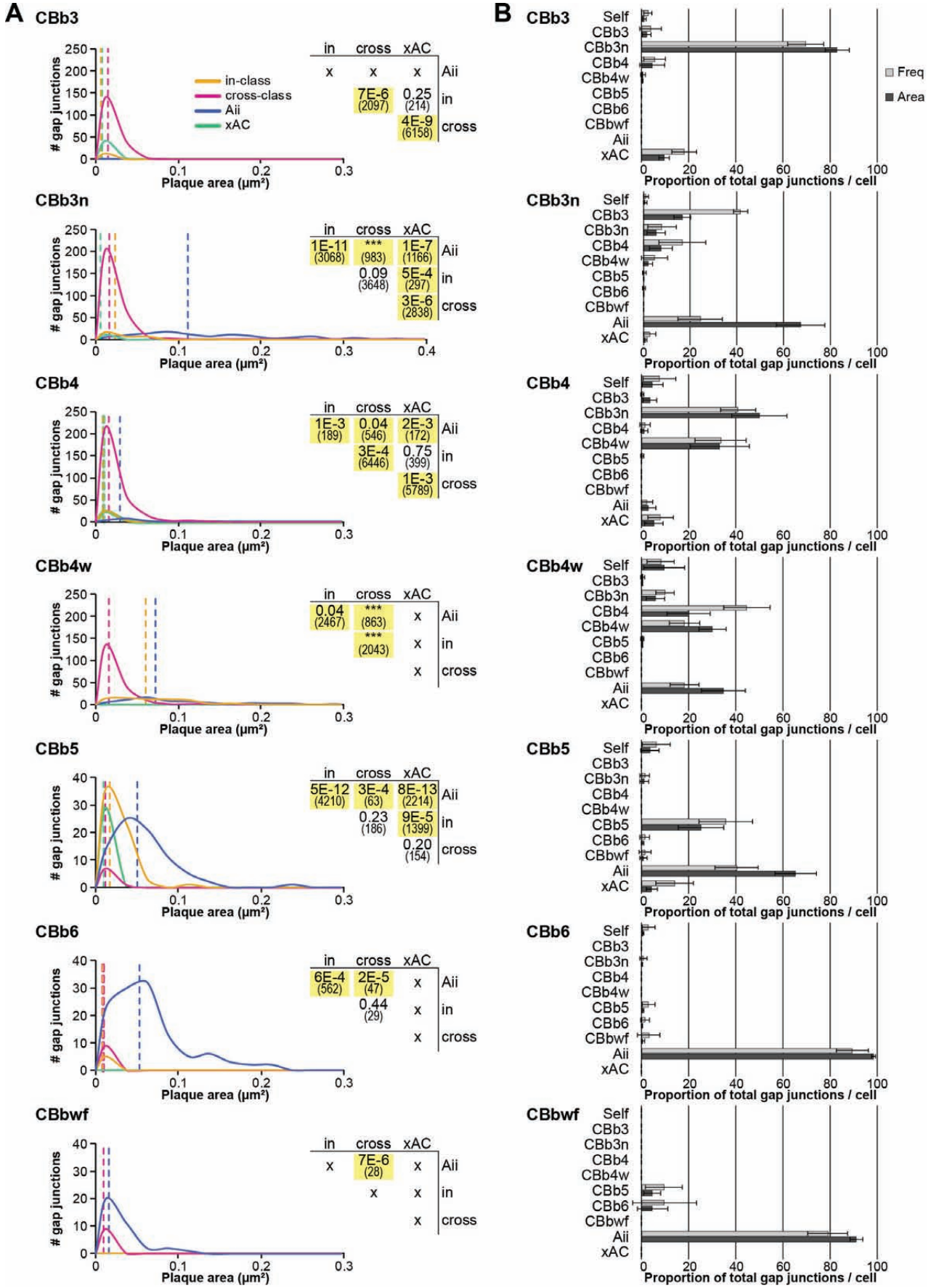

JNeurosci Accepted Manuscript

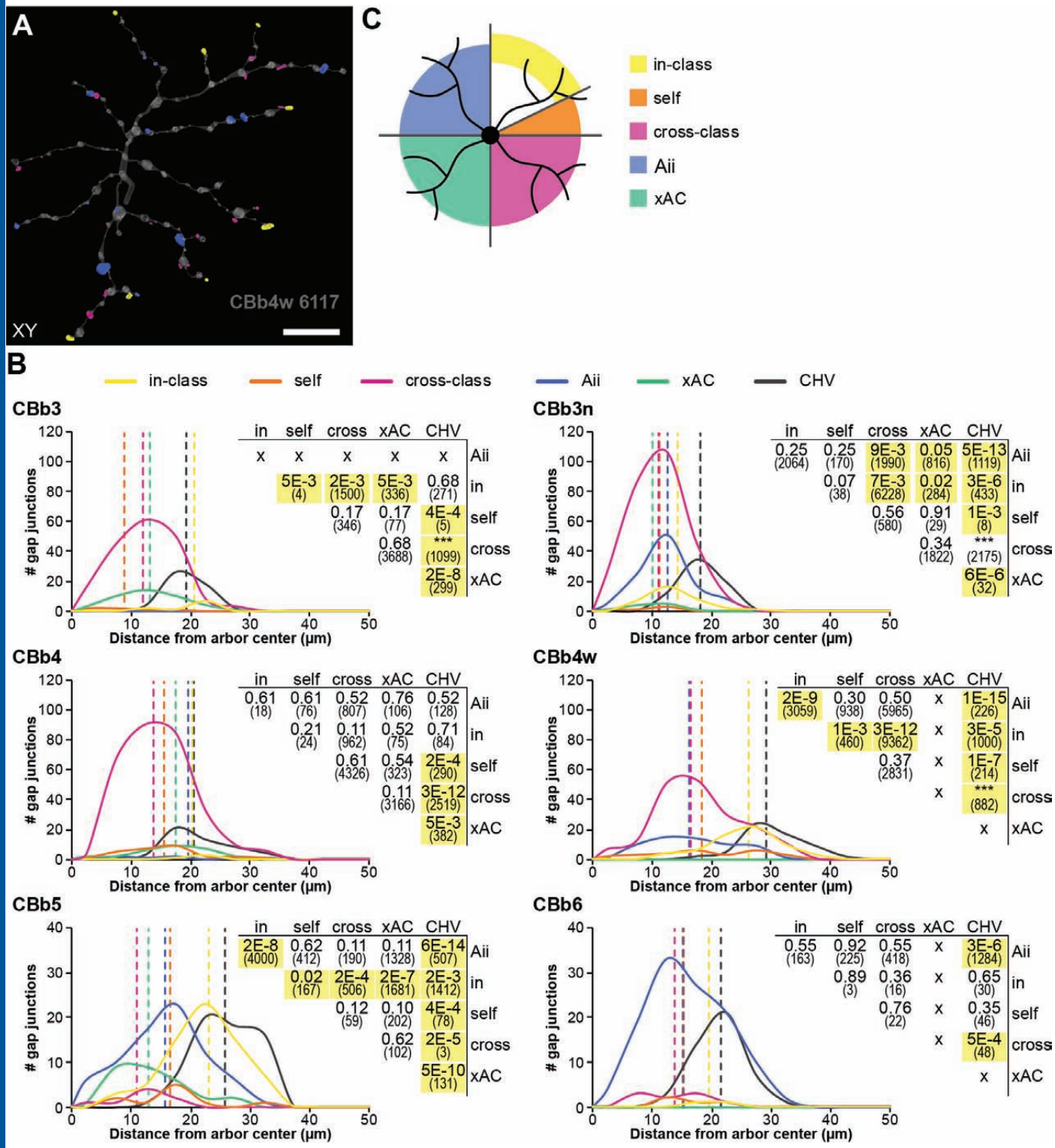

JNeurosci Accepted Manuscript

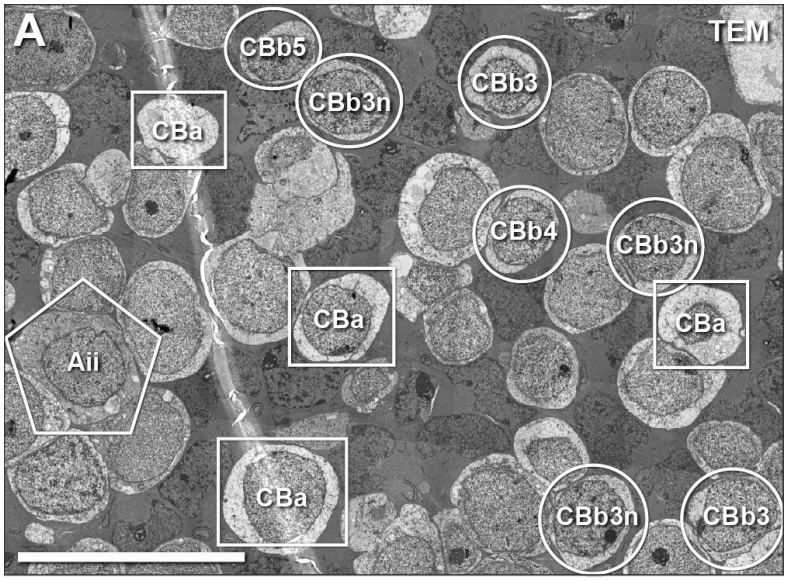

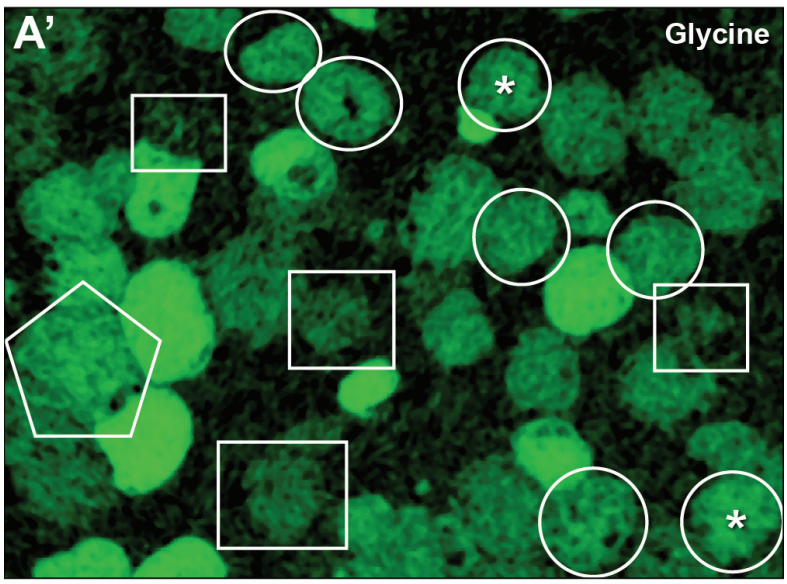

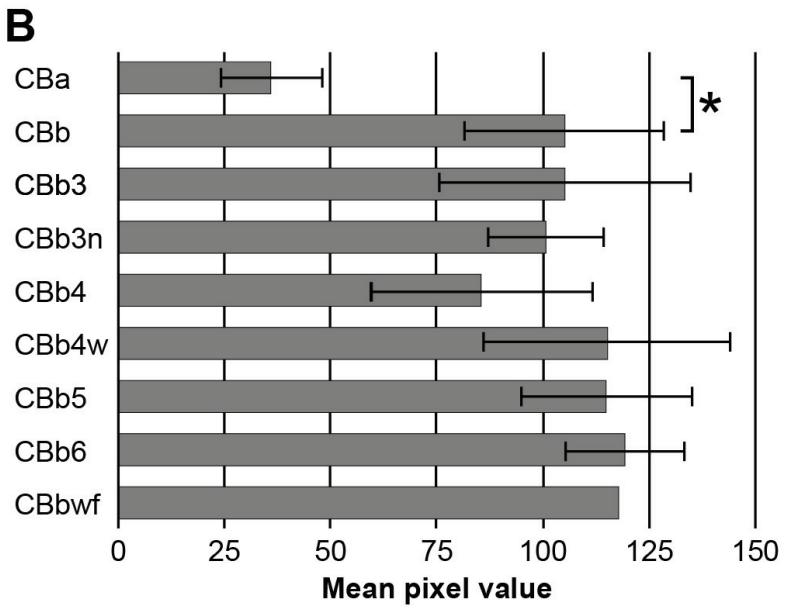

JNeurosci Accepted Manuscript

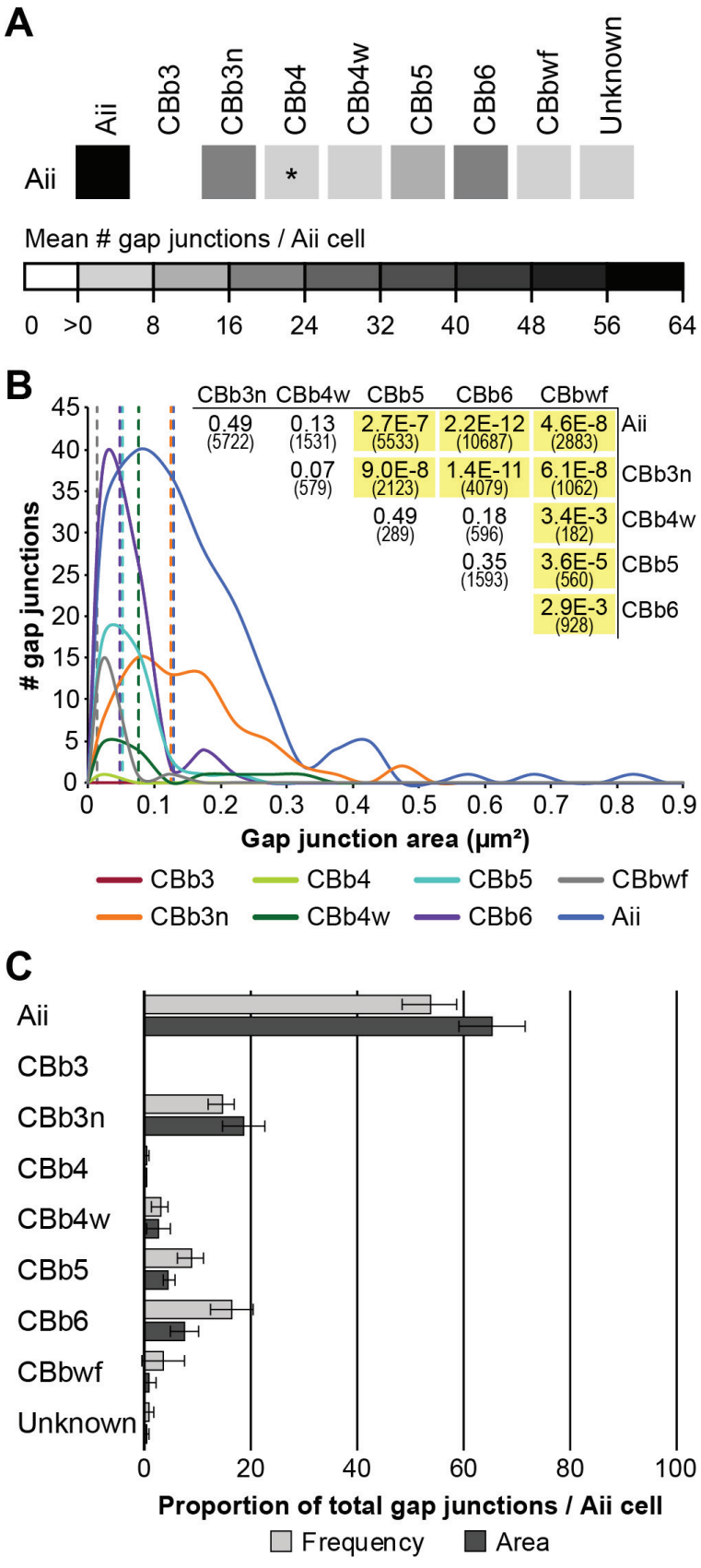
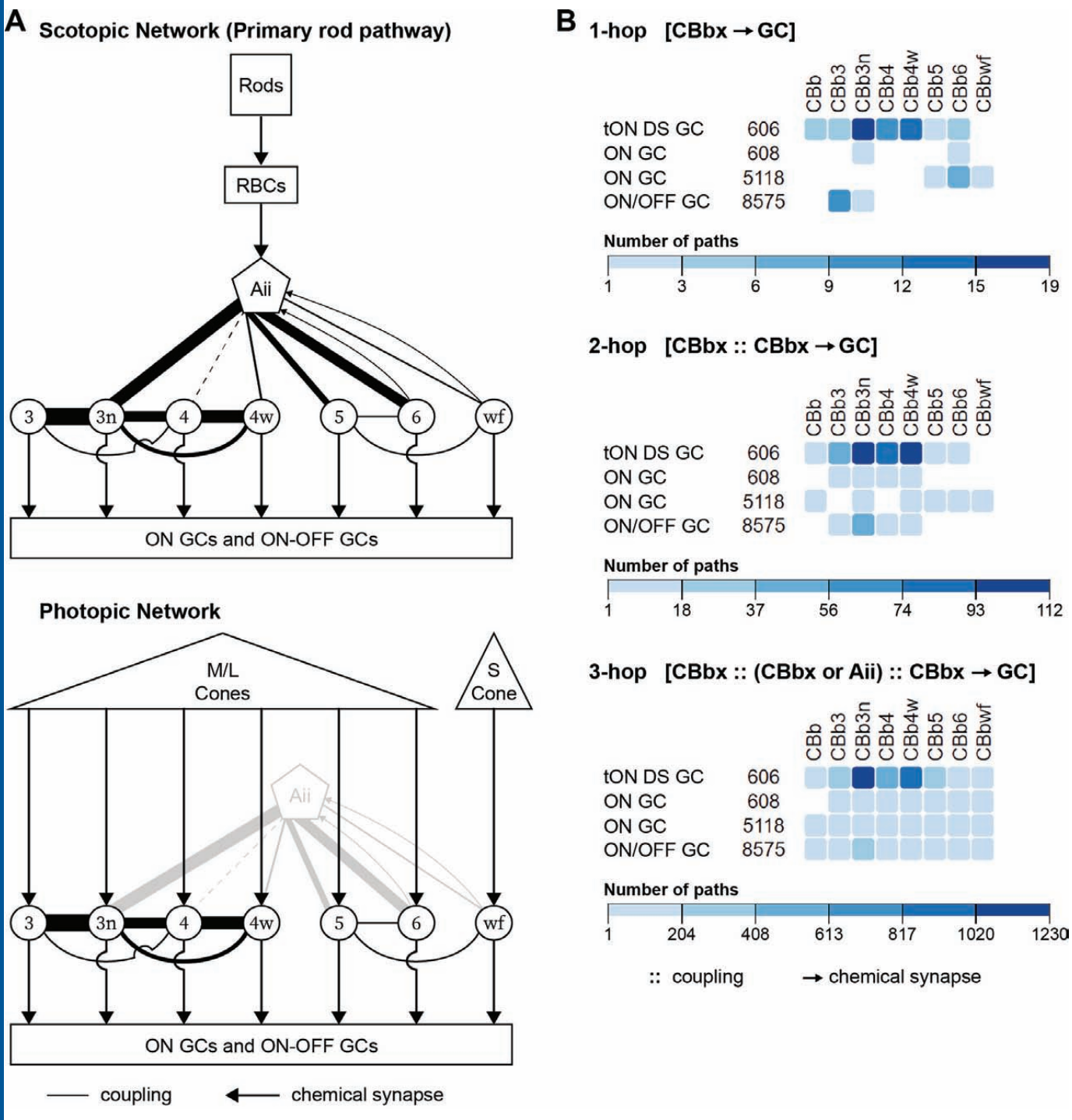
JNeurosci Accepted Manuscript